MEASUREMENT MODEL OF IONOSPHERIC ELECTRON CONTENT WITH CYGNSS

BY

JORDI XING ZHANG

DEPARTMENT OF MECHANICAL, MATERIALS AND
AEROSPACE ENGINEERING

Submitted in partial fulfillment of the
requirements for the degree of
Master of Science in Mechanical and Aerospace Engineering
in the Graduate College of the
Illinois Institute of Technology

Approved 
Adviser

Chicago, Illinois
December 2013

ACKNOWLEDGEMENT

I would like to express my very great appreciation to all the people who have supported me in this work. My advisor Seebany Datta-Barua I thank for allowing me the opportunity to investigate an area of interest in space and the honor of being her first Master student. Her support, guidance and enthusiasm throughout this year have been invaluable and greatly appreciated. Special thanks to Dr. Boris Pervan for providing me insights and reviewing this dissertation. I thank both Seebany and Boris for all their attention while I have been studying overseas in the US, far from home.

I am also grateful to Professor Kevin Cassel, my academic advisor, and Professor Qian, who has served on my thesis defense committee. I appreciate Professor Lisowski for providing me the license for using STK. Thanks in particular to Jessica Nicholson for her help in financial and academic administration. I would also like to express my gratitude for the collaboration of Dr. Aaron Ridley and Dr. James Garrison on this dissertation.

Thanks to Professors David Segarra and Conxita Flaqué from my home university for encouraging me to study abroad in the US. I also appreciate the help of my lab members, Daniel Miladinovich and Yang Su, in improving the quality of my work.

And to my family and close friends: I am especially grateful to my parents, Qilai Xing and Yan Zhang, for all the personal sacrifices they have made to make

so many opportunities available to me; and to Qiaoni and Sergio for all these years of encouragement and support.

TABLE OF CONTENTS

LIST OF TABLES

LIST OF FIGURES

LIST OF ABBREVIATIONS

Abbreviation	Definition
C/A	coarse / acquisition
CHAMP	Challenging Minisatellite Payload
COSMIC	Constellation Observing System for Meteorology, Ionosphere and Climate
CYGNSS	Cyclone Global Navigation Satellite System
DDM	Delay Doppler Map
DDMI	Delay Doppler Mapping Instrument
DMC	Disaster Monitoring Constellation
ECEF	Earth-Centered, Earth-Fixed
ENU	East, North, Up
GNSS	Global Navigation Satellite System
GNSS-R	Global Navigation Satellite System Reflectometry
GPS	Global Positioning System
GPST	Global Positioning System Time
IP	Ionospheric Point
IRI	International Reference Ionosphere
LEO	Low-Earth Orbit
MEO	Medium Earth Orbit
MET	Meteorology

MSL	mean sea level
NASA	National Aeronautics and Space Administration
OCXO	oven-controlled crystal oscillator
OF	obliquity factor
PRN	pseudo-random noise
P(Y)	precision (encrypted)
RAAN	Right Ascension of the Ascending Node
RF	radio frequency
RO	Radio Occultation
SAC-C	Scientific Application Satellite-C
SP	Specular Point
STK	Satellite Tool Kit
SWH	significant wave height
TCXO	temperature-compensated crystal oscillator
TEC	Total Electron Content
TECU	Total Electron Content units
UCAR	University Corporation for Atmospheric Research
UTC	Coordinated Universal Time
VTEC	Vertical Total Electron Content
WGS	World Geodetic System
XO	quartz crystal oscillator

LIST OF SYMBOLS

Symbol	Definition
a	Semi-major Axis
b	Semi-minor Axis
c	Speed of Light
c_n	Tropospheric Empirical Coefficient
ΔI	Horizontal Ionospheric Delay Variation
Δr	Extra Geometric Range
$\Delta\tau_{rel}$	Relative Apparent Transit Time
$\Delta\varepsilon$	Relative Signal Noise
Δ^{Iono}	Ionospheric Path Delay
Δ^{Trop}	Tropospheric Path Delay
δt^s	Satellite Clock Bias
δt_u	Receiver Clock Bias
E	Elevation Angle
e	Partial Pressure of Water Vapor
f	Radio-Frequency
h	Height
I_{below}	Ionospheric Delay Below the CYGNSS Height
λ	Geographic Longitude
m	Mapping Function

N	Carrier Phase Cycle Ambiguity
N_e	Electron Density
N^{Trop}	Tropospheric Refractivity
$\boldsymbol{n}$	Normal Vector
n_{gr}	Group Refractive Index
n_{ph}	Phase Refractive Index
ϕ	Geographic Latitude
R_e	Mean Earth Radius
r	True Range
s_0	Geometric Range
T_R	Tropospheric Delay of the Reflected Signal
θ_i	Angle of Incidence
θ_r	Angle of Reflection
τ	Actual Transit Time
$\boldsymbol{u}$	Unit Vector
$x^{(k)}$	PRN Sequence for Satellite k
$x^{(l)}$	PRN Sequence for Satellite l
z	Zenith Angle

ABSTRACT

Global ionospheric imaging is currently limited by a lack of significant quantities of observations over the oceans. This deficiency of measurements arises because coverage from Global Navigation Satellite System (GNSS) remote sensing tools is typically limited to regions over land by using ground-based receivers. This dissertation presents the opportunity to estimate ionospheric data over the oceans by using reflected GNSS signals received by the upcoming Low-Earth Orbit (LEO) satellite constellation Cyclone Global Navigation Satellite System (CYGNSS).

CYGNSS is currently being developed by NASA primarily for hurricane predictions. Its eight micro-satellites will have a single-frequency Global Positioning System (GPS) receiver onboard and zenith and nadir antennas that collect GPS signals reflecting from the ocean surface of Earth. This study investigates the possibility of leveraging CYGNSS for a secondary science mission, using GNSS-Reflectometry for ionospheric remote sensing.

A mathematical model is developed that retrieves ionospheric electron content by using ranging measurements from direct and ocean-reflected GPS signals onboard CYGNSS satellites. The measurement model terms can be grouped as geometric raypath and signal refraction components due to the troposphere and the ionosphere. Each term of the model is analyzed and quantified by applying fundamental physical principles and empirical models. The

implementation of a multi-orbit simulation estimates the magnitudes of anticipated electron content measurements with CYGNSS.

CHAPTER 1

INTRODUCTION

Society increasingly depends on communication and navigation satellites, which are vulnerable to operational errors by space weather effects. The ionosphere, an ionized layer of the upper atmosphere, comprises only five percent of the Global Positioning System (GPS) signal path to a ground-based receiver, but refracts the signal such that it is the largest error source for single frequency civilian users [24]. Understanding and predicting the complex dynamic environment of the upper atmosphere therefore grows more urgent. Paradoxically, the distortion of GPS signals due to the ionosphere ends up being a great benefit for the scientific community by taking advantage of its remote sensing properties.

While GPS has emerged as a widespread tool for ionospheric remote sensing, coverage is typically limited to regions over land by using ground-based receivers [20]. In order to address this problem, it is interesting to consider the upcoming Cyclone Global Navigation Satellite System (CYGNSS) Mission, which is currently in the design stage and being developed by NASA. The constellation consists of eight Low-Earth Orbit (LEO) micro-satellites designed primarily for extreme tropospheric weather predictions. The CYGNSS satellites have a single-frequency GPS receiver onboard as well as one zenith antenna that receives direct GPS signals, and two nadir antennas that collect reflected GPS signals

bouncing off the ocean surface of Earth [5]. This dissertation is concerned with using CYGNSS satellites to remotely sense the ionosphere over the oceans by using its GPS ranging measurements.

Other GNSS remote-sensing missions equipped with GPS receivers onboard have been used for ionospheric studies such as COSMIC, MET and CHAMP [21]. Radio Occultation (RO) is the most commonly used remote sensing technique that involves a LEO satellite receiving a GNSS signal. This technique relies on the refraction experienced by the electromagnetic signal when it passes through the planet's atmosphere as the satellite is occulted by the Earth [19]. The ionospheric electron content can be retrieved from the refraction induced by the upper atmosphere. In the neutral atmosphere, other physical properties such as temperature, pressure and water vapour content can also be derived, allowing radio occultation applications in meteorology [15].

CYGNSS differs from other LEO missions because it involves GNSS-Reflectometry, which consists of making measurements from the reflections of navigation signals scattered from the ocean surface of the Earth. Each of the micro-satellites will be equipped with a Delay Doppler Mapping Instrument (DDMI) capable of generating two-dimensional correlation functions called as Delay Doppler Maps (DDM). The DDM is a representation of the reflected signal power distribution relative to the direct as a function of the time chip delay and the Doppler frequency. Therefore, the correlation function needs to be performed between the direct and the reflected signals. Each DDMI can process four

different sets of direct-reflected signals coming from four different GPS satellites simultaneously [5].

This dissertation shows the achievement of retrieving ionospheric electron content with CYGNSS satellites over the oceans. The obtained measurements can be assimilated into models and tomographically reconstruct ionospheric plasma, which will improve the existing physical understanding of the ionosphere and the accuracy of ionospheric empirical models [3]. Also, the possibility of getting measurements without having to launch new infrastructure implies an economical opportunity for high quality science.

1.1 The Ionosphere

The ionosphere is a region of the Earth's upper atmosphere where neutral particles undergo photoionization caused by the radiation from the Sun [30]. In practice, it has a lower limit of 50 km to 70 km and no distinct upper limit; however, for many application purposes 2,000 km is typically set as the upper limit. It overlaps the thermosphere and parts of the mesosphere and exosphere. During photoionization, electrons are dislodged from atoms and molecules to produce the ionospheric plasma, which is a gas of free ions and free electrons that move throughout the ionosphere. Photoionization occurs on the sunlit side of the Earth. Generally only the shorter wavelengths of solar radiation are energetic enough to generate this ionization: the extreme ultraviolet and X-ray part of the spectrum [1]. The recombination of these ions and electrons

proceeds slowly at high altitudes due to low gas densities, so that quite high concentrations of free electrons persist even during night.

Although the ionosphere only contains a small fraction of atmospheric material, it is very important because of its effects on the propagation of radio signals from spacecraft vehicles. Figure 1.1 shows altitude positions of spacecraft vehicles relative to the ionospheric region (white dots).

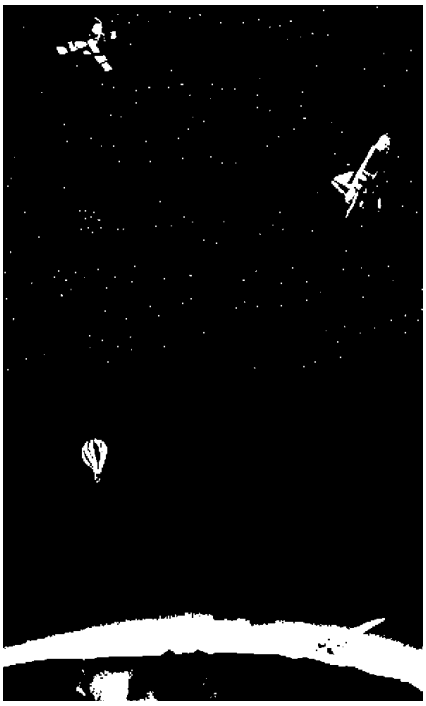

Figure 1.1. Altitude Positions of Aerospace Vehicles in the Ionosphere [1]

1.1.1 Ionospheric Characteristics. The flux of free electrons in the ionospheric plasma divides the ionosphere into four different regions, distinguished by their ability to retain free electrons. In order of increasing altitude and increasing electron concentration, these layers are called D, E, F1 and F2 [30]. The D-region is the lowest extending from 50 to 90 km. The E-

region covers altitudes between 90 and 150 km, and the F-region lies above the E-region.

It has been observed since the 1920s that the ionosphere varies dramatically with geomagnetic latitude. Particularly, there appear three distinguishable ionospheric regions: high-latitude, mid-latitude and low-latitude. The mid-latitude ionosphere is the easiest to understand and has the best agreement with the classical ionospheric models. The high-latitude ionosphere is directly coupled to the magnetospheric tail by the stretched auroral magnetic field lines. The low-latitude ionosphere is sensitive to plasma instabilities and changes to the magnetospheric ring current. Figure 1.2 shows the ionospheric layers and the main ions that compose each region. Figure 1.3 shows how typical mid-latitude vertical electron density profiles change over the sunspot cycle for daytime and nighttime.

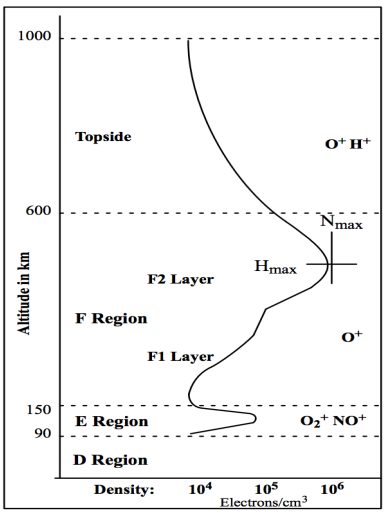

Figure 1.2. Ionospheric Layers and their Predominant Ion Populations [1]

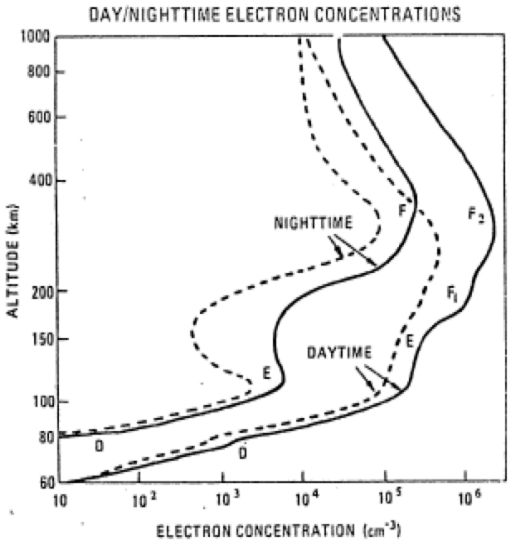

Figure 1.3. Typical Mid-Latitude Daytime and Nighttime Electron Density Profiles for Sunspot Maximum (Solid Lines) and Minimum (Dashed Lines) [1]

From a satellite-based radionavigation and communication point of view, the F2 layer is the most important one because the electron densities reach their maximum value [30]. Above the maximum electron density of the F2-region, the electron density decreases monotonically out to several Earth radii. Not only does the overall electron density decrease at night, but also the F1 and D-layers disappear soon after sunset.

1.1.2 Ionospheric Propagation Effects. The interaction of the radio signal wave with the ionospheric plasma is one of the main reasons for the limited accuracy and vulnerability in satellite based positioning and time estimation, which rely on the trilateration radionavigation principle [17].

A trans-ionospheric radio wave propagating through plasma is refracted due to the presence of electron concentrations. When a radio wave is refracted,

the propagation path suffers a curvature and its speed differs from that in free space. Refractions lead to a propagation delay (and phase advance) of satellite navigation signals, yielding a time and apparent travel distance larger than the real one [17]. The propagation delay is described by the refractive index of the ionosphere, which is not equal to unity as it is in free space. The ionospheric delay depends also on the frequency of the radio wave, since the ionosphere is a dispersive medium [17].

Because a GPS user's receiver estimates its position using distances based on signal transit time from transmitters at known locations (the GPS satellites), refraction alters the apparent distance from the known locations, thus introducing an error. The ionospheric error range varies from a few meters at GPS L1 frequency (1575 MHz) to numerous tens of meters at zenith, while the troposphere error range goes between two to three meters at zenith. With a linear combination of dual-frequency observables, the major part of the ionospheric refraction can be eliminated since the ionosphere is a dispersive medium. However, higher order nonlinear effects, which are generated by inhomogeneous plasma and anisotropy of the magnetic field, are not removed in this linear approach. Predominantly the second and third order ionospheric terms and errors due to bending of the signal remain uncorrected. The error range can be several tens of centimeters at low elevation angles and during high solar activity conditions [17].

As already mentioned, the propagation delay of a radio wave through the ionospheric plasma is characterized by the refractive index of the ionosphere. The refractive index fundamentally depends on the electron density and the frequency of the signal being transmitted. Thus, the spatial distribution of the electron density along the ray path and the signal frequency determine the ionospheric impact on the electromagnetic wave.

1.2 The Upcoming NASA CYGNSS Mission

The Cyclone Global Navigation Satellite System (CYGNSS) is a new space-borne mission concept from NASA. It is a constellation of satellites being designed primarily for extreme tropospheric weather predictions with a current tentative lunch date of 2016 [27]. The main goal is to investigate the coupling between ocean surface properties, moist atmospheric thermodynamics, radiation, and convective dynamics in the inner core of tropical cyclones. CYGNSS data will allow scientists to explore air-sea interaction processes that take place near the inner core of the storms for the first time. This mission will contribute to the advancement of forecasting and tracking methods [27].

CYGNSS will be formed by a constellation of eight small satellites carried to orbit on a single launch vehicle. The eight observatories are positioned in a low inclination plane of 35 degrees residing in Low Earth Orbit (LEO) at 500 km altitude. Each of the micro-satellites is single-frequency and has one zenith and two nadir antennas that receive both direct and reflected signals from Global

Positioning System (GPS) satellites. The direct signals pinpoint the CYGNSS satellite positions and the reflected signals respond to ocean surface roughness, from which wind speed is retrieved.

Figure 1.4 shows the CYGNSS space-borne concept. The CYGNSS satellites are shown as yellow spheres. The white lines represent direct GPS signals and the blue ones ocean surface reflected signals. The lighter blue circles on the Earth surface show individual samples over the ocean.

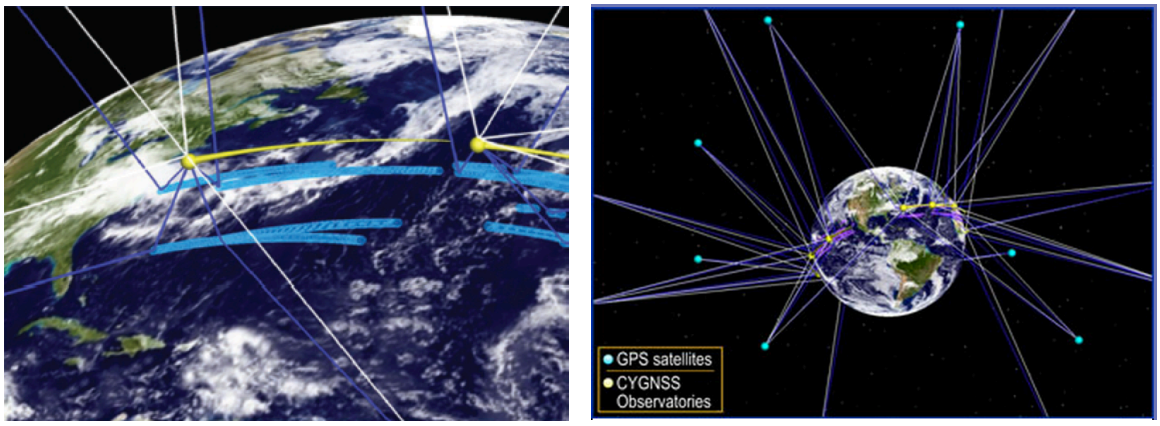

Figure 1.4. The CYGNSS Space-Borne Concept [29]

Each observatory simultaneously samples quasi-specular scattered signals from up to four GPS transmitters. The resulting spatial and temporal sampling properties can provide excellent sampling of evolving tropical cyclones.

1.2.2 CYGNSS Science. CYGNSS addresses the limitations in the improvement of the accuracy of tropical cyclone intensity forecasts. This forecast deficiency lies in inadequate observations and modeling of the storm inner core [5]. The problem is approached by combining “the all-weather performance of GPS-based

bistatic scatterometry with the sampling properties of a dense satellite constellation. By doing this, CYGNSS can take measurements of the ocean surface wind field with unprecedented temporal resolution and spatial coverage under any precipitating conditions" [5]. Figure 1.5 and 1.6 show CYGNSS sampling capabilities covering great parts of ocean represented by ground tracks for 90 minutes and 24 hours respectively. Each of the 8 observatories is capable of measuring 4 simultaneous reflections, resulting in 32 wind measurements per second across the globe.

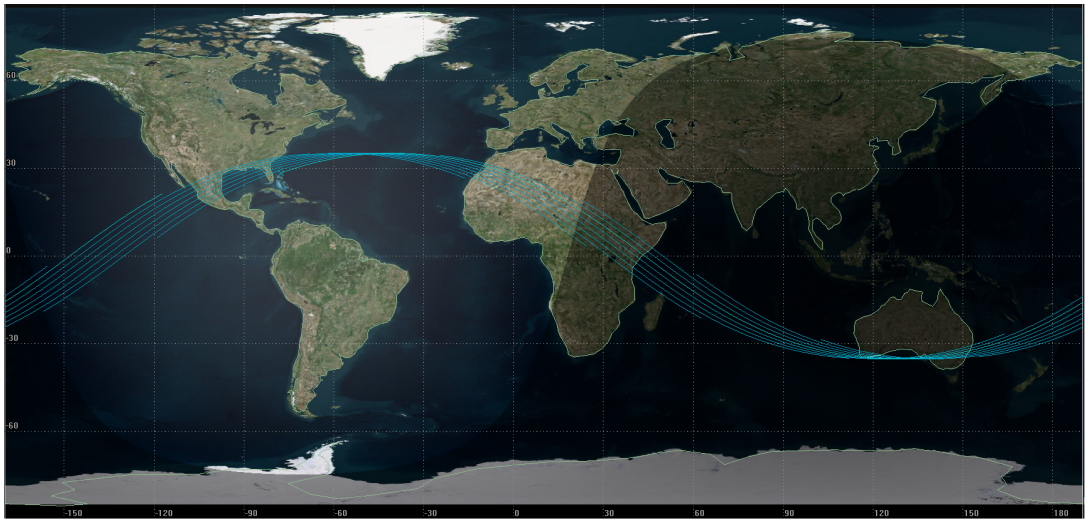

Figure 1.5. CYGNSS Ground Tracks for 90 Minutes

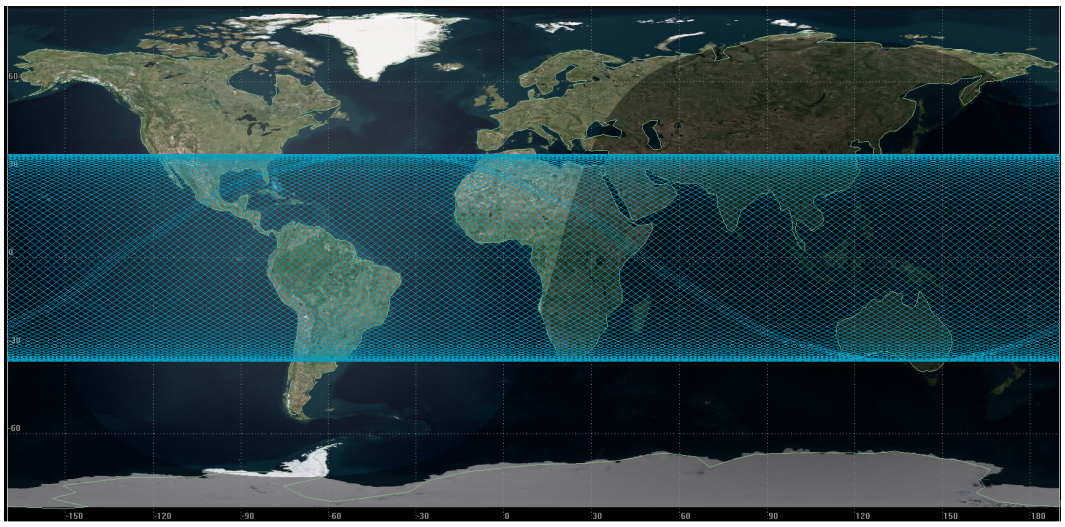

Figure 1.6. CYGNSS Ground Tracks for a Full Day

1.2.3 CYGNSS Technology. The eight micro-satellites of CYGNSS capture a detailed view of the ocean's surface thanks to a higher pass over frequency compared to one large satellite. Each micro-satellite mass and power are estimated to be 18 kg and 49 watts.

Each CYGNSS observatory will be equipped with a Delay Doppler Mapping Instrument (DDMI), which consists of a multi-channel GPS receiver, one low gain zenith antenna to provide space-location capability and two high gain nadir antennas to collect scattering GPS signals. A sketch of a CYGNSS observatory is represented in Figure 1.7 and the elements that compose the DDMI is shown in Figure 1.8.

In terms of stabilization, attitude is 3-axis stabilized using horizon sensors, a magnetometer, pitch momentum wheel, and torque rods.

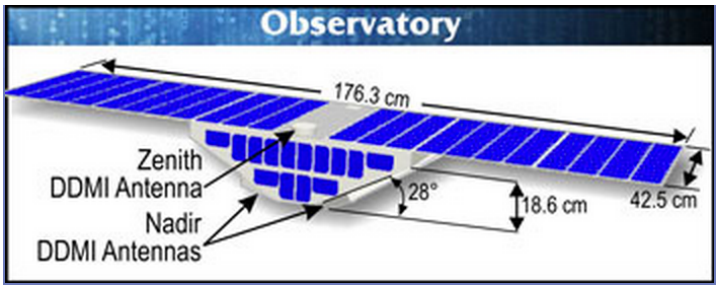

Figure 1.7. Scheme of a CYGNSS Observatory [5]

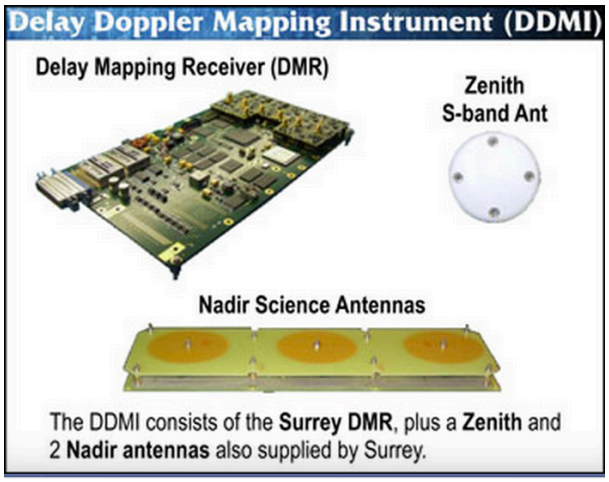

Figure 1.8 Elements of a CYGNSS DDMI [5]

1.3 Previous Work

The permanent availability of L-band radio signals transmitted by GPS satellites has opened a new dimension for probing the ionosphere. Several LEO satellite missions are equipped with GPS receivers onboard to probe the ionosphere. Radio occultation is the most used satellite-based remote sensing technique to explore the ionosphere, while GNSS–Reflectometry is the new branch of study to investigate its feasibility.

1.3.1 Radio Occultation. Radio occultation (RO) is a remote sensing technique used for measuring the physical properties of a planetary atmosphere [19]. It is based on measurements of the change of ray path bending, phase or signal strength of the radio wave while approaching the planetary surface until it is completely occulted by Earth. This technique provides a simple and inexpensive tool for retrieving a profile of the entire vertical electron density structure from satellite orbit heights down to the bottom of the ionosphere.

The ionosphere has two important effects on GPS signals during occultation: a geometric bending or curvature effect and a scintillation effect, which is produced by ionospheric irregularities.

The general scheme of a radio occultation is shown in Figure 1.9, where a LEO satellite receives the occulted signal coming from the GNSS.

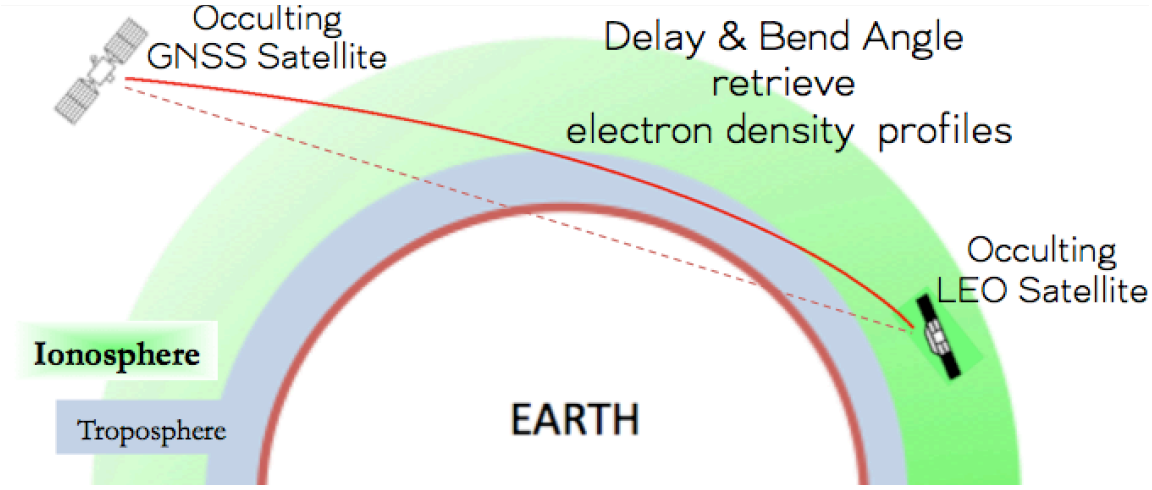

Figure 1.9. Occultation Geometry Between the GNSS and the LEO Satellites

It has been demonstrated that the GPS radio occultation technique provides a powerful and complementary vantage point over ground-based

measurements for remote sensing of the Earth's neutral atmosphere and ionosphere. Therefore, several satellite missions have been launched with GPS radio occultation receivers, such as GPS/MET, CHAMP, COSMIC and SAC-C.

GPS/MET – The Global Positioning System Meteorology experiment started working on April 1995 to test the occultation concept for the first time [15]. The University Corporation for Atmospheric Research (UCAR) managed the experiment by placing a GPS receiver in a LEO satellite, which was tracking GPS satellites setting behind Earth's limb. GPS/MET is capable of tracking up to eight GPS satellites simultaneously at both frequencies transmitted by GPS and collects between 100 and 200 globally distributed occultations daily. The experiment provided a very rich data set to study the ionosphere and lower atmosphere properties accurately: density profiles, temperature, pressure and humidity.

CHAMP – The German research satellite Challenging Minisatellite Payload for geo-scientific research provided the first opportunity to create continuous RO data for climate monitoring for a multi-year period of >5 years [10]. Since March 2002, it has been recording continuously about 230 RO profiles per day. These measurements allowed CHAMP to build monthly and seasonal mean climatologies of atmospheric microwave refractivity, pressure, geopotential height and temperature.

COSMIC – The Constellation Observing System for Meteorology, Ionosphere and Climate, also known as Formosat-3, is a constellation mission

designed to perform research in meteorology, ionosphere, climatology and space weather [28]. Currently, it consists of six small satellites orbiting at around 800 km altitude and 30 degrees of separation in longitude between each satellite. Each is equipped with four sets of GPS receivers to measure the bending angles of GPS ray paths passing through the ionosphere in order to obtain the ionospheric refractivity index, which is directly related to the electron density.

SAC-C – The Scientific Application Satellite-C is an international cooperative Earth observation mission launched on November 2000 [19]. The SAC-C mission involves studies and observations of the dynamics of Earth's surface, atmosphere, ionosphere and geomagnetic field. This mission works with radio occultation techniques to provide results of the neutral atmosphere.

1.3.2 GNSS – Reflectometry. The idea of working with Global Navigation Satellite System Reflectomery (GNSS-R) came out as a solution to cover the lack of ionospheric data over the oceans or ice sheets by performing measurements exclusively over water, since radio occultation does not always read over the ocenas [4]. This technique involves taking measurements from GNSS signals reflected on the Earth, which presents difficulties in terms of signal strength as they are weakened upon reflection. One of the main reasons that has made this technique possible is the implementation of downward-pointing high-gain left-hand circularly polarized antennas to any satellite carrying a single frequency altimeter [20]. Several experiments proving evidence of this technique have

been carried on: Katzberg and Garrison [20] showed it to be possible to determine ionospheric electron density in the satellite vicinity from the GPS ocean bounce signal under certain circumstances. These circumstances need to meet requirements such as specular reflectance and adequate polarization due to antenna operation. Thus, when the ocean reflectance can be represented as specular or quasi specular, the reflected GPS signal received at the satellite altitude is nearly as strong as the direct signal. Figure 1.10 shows the GNSS-Reflectometry concept in remotely sensing the ionosphere over the oceans.

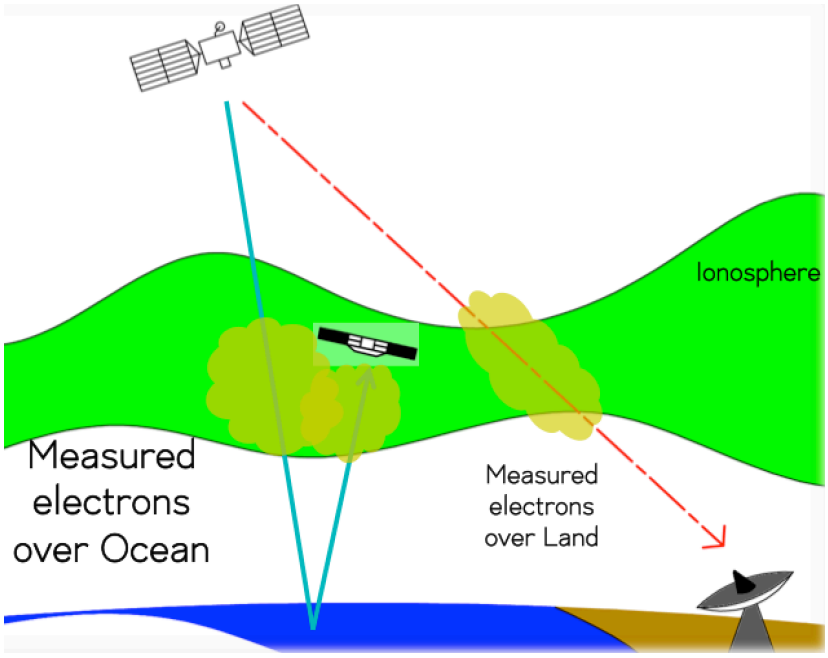

Figure 1.10. GNSS – Reflectometry Concept

Besides ionospheric measurements, GNSS signals scattered by the surface of the ocean also carry information about the sea surface state, which can be exploited to investigate its geophysical properties [4]. Consequently, GNSS-R retrieves mainly two types of sea surface information: scatterometric and

altimetric. The first one determines sea roughness and wind speed and direction, and the second one carries the significant wave height (SWH) and the mean sea level (MSL). CYGNSS will be one of the very few satellite missions, like the UK-DMC satellite mission, to perform remote sensing by using GNSS-R techniques.

UK-DMC – The Surrey Satellite Technology Ltd UK-DMC is part of the Disaster Monitoring Constellation (DMC) launched on September 2003 and retired on November 2011 [4]. The mission consisted of a low-orbit sun-synchronous satellite that carries remote sensing imaging sensors and also experimental payloads. One of the experiments demonstrated GNSS-Reflectometry possibilities. The satellite received scattered off the ocean GPS signals at an altitude of about 680 km and retrieved a 2D representation of the reflected GPS signal power as function of the time delay and the Doppler frequency, the so-called Delay-Doppler Map (DDM). The DDM will be essential to get ionospheric estimations.

1.4 Contributions

This dissertation involves four main contributions to scientific knowledge, each of which is described throughout the following chapters. However, the first two provide an introductory review of the basic elements used in this work. Chapter 1 has been concerned with describing the ionosphere and the satellite constellations to be used for ionospheric remote sensing. It also presented previous work in estimating the ionosphere involving LEO satellites receiving

GNSS signals thanks to the refractivity of the ionosphere. The basis of GPS signal processing and acquisition, and the *Delay Doppler Map* correlation function are discussed in Chapter 2, which represent the fundamental principles for the derivation of the ionospheric measurement model. The consequent chapters build the four main contributions, which are outlined in the following sections.

1.4.1 Development of a Mathematical Model for Ionospheric Remote Sensing using CYGNSS Satellite Measurements.

CYGNSS mission presents the opportunity to estimate ionospheric plasma over the oceans. Chapter 3 formulates the mathematical model that allows the retrieval of relative total electron content by using ranging measurements from direct and ocean-reflected GPS signals onboard CYGNSS satellites.

1.4.2 Analysis and Evaluation of Satellite and Raypath Geometries based on Fundamental Physical Principles.

Solving for the geometric raypath term from the measurement model requires a geometry study of the satellite configuration, which is addressed in Chapter 4. The most relevant part is the computation of the *Specular Point* location, which is the point on the ocean surface at which the reflected signal strikes. Evaluations of the results are performed to ensure the agreement with fundamental physical principles.

1.4.3 Estimation and Quantification of the Signal Refraction Error Induced by Different Regions of the Planetary Atmosphere. The GPS electromagnetic signals suffer refraction by the medium through which they travel before arriving to CYGNSS satellites. Chapter 5 describes the tropospheric delay term induced by the lower part of the atmosphere based on the *Hopfield* model. Chapter 6 deals with the ionospheric delay terms induced by the upper atmosphere subject to the *International Reference Ionosphere* and a multi-layer model.

1.4.4 Design of a Multi-Orbit Simulation for Estimating the Magnitude of CYGNSS Satellite Measurements. The last contribution is the design of multi-orbit simulation to estimate the magnitude of anticipated electron content from CYGNSS measurements by creating a sample of signals for a period of time. The simulation involves all the measurement model terms discussed throughout the chapters.

CHAPTER 2

GPS SIGNAL PROCESSING AND DDM

2.1 Global Positioning System Overview

GPS represents an important technological success in the history of mankind. At first, it was developed primarily for the U.S. military to provide precise computations of position, velocity and time [24]. During the 1990s civil applications of GPS grew at a rapid rate in many fields including transportation, civil aviation, maritime commerce, surveying and mapping, construction, mining and telecommunications. GPS originally consisted of 24 satellites and was declared fully operational in 1995.

The system works with a radio navigation principle called trilateration, in which the user's position can be retrieved if the distances to three transmitters at known locations are given. Each of the three distances is determined by measuring the transit time of a signal from a transmitting satellite to the user since these waves travel at a known speed. The basic idea of trilateration is illustrated in Figure 2.1. However, the clocks at the transmitters and the receiver are not synchronized to measure the signal transit time precisely. A synchronization error of 1 μs can result in an error of 300 m in distance measurement. Adding a fourth visible satellite, which determines the deviation of the receiver clock from GPS time, can solve this problem. This provides a four-

dimensional problem approach: three components for position and one component for time.

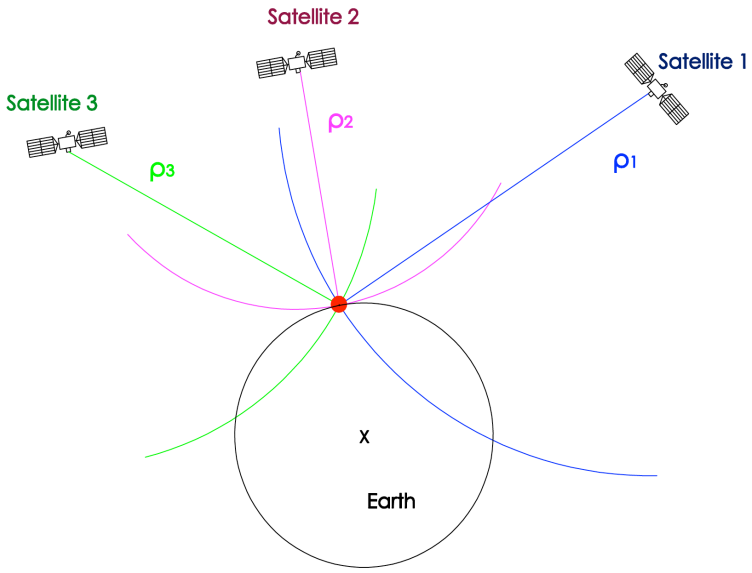

Figure 2.1. Trilateration Concept

GPS satellites broadcast signals and a user determines his position via the principle of trilateration. The constellation can handle an unlimited number of users since it does not require user interaction.

2.1.1 GPS System Architecture. The GPS system consists of three different segments known as the Space, the Control and the User Segments. The Space Segment consists of the 24 active satellites. They occupy six nearly circular orbital planes with a radius of 26,560 km, a period of approximately twelve hours and stationary ground tracks. These orbital planes are inclined at 55 degrees relative to the equatorial plane and have four primary satellite slots distributed unevenly in each orbit.

2.1.2 GPS Signals. Each GPS satellite was originally designed to broadcast continuously data using two radio frequencies in the L-band referred to as L1 and L2 [24]. L1 is centered at 1575.42 MHz while L2 is intended for military purposes only and it is centered at 1227.60 MHz. Ongoing GPS modernization includes the introduction of a civilian frequency at the L2 band, known as L2C, and a third frequency L5 at 1176.45 MHz. Each signal consists of three components, represented in Figure 2.2:

- A carrier phase which consists in a *radio frequency* (RF) sinusoidal signal with frequency L1 or L2.
- A code phase, which has a unique sequence of zeroes and ones called *pseudo-random noise* (PRN) *sequences or codes*, assigned to each satellite. It allows the receiver to determine the signal transit time instantaneously. Each satellite emits two different codes: a coarse/acquisition (C/A) code, which has a unique sequence of 1023 bits or chips, and a precision (encrypted) P(Y) code, which are restricted to authorized users only.
- A navigation data that implies a binary-coded message which contains information about satellite health status, ephemeris, clock bias parameters, and an almanac giving reduced-precision ephemeris data on all satellites in the constellation.

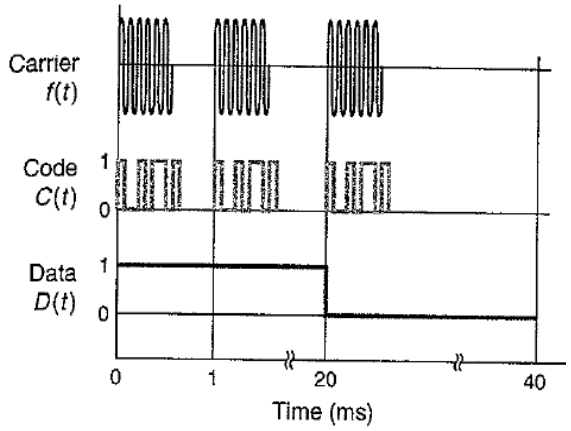

Figure 2.2. Structure of the GPS Signal Components for Civil Use [24]

The PRN sequences have two very special properties, which make RF signals attractive for use in communication and navigation.

The first property defines the *cross-correlation function*. PRN sequences are nearly *orthogonal* to each other, which means that the sum of term-by-term products of two sequences, arbitrarily shifted relative to each other, is nearly zero. Given satellites k and l, which are assigned unique PRN sequences called C/A-codes $x^{(k)}$ and $x^{(l)}$,

$$\sum_{i=0}^{1022} x^{(k)}(i) \cdot x^{(l)}(i+n) \approx 0 \quad , \quad for\ all\ n, k \neq l \tag{2.1}$$

The PRN sequences are nearly uncorrelated for all shifts. This orthogonal property allows all satellite to transmit simultaneously at the same frequency without interfering with each other.

The second property defines the *auto-correlation function*. A PRN sequence is nearly uncorrelated with itself, except for zero shift. For a C/A-code,

$$\sum_{i=0}^{1022} x^{(k)}(i) \cdot x^{(k)}(i+n) \approx 0 \quad , \quad for\ all\ |n| \geq 1 \tag{2.2}$$

The auto-correlation function of a PRN is insignificant except for zero shift where it has a sharp peak. This property allows the receiver to measure the apparent transit time of an incoming signal in order to obtain the user position. As it is shown in Figure 2.3, auto-correlation multiplies x(t) by a time-shifted replica of itself and integrates the product. Only when both sequences resemble, the auto-correlation function retrieves a large value.

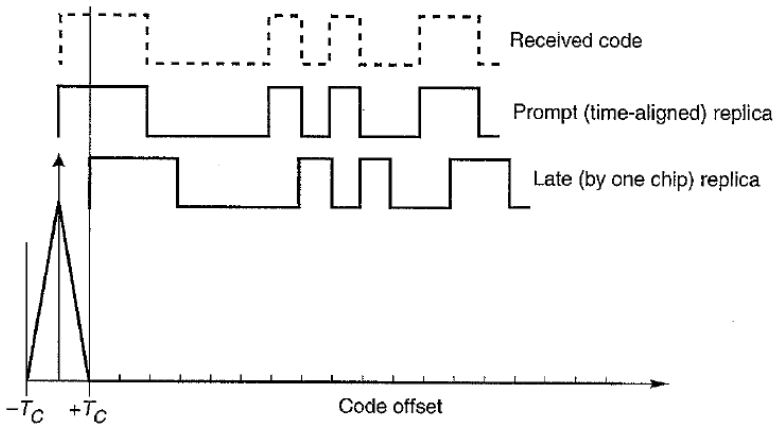

Figure 2.3. Autocorrelation Function of the Received Code with Time-Shifted Replicas [24]

2.2 GPS Signal Processing

The GPS signals are collected on the receiver and go through a process called signal acquisition and tracking. The receiver captures the RF signals emitted by the satellites, acquires the signals from satellites in view, measures signal transit time and Doppler shift, decodes the navigation message, and estimates the user position, velocity and time [24].

For a typical receiver, the signals arrive at an omni-directional antenna. From a recent almanac and an estimated idea of the user location carried by the signal, the receiver determines which satellites are in view. Then, the receiver knows the structure of each satellite C/A-code being transmitted by it, and starts attempting to 'tune' to the same code structure to acquire the signal, and from then on tracks changes in it continuously.

2.2.1 Signal Acquisition and Tracking.

In this signal-processing step, the receiver generates a replica of the known C/A-code and intends to align it with the incoming code by sliding the replica in time and performing correlation [24]. This procedure has a limited matching uncertainty to only 1023 chips. The correlation function shows the sharpest peak when the code replica is aligned with the code received from the satellite. As result, the apparent transit time τ is obtained by determining the time shift required to align the receiver-generated code replica and the signal received from the satellite. The apparent transit time multiplied by the speed of light gives the *pseudorange,* which helps to compute

the user position when there are values from four or more different satellites. Figure 2.4 shows an illustration of the estimation of the transit time.

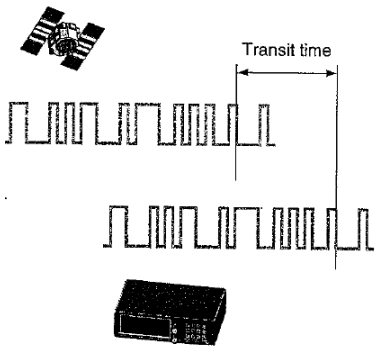

Figure 2.4. Transit Time Estimation from the Satellite to a User [24]

The code tracking of the signal lies in a feedback control loop, called as *delay lock loop*, which adjusts the replica code continuously to keep it aligned with the code in the incoming signal. After that, the PRN code is removed from the signal. Next, the signal is directed to another feedback control loop called *phase lock loop*, in which the receiver generates a sinusoidal signal to match the frequency and phase of the incoming signal. Consequently, the Doppler shift f is obtained in the phase lock loop. This shift in frequency is caused by the relative motion of a satellite and the user and represents the projection of the relative velocity on the line of sight. In other words, it is the pseudorange rate. Thus, the user can compute his velocity by having the pseudorange rates corresponding to four or more satellites and the satellite velocity vectors, which are derived from the navigation message.

2.3 GPS Error Sources

The measurements retrieved by the receiver are subject to a variety of errors. These errors come from several sources, which can be grouped as follows:

- Errors in the parameter values contained in the navigation message coming from a broadcasting satellite.
- Errors associated with the propagation medium through several layers of the atmosphere affect the travel time of the signal from a satellite to a receiver.
- Receiver noise and interference from signals reflected from surface in the vicinity of the antenna affect the precision of the measurement.

For the purposes of this work, the signal propagation errors are the most relevant ones, particularly since the main goal of the project is to retrieve ionospheric delay.

2.3.1 Signal Refraction, Ionospheric and Tropospheric Delays.

GPS signals are affected by the medium through which they travel from the satellites to the receiver. Most of the 26,000 km travel range, except for the final 5% of the signal travel, can be regarded as free space or in a vacuum [24], through which the electromagnetic signals travel at a constant speed c = 299,792,458 m/s . At a height of about 1,000 km, however, the signals travel

through an atmospheric layer of charged particles, known the ionosphere. At a height of about 40 km, the signals enter an electrically neutral atmospheric layer called the troposphere.

When the signals travel through the atmosphere, they suffer a phenomenon called *refraction*, which changes the signal propagation velocity. Consequently, refraction also affects the signal transit time, which is the basic measurement from GPS.

Signals are refracted when they travel through the ionosphere and the troposphere. Therefore, there are two signal delays associated with these two parts of the atmosphere: the *ionospheric* and *tropospheric delays*.

The ionospheric delay affects the speed of propagation of a radio signal according to the number of free electrons in its path, defined as the *total electron content* (TEC): the number of electrons in a column of one m^2 cross-section extending from the receiver to the satellite.

The GPS signals are also refracted by the lower part of the atmosphere composed by dry gases and water vapor. The overall effect of the neutral atmosphere is referred as the tropospheric delay. The delay experienced by a signal depends on the refractive index of the air mass along its path. This refractive index is related to the air mass density, which can be expressed as the sum of the densities of the dry air constituents and water vapor.

2.4 GPS Measurement Models

GPS satellites provide two types of measurements: code phase and carrier phase measurements. In this section, GPS measurements are examined and simple mathematical models are shown.

2.4.1 Code Phase Measurements. Code phase measurements work with the apparent transit time of the signal from a satellite to a receiver. The transit time is called "apparent" due to the fact that the receiver and the satellite clocks are not synchronized; the transit time is biased. For this reason, the range obtained by the apparent time is called pseudorange [24]. The measured pseudorange ρ can be written as follows:

$$\rho = r + c\,[\delta t_u - \delta t^s] + I_\rho + T_\rho + \varepsilon_\rho \tag{2.3}$$

Where,

r is the true range between user and satellite

c is the vacuum speed of light (299,792,458 m/s)

δt_u is the receiver clock bias

δt^s is the satellite clock bias

I_ρ is the ionospheric delay associated with the signal transmission

T_ρ is the tropospheric delay associated with the signal transmission

ε_ρ is the code phase measurement error or signal noise

2.4.2 Carrier Phase Measurements. Carrier phase measurements are much more precise than the code phase ones. The measurement, however, contains a term which is an integer unknown number of whole cycles of the carrier phase wave between satellite and user, the cycle ambiguity *N* [24]. The carrier phase measurement in units of cycles can be written as follows:

$$\lambda\phi = r + I_\phi + T_\phi + c\,[\delta t_u - \delta t^s] + N + \varepsilon_\phi \tag{2.4}$$

λ is the carrier wavelength and is used to convert the measurement cycles to range. The carrier phase measurements are extremely precise because ε_ϕ is much smaller than ε_ρ. However, the phase measurements are encumbered with integer ambiguities.

2.5 Delay Doppler Maps

In GNSS-R, a Delay Doppler Map (DDM) is generated onboard the receiver and consists of a 2-D representation of the power distribution of the reflected signal relative to the direct signal as function of delay offsets and Doppler shifts [23]. The shape of the DDM not only provides the apparent transit time and the Doppler shift, but also parameters of the sea surface state such as its roughness, wind speed or salinity. In addition, it shows the measurement of the size of the area over which the GPS signals are scattered, also known as *glistening zone*.

As it is said, a DDM also looks like a two-dimensional correlation function for the GPS C/A-codes. During signal acquisition, the receiver runs a search across the two-dimensional space (delay offset, doppler shift) as shown in Figure 2.5, where a main lobe remains distinct from all side-lobes even when Doppler offsets are present [24].

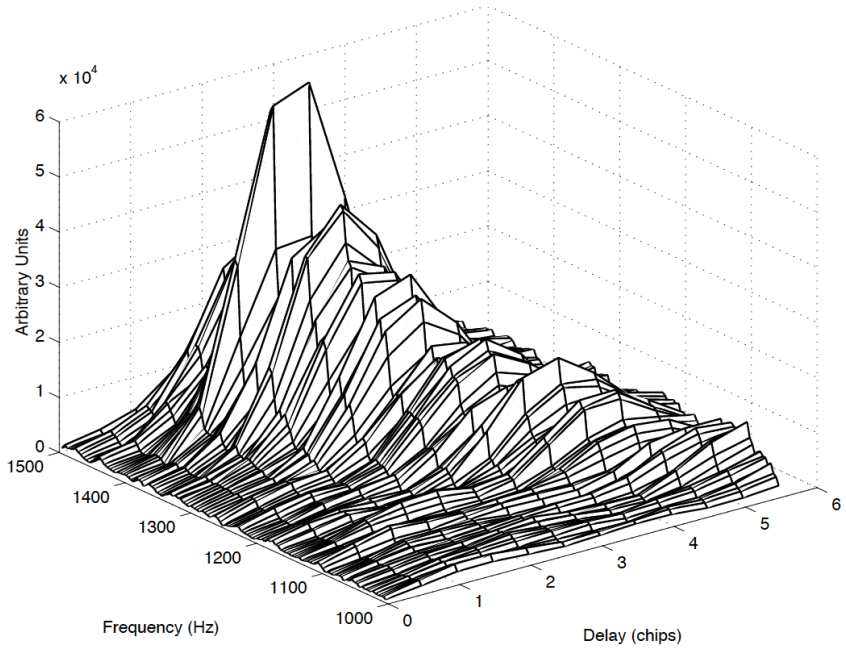

Figure 2.5. Delay Doppler Spectrum of a GPS Reflected Signal [8]

An example of a satellite that works with the DDM is the UK-DMC satellite. It uses GNSS signals scattered from the ocean to investigate the sea surface and its geophysical properties [4]. The CYGNSS mission will also be equipped to generate DDMs, from which estimation of the ocean surface roughness and wind speed is possible from two properties of the DDM illustrated in Figure 2.6. The maximum scattering cross-section in the dark red region can be related to roughness and wind speed. Additionally, the shape of the scattering arc can also

provide wind speed estimations [29]. The DDM is the output product that will be broadcast by the CYGNSS satellites.

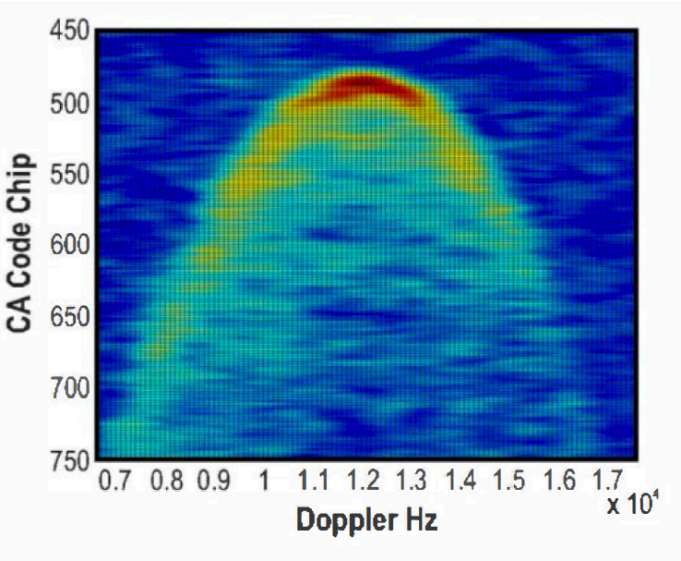

Figure 2.6. Delay Doppler Map Image Produced by UK-DMC-1 [29]

CHAPTER 3

MEASUREMENT MODEL DERIVATION

In this chapter, a mathematical model is developed to estimate the Total Electron Content (TEC) in the ionosphere by using CYGNSS satellite measurements. Particularly, the Delay Doppler Maps (DDMs) generated onboard the CYGNSS satellites are data that will be crucial to perform ionospheric investigation.

First of all, the problem statement is presented by illustrating the case scenario with the help of a schematic diagram of the transmitting and receiver satellites, the signals propagating through the medium and the scattering on the ocean surface.

Secondly, the measured pseudoranges from the GPS code phase measurements corresponding to the direct and reflected signals are shown. In order to operate with the pseudorange equations, the assumptions made are explained for each of the different terms.

Lastly, the measurement model is formulated and analyzed. The analysis identifies the outputs and inputs and explains the relevance of the DDM by showing its contribution to the measurement model.

3.1 Problem Statement

Each of the CYGNSS micro-satellites is L1 single-frequency and has one zenith antenna that collects direct signals from GPS satellites and two nadir antennas that receive reflected signals scattered from the Earth's ocean surface. The direct signals pinpoint the CYGNSS satellite positions and the reflected signals provide the ionospheric data, which will be the output of the measurement model.

The following Figure 3.1 is a picture of the stated problem. The illustration (not to scale) shows the positions of the transmitter and receiver satellites and the propagating geometries for direct and reflected signals. Note that the GPS satellite resides in Medium Earth Orbit (MEO) at an altitude of approximately 20,200 km while CYGNSS is a Low Earth Orbit (LEO) satellite mission located at about 500 km of altitude.

Thus, the CYGNSS satellite lies within the ionosphere and will generally be above the mean altitude that corresponds to the maximum total electron density, which occurs between 350-450 km [31].

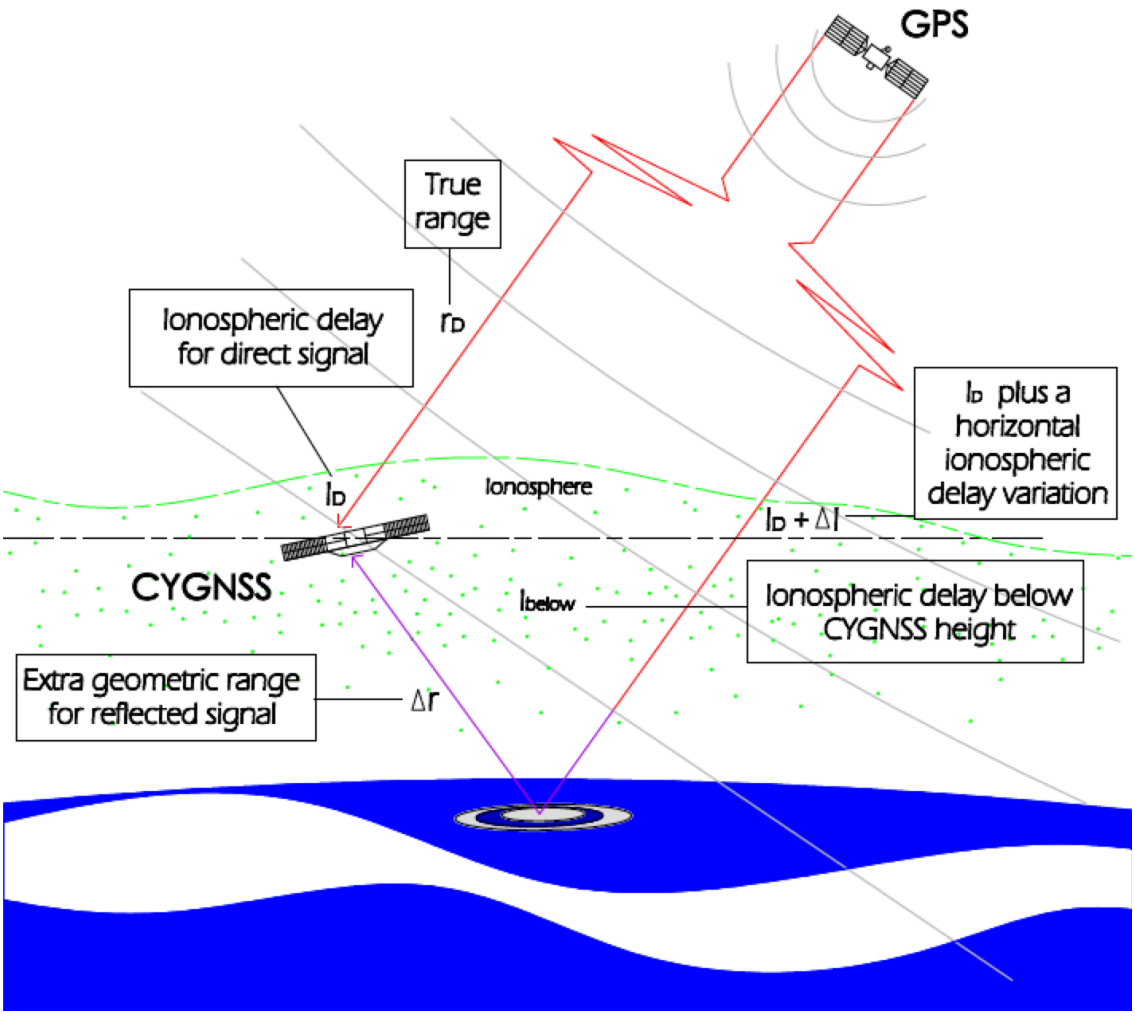

Figure 3.1. Scheme of GPS Signal Propagation and Scattering Geometries for Ocean Surface

3.2 Analysis and Assumptions

In the diagram above, the CYGNSS satellite receives two different instances of the GPS signal from a single GPS satellite. The corresponding code phase measurements of measured pseudoranges ρ for the direct and reflected GPS signals can be modeled as,

$$\rho_D = c\,\Delta\tau_D = r_D + c\,[\,\delta t_u(t_D) - \delta t^s(t_D - \tau_D)\,] + I_D + T_D + \varepsilon_D \quad (3.1)$$

$$\rho_R = c\,\Delta\tau_R = r_R + c\,[\,\delta t_u(t_R) - \delta t^s(t_R - \tau_R)\,] + I_R + T_R + \varepsilon_R \quad (3.2)$$

where,

D subscript stands for direct signal

R subscript stands for reflected signal

c is the vacuum speed of light (299,792,458 m/s)

$\Delta\tau$ is the apparent transit time

r is the true range of the signal path

$\delta t_u(t)$ is the CYGNSS receiver clock bias at arrival time *t*

$\delta t^s(t-\tau)$ is the GPS satellite transmitter clock bias at emission time $t - \tau$

τ is the actual transit time of a signal from a satellite to a receiver

I is the delay associated with the signal transmission through the ionosphere

T is the delay associated with the signal transmission through the troposphere

ε is the code phase measurement error

Consider that CYGNSS, on one hand, uses the reflected GPS signal to compute the DDM. On the other hand, the direct GPS signal is used as a

coherent reference for the coded GPS transmit signal [29]. For this reason, equation (3.1) is subtracted from equation (3.2) as follows,

$$\rho_R - \rho_D = c\,(\Delta\tau_R - \Delta\tau_D) = c\,(\Delta\tau_{rel}) = \tag{3.3}$$

$$= r_R - r_D + c\left[\delta t_u(t_R - t_D) - (\delta t^s{}_R - \delta t^s{}_D)\right] + I_R - I_D + T_R - T_D + \varepsilon_R - \varepsilon_D$$

3.2.1 Assumptions. In order to operate with this mathematical expression, the considered assumptions on the different terms of the equation are described.

Clock Bias Terms – These are error sources related to the deviation of the individual atomic clock onboard the satellites from GPS system time. Most of GPS receivers use quartz crystal oscillators (XO), which have frequency stability from 10^{-7} to 10^{-10} approximately [24]. Since the crystal's resonance frequency varies with temperature, there also exist temperature-compensated crystal oscillators (TCXO) and oven-controlled crystal oscillators (OCXO).

- The GPS satellite transmitter clock bias for the direct and reflected signals have exactly the same value since both signals are transmitted at the same time from the same GPS satellite:

$$\delta t^s{}_R = \delta t^s{}_D \tag{3.4}$$

The arrival time from the direct and the reflected signals have almost the same value due to the high speed at which the signals travel. Figure 3.2 shows

samples of clock bias estimates in meters for different common clocks relative to GPS Time.

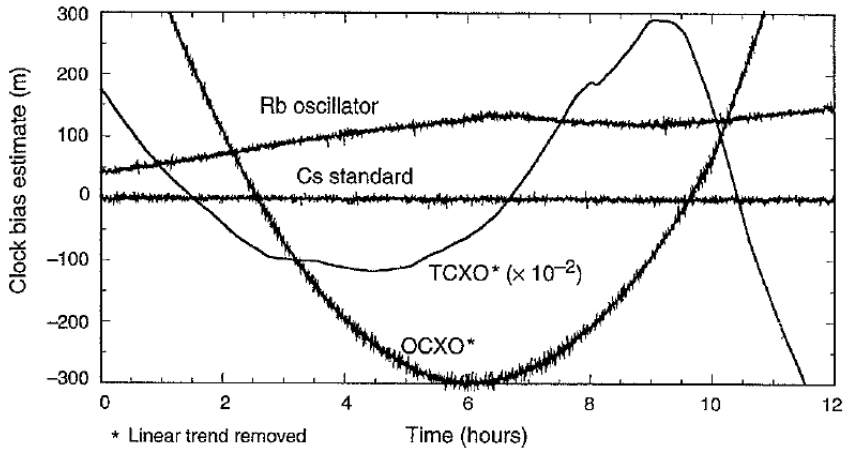

Figure 3.2. Changes in Clock Bias of Four Receiver Clocks Relative to GPS Time [24]

- The arrival time from the direct and the reflected signals are so close to each other that the difference between the respective CYGNSS receiver clock bias is small enough to be negligible:

$$\delta t_u(t_R - t_D) \approx 0 \tag{3.5}$$

From the assumptions (3.4) and (3.5), the clock bias terms disappear and equation (3.3) turns to be:

$$\rho_R - \rho_D = c\,(\Delta\tau_{rel}) = r_R - r_D + I_R - I_D + T_R - T_D + \varepsilon_R - \varepsilon_D \tag{3.6}$$

True Range Terms – Referring back to Figure 3.1, some analysis needs to be considered in order to approach the true range terms. Note that the GPS satellite is so far away relative to the CYGNSS satellite that the signal waves are practically straight lines, or plane wave fronts, when they arrive at CYGNSS altitude. Therefore, we can suppose that the direct and reflected signal ray paths are parallel to each other when they reach to CYGNSS height. Note that bending of the raypath due to propagation through plasma is neglected as insignificant.

- By inspecting the reflected signal range r_R on Figure 3.1, one can split its path into two different segments. The first segment, which starts at the GPS satellite and ends at the intersection with the perpendicular signal wave that crosses the CYGNSS satellite, has basically the same length as the total path of the direct signal r_D; both are colored orange. The remaining segment on the reflected signal is called the extra geometric range Δr, in purple. Therefore:

$$r_R = r_D + \Delta r \tag{3.7}$$

Ionospheric Terms – Referring to the ionospheric terms, observe that there is a limit that separates two different regions.

- Above the CYGNSS altitude, the reflected signal sweeps the same ionospheric region heights as the direct signal but with a horizontal

delay variation ΔI. Below the CYGNSS altitude, the reflected signal travels through the densest ionospheric layers and encounters a significant amount of electron density, which can be grouped as I_{below}. Thus,

$$I_R = I_D + \Delta I + I_{below} \tag{3.8}$$

Other Terms – The tropospheric delay for direct signal T_D is actually zero since the troposphere starts at an altitude much lower than the CYGNSS altitude.

$$T_D = 0 \tag{3.9}$$

Lastly, we define the difference between the two measurement errors as:

$$\varepsilon_R - \varepsilon_D = \Delta\varepsilon \tag{3.10}$$

3.3 Measurement Model

Finally, after applying the assumptions from equations (3.7) to (3.10) to the equation (3.6), the derived measurement model is as follows:

$$\rho_R - \rho_D = c\,(\Delta\tau_{rel}) = \Delta r + \Delta I + I_{below} + T_R + \Delta\varepsilon \tag{3.11}$$

where,

$\Delta\tau_{rel}$ is the apparent transit time of the reflected signal relative to the direct or the needed time to make the extra geometric range path

Δr is the extra geometric range corresponding to the scattering segment of the reflected signal raypath

ΔI is the horizontal ionospheric delay variation of the reflected signal relative to the direct signal at CYGNSS height

I_{below} is the delay associated with the reflected signal through the ionosphere below the CYGNSS height

T_R is the delay associated with the reflected signal transmission through the troposphere

$\Delta\varepsilon$ is the relative code phase measurement error

In practice,

$$\Delta I + I_{below} = c\,(\Delta\tau_{rel}) - \Delta r - T_R - \Delta\varepsilon \tag{3.12}$$

On the left-hand side, ΔI and I_{below} are the ionospheric estimations to retrieve as the outputs from the measurement model. Given there is only one measurement for a single line-of-sight at a given instant, it may not be possible to separate ΔI and I_{below} without additional assumptions, in practice. On the right-hand side, $\Delta\tau_{rel}$ is the input value of the measurement model and is obtained

from the maximum correlation function value on the DDM as shown in Figure 3.3 generated onboard the CYGNSS satellite.

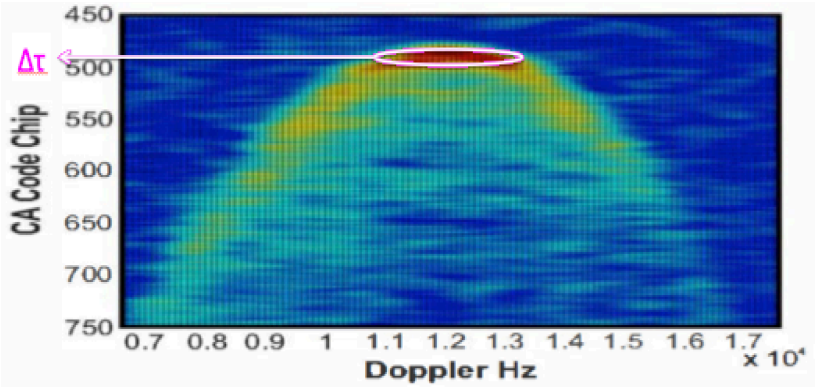

Figure 3.3. Measured DDM Obtained from the UK-DMC-1 Mission ([29], annotated with edits)

Δr and T_R can be computed by using accurate Earth ocean-surface and tropospheric models respectively. For the ionospheric components, the use of ionospheric models is helpful to estimate the magnitude of anticipated electron content, which applied with some assumptions on ΔI, will contribute to separate and solve for I_{below}.

The following chapters are focused on modeling each term of the measurement model with the objective of retrieving the ionospheric parameters.

CHAPTER 4

SPECULAR POINT AND RAYPATH COMPUTATIONS

The objective of this chapter is to solve for the extra geometric range term Δr from the measurement model obtained in Chapter 3. In order to get the ionospheric terms, which are the outputs of the formulated mathematical model, all the other terms from the measurement model need to be solved. Therefore, to simplify the problem, the following chapters will focus on the computation of the case study of one satellite pair, of a GPS transmitter and a CYGNSS receiver, at one instant.

This chapter analyzes the extra geometric range by computing the location of the *specular point*, which is an indispensable key to move forward on this project.

The first section describes satellite positioning for the GPS transmitter and the CYGNSS receiver on a certain date by using satellite ephemeris almanac files. The second section introduces the definition of the specular point and presents different approaches to obtain its exact location. The method of solution is explained in detail as well as the important considered assumptions.

Finally, validations are performed to ensure the reliability of the obtained results by introducing real inputs. Critical judgments are made after plotting the results illustratively, which are helpful in understanding better and interpreting the results.

4.1 Satellite Positioning

The geometrical problem starts with obtaining GPS and CYGNSS satellite positions. In order to get information about the satellites, this section makes use of *almanac* files that contain the ephemerides to compute the position of satellites in orbit. Actual ephemeris data are introduced to engineering tools, such as Matlab and STK, to estimate GPS and CYGNSS positions.

4.1.1 The Almanac. The almanac is a subset of the clock and ephemeris data that every GPS satellite transmits. It includes information about the state or health of the entire GPS constellation as well as a coarse version of the ephemeris of all satellites in orbit [24]. This ephemeris data can be propagated to retrieve an estimated position of each GPS satellite. The almanac allows a receiver to determine approximately when a satellite rises above the horizon, given an approximate user position, so that the receiver can plan to initiate signal acquisition. Almanac parameters do not provide accurate positions as the ephemeris parameters do. However, this project computes the satellite positions by using almanac parameters since the main objective is simply to illustrate the capability of GNSS – Reflectometry for ionospheric remote sensing.

The Yuma almanac provides a quasi-Keplerian parameter set used for propagation along with other information [13]. One of the advantages of using Yuma almanac is that it is a standard widely-used format.

The temporal reference in which the Yuma almanac is defined is under the basis of GPS Time (GPST). GPST is described by the basis of measurements from a set of cesium and rubidium frequency standards in use at the monitor stations and aboard the satellites. A time epoch in GPST is defined in terms of the week number and number of seconds into the week, which is the time of applicability *toa* [24].

The Keplerian parameter set required for orbital propagation is limited to seven parameters: eccentricity, orbital inclination, rate of right ascension, square root of semi-major axis, longitude of ascending node, argument of perigee, and mean anomaly, all specified at a common reference time *toa*. The Yuma almanacs can be obtained at the official Navigation Center website [13].

4.1.2 Solution Method. Two different engineering tools are used to implement the Yuma almanac data. Both take an almanac file as the input and retrieve satellite positions over time as the output.

MATLAB. This programming language is used to write the algorithm that calculates GPS transmitter positions from almanac data. The algorithm reads through the almanac file and saves each of the ephemeris parameters into a Matlab variable. Before proceeding with the computations, the number of weeks is converted into units of seconds. Then, the algorithm starts with the calculation of different orbital parameters to locate the GPS satellite position. The procedure is to utilize a variation of equations available in Table 20-IV from

[18]. Afterward, the position coordinates of the GPS satellite are retrieved for a determined instant of time in the Earth-Centered, Earth-Fixed (ECEF) frame.

The CYGNSS satellite positions are not computed by this method since there are no available ephemeris data yet. Note that the CYGNSS satellites are still in the design stage [27].

STK. Satellite Took Kit (STK) consists of a physics-based software package from Analytical Graphics, Inc., which allows engineers to perform complex analyses of space assets. The software displays the GPS constellation by reading an almanac file. It is capable of simulating each of the satellites' motions by propagating the orbital elements over time. STK retrieves GPS satellite positions in the ECEF coordinate system. In addition, this software allows the implementation of customized satellites, which makes it easier to work with partially constrained satellite constellations, such as CYGNSS, that are still in the design phase.

Coordinate Frames. The satellite position outputs are given in the World Geodetic System (WGS 84) Earth-Centered, Earth-Fixed (ECEF) coordinate system shown in Figure 4.1. The WGS 84 is a standard for use in cartography, geodesy, and navigation. It comprises a coherent set of global models and definitions [18]:

- An ECEF Cartesian coordinate frame for the Earth.
- An ellipsoidal reference surface model of the shape of the Earth.

- A gravitational equipotential surface called *geoid* that defines the nominal sea level.

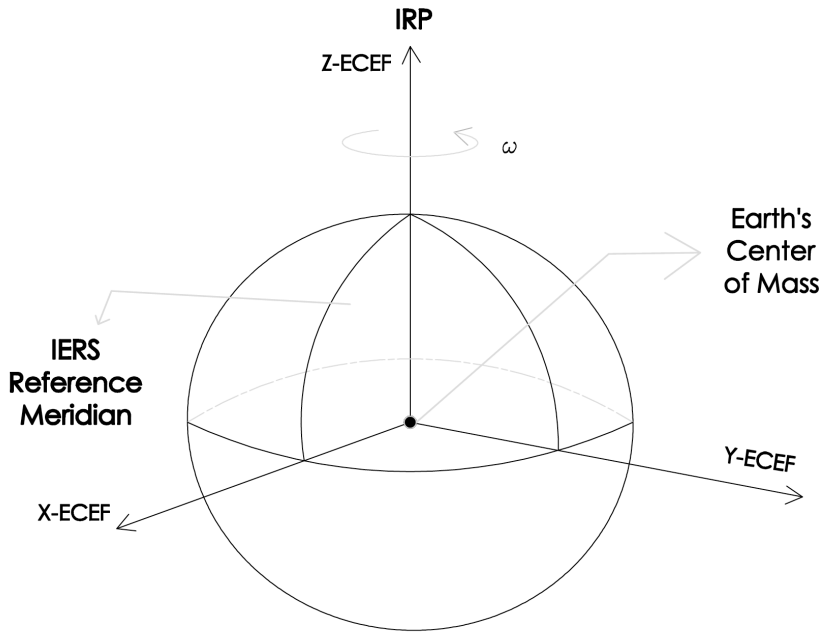

Figure 4.1. WGS 84 Reference Frame

The WGS 84 surface is an oblate spheroid with an equatorial semi-major axis of a = 6,378,137 m and a flattening of f = 1/(298.257 223 563). The polar semi-minor axis is $b = a(1-f)$ = 6,356,752.3142 m.

4.1.3 Actual Data and Results. The GPS Yuma almanac file used as input for this project was generated on week 1,738 at *toa* = 319,488 s, which corresponds to May 1st 2013 at 16:44:48.00 UTC. For simplicity, only one GPS satellite is considered: PRN 1. The parameter values of the Yuma almanac for PRN 1 are represented in Table 4.1.

Table 4.1. Yuma Almanac Parameters for PRN 1

Parameter	Value
ID	01
Health	000
Eccentricity	0.1793384552E-002
Time of Applicability (s)	319,488.0
Orbital inclination (rad)	0.9600346856
Rate of Right Ascension (rad/s)	-0.7851755629E-008
Sqrt of Semi-Major Axis ($m^{1/2}$)	5,153.645508
Right Ascension at Week (rad)	-0.9638972013
Argument of Perigee (rad)	0.274960813
Mean Anomaly (rad)	0.2218360174E+001
Af0 (s)	0.0000000000E+000
Af1 (s/s)	0.0000000000E+000
Week	714

Basic ephemerides for CYGNSS are already defined, shown in Table 4.2 [29]. Thus, a hypothetical configuration of the CYGNSS satellites is simulated in STK under the constraints of Table 4.2.

Table 4.2. Orbital Parameters from the CYGNSS Constellation

Parameter	Value
# Micro-Satellites	8
Altitude (m)	500,000
Orbital Inclination (deg)	35
Eccentricity	≈ 0

One of the assumptions made in this case study is that the eight LEO micro-satellites will be evenly distributed around the orbital plane. Also, it is

assumed that the Right Ascension of the Ascending Node (RAAN) is zero, which means that the direction of the orbital ascending node is aligned with the direction of the first point of Aries [7].

The implementation of these ephemerides into Matlab and STK results in the following satellite configuration illustrated in Figure 4.2:

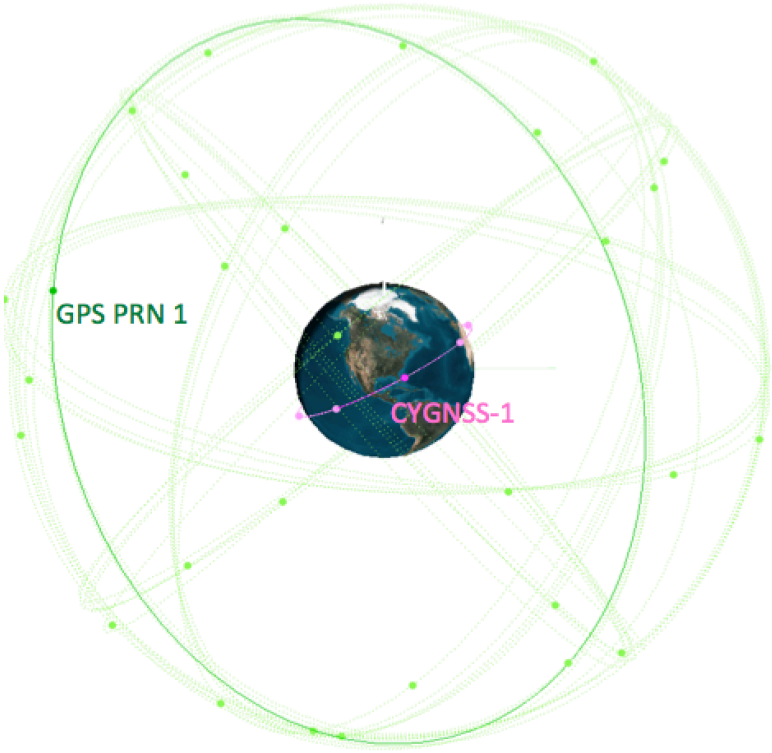

Figure 4.2. GPS and CYGNSS Satellite Constellations

The bold colored points represent the satellite set of a GPS transmitter (green) and a CYGNSS receiver (magenta).

The position values of this set of satellites at the reference epoch corresponding to May 1st 2013 at 16:44:48.00 UTC are given in Table 4.3 from the computations in Matlab and in Table 4.4 from the computations in STK.

Table 4.3. Satellite Positions in the ECEF Frame Computed in Matlab

Satellite	X_{ECEF} [m]	Y_{ECEF} [m]	Z_{ECEF} [m]
GPS PRN 1	-20,692,605.06	-10,349,329.47	13,102,459.12

Table 4.4. Satellite Positions in the ECEF Frame Computed in STK

Satellite	X_{ECEF} [m]	Y_{ECEF} [m]	Z_{ECEF} [m]
GPS PRN 1	-20,707,003.81	-10,371,941.81	13,061,947.64
CYGNSS - 1	1,311,300.64	-5,909,970.67	3,265,196.15

One can observe the presence of small discrepancies on the Matlab and STK position results. This variation comes from the fact that STK propagates the almanac orbital parameters over time while Matlab does not use any GPS propagator function. Therefore, the position values to be used for the subsequent simulations are those computed in STK. The appendix contains an error variation study between STK and Matlab that shows an agreement within 51km. It is believed that this magnitude of the variation is small enough to be considered insignificant for the subsequent raypath analyses.

4.2 Specular Point

This section defines the specular point and shows how to compute its location. First, Section 4.2.1 presents the geometrical fundamentals that describe the specular point as well as the corresponding hypotheses considered in the problem. Then, Section 4.2.2 presents different approaches to compute

this geometric point and shows the obtained plots and results. Finally, the corresponding validations are performed to ensure the reliability of the outcome.

4.2.1 Specular Point Fundamentals. The specular point is defined under the physical basis of optics. It is the location at which signal waves experience a mirror-like reflection when they strike a surface, such that rays from a single incoming direction are reflected into a single outgoing direction [12]. The specular reflection is governed by the *law of reflection* and *Fermat's principle of least time*, which are described as follows:

Law of Reflection – When an incident ray arrives at the specular point, it makes an angle with the normal to the surface called angle of incidence θ_i. In the same way, the angle that the outgoing ray makes with the normal is called angle of reflection θ_r. The law of reflection states that the incident and reflected rays lie in the same plane with the normal to the surface, and that the incident ray upon a reflective surface will have an angle of reflection equivalent to the angle of incidence [12], illustrated in Figure 4.3:

$$\theta_i = \theta_r \tag{4.1}$$

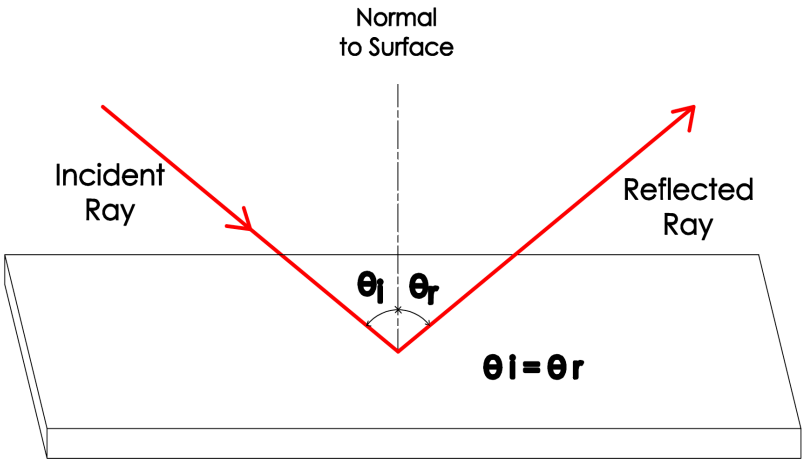

Figure 4.3. The Angle of Incidence is Equal to the Angle of Reflection

Fermat's Principle of Least Time – From all the possible paths, the specular point provides the shortest path length and time to get from the transmitter to the receiver [9].

In fact, this principle holds when the law of reflection is true and vice-versa. In order words, the statement that the angle of incidence equals the angle of reflection is equivalent to the statement that the signal wave strikes the mirror-like surface in such a way that it comes back to the receiver in the least possible time [9]. It is possible to demonstrate this equivalence by doing a small exercise in Figure 4.4.

From Fermat's principle, the objective is to find the path from A to B traversed in the shortest possible time. The straight path from A to B is shortest, but not if it is required that the wave has to strike the mirror MM' and come back.

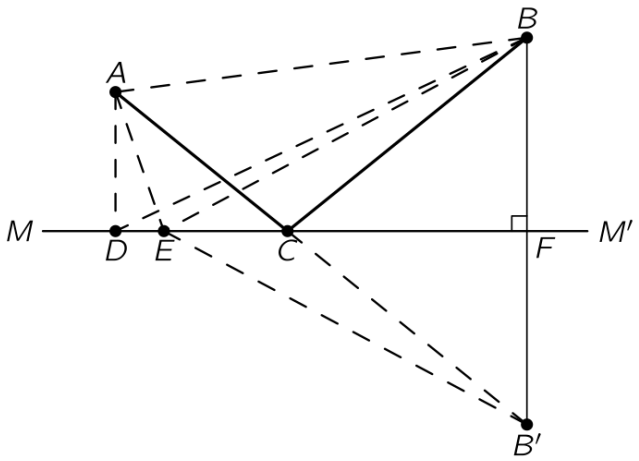

Figure 4.4. Illustration of the Principle of Least Time [9]

One possible way would be to go as fast as possible to the mirror on the path ADB, but it implies a long path DB. By moving a little to the right, to E, the first distance is slightly increased, but the second distance is greatly decreased. To find the point C for which the time is shortest, a geometrical trick needs to be used. An artificial point B' is constructed on the other side of MM'. This point B' has the same distance below the plane MM' as the point B is above the plane. Now, note that BFM is a right angle and BF = FB', so EB = EB'. Therefore the sum of AE + EB is also the sum of AE + EB'. Hence, the sum of the two lengths that gives the least distance corresponds to the line that goes through point C as a straight line from A to B'. In order words, finding the shortest reflecting path to

point B is equivalent to finding the shortest distance toward the artificial point B'. Now if ACB' is a straight line, then angle BCF is equal to angle B'CF and thence to angle ACM ($\theta_i = \theta_r$) [9].

These optics principles are broadly applied in GNSS–Reflectometry in remote sensing missions to determine geophysical properties such as the sea surface state, moisture, and snow depth [4]. For this reason, it is a key challenge to locate the specular points. In the literature, there are different methods. Wu et al., 1997 [32] devise a two-step algorithm: in the first step, an approximate nominal sea surface is assumed and in the second step a more precise surface is applied to refine the reflection point. Kostelecky et al., 2005 [22] propose an iterative approach, which assumes that the sea surface height is known to obtain a better approximation first. Guo et al., 2012 [14] present a constrained optimization problem with the associated error analysis. Even so, this project uses a different method to compute the specular point location in the following section.

4.2.2 Solution Method. As it is explained previously, there are several ways to estimate the specular point when the satellite transmitter and receiver positions are given.

Assumptions. In this project, the specular point is assumed to be positioned somewhere on the WGS 84 ellipsoid surface, which is a reasonable approximation to the Earth as the GPS receivers use this model to determine

position. The ellipsoid is used instead of the geoid of constant gravitational potential for geometric simplicity. In addition, it is supposed that there are no motions on the sea surface or phenomena that change the local sea level such as tsunamis, tides or ocean swells. Given these assumptions, there are some theoretical approaches to find the specular point under a couple of geometrical constraints.

Geometric Configuration. Given the positions of the satellite transmitter and receiver, it is possible to define a plane that contains three points: the two satellite positions and the origin of the ellipsoidal reference model as shown in Figure 4.5:

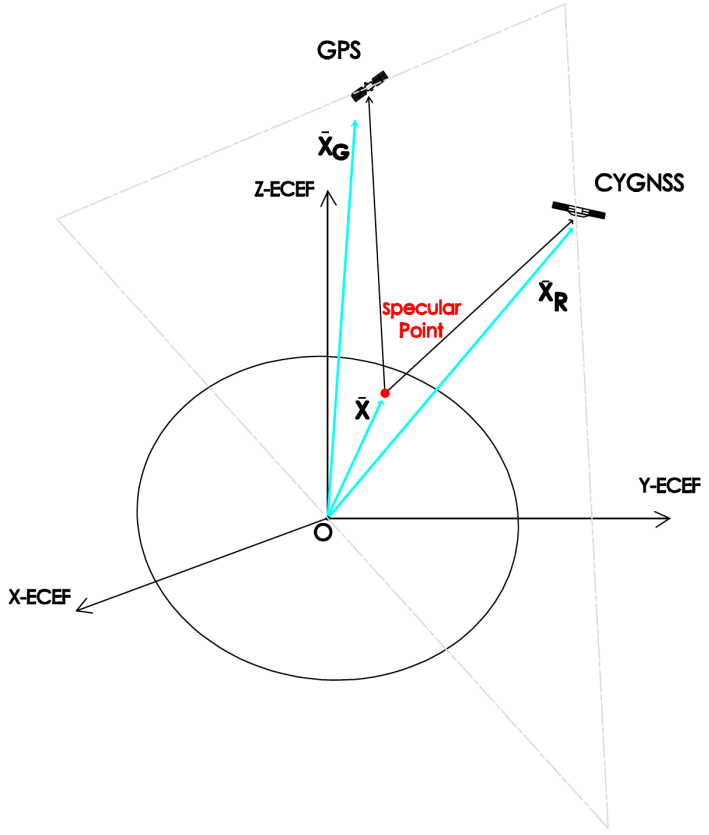

Figure 4.5. Plane that Contains the Satellite Positions and the Origin of the WGS 84 Ellipsoid Reference Model

The equation of the plane can be obtained by computing the cross product of two vectors that lie in the same plane:

$$\boldsymbol{X_G} \times \boldsymbol{X_R} = \begin{pmatrix} x_G \\ y_G \\ z_G \end{pmatrix} \times \begin{pmatrix} x_R \\ y_R \\ z_R \end{pmatrix} = \begin{pmatrix} y_G z_R - z_G y_R \\ z_G x_R - x_G z_R \\ x_G y_R - y_G x_R \end{pmatrix} \tag{4.2}$$

From (4.2) the constants of the plane equation are defined:

$$Ax + By + Cz + D = 0 \tag{4.3}$$

where $\mathbf{X} = (x, y, z)^T$ is the unknown position vector of the specular point and *A*, *B*, *C* and *D* are constant terms of the equation of the plane with the following values:

$$\begin{bmatrix} A \\ B \\ C \\ D \end{bmatrix} = \begin{bmatrix} y_G z_R - z_G y_R \\ z_G x_R - x_G z_R \\ x_G y_R - y_G x_R \\ -(Ax_G + By_G + Cz_G) \end{bmatrix} \tag{4.4}$$

The reference ellipsoid for the surface of the Earth can be expressed as:

$$\frac{x^2}{a^2} + \frac{y^2}{a^2} + \frac{z^2}{b^2} = 1 \tag{4.5}$$

where,

a is the semi-major axis of the WGS 84 ellipsoid (*a* =6,378,137 m)

b is the semi-minor axis of the WGS 84 ellipsoid (*b* =6,356,752.314 m)

Once these two geometric configurations are defined, two methods for solving specular points can be defined.

Optimization Problem – This approach applies the *Fermat's principle of least time*. The method of Lagrange multipliers is used to minimize the total path length of the reflected signal r_R that goes from the GPS satellite and bounces at the specular point to the CYGNSS satellite. The non-linear function to be minimized is the following equation:

$$r_R = f(x,y,z) = \sqrt{(x_G - x)^2 + (y_G - y)^2 + (z_G - z)^2} + \\ + \sqrt{(x_R - x)^2 + (y_R - y)^2 + (z_R - z)^2} \tag{4.6}$$

Where the first square root term corresponds to the incoming ray-path to the specular point and the second term is associated to the outgoing ray-path. The total path length function is subject to the geometrical constraints described above as equations (4.3) and (4.5), which means that the specular point has to lie on the curve at which the plane and the ellipsoid intersect:

$$g_1(x,y,z) - c_1 = Ax + By + Cz + D \tag{4.7}$$

$$g_2(x,y,z) - c_2 = \frac{x^2}{a^2} + \frac{y^2}{a^2} + \frac{z^2}{b^2} - 1 \tag{4.8}$$

Since there are two constraints, the method introduces two new variables λ_1 *and* λ_2 called Lagrange multipliers. Therefore, the Lagrange function or Lagrangian in this problem is defined by:

$$\Lambda\,(x, y, z, \lambda_1, \lambda_2) = f(x, y, z) + \lambda_1(g_1(x, y, z) - c_1) + \lambda_2(g_2(x, y, z) - c_2) \tag{4.9}$$

By taking the gradients of equation (4.9) respect to each of the variables, the five unknowns can be retrieved by solving the system of five equations:

$$\boldsymbol{\nabla}_{x,y,z,\lambda_1,\lambda_2}\,\Lambda\,(x, y, z, \lambda_1, \lambda_2) = \mathbf{0} \tag{4.10}$$

Vector Approach – This method uses the *law of reflection*. If the angles of incidence and reflection are equivalent with respect to the normal vector to the ellipsoid surface, the cross product between the vector pointing to GPS and the normal vector to the ellipsoid should have the same magnitude as the cross product between the normal vector and the vector pointing to the CYGNSS satellite. Figure 4.6 is a representation of the problem scenario:

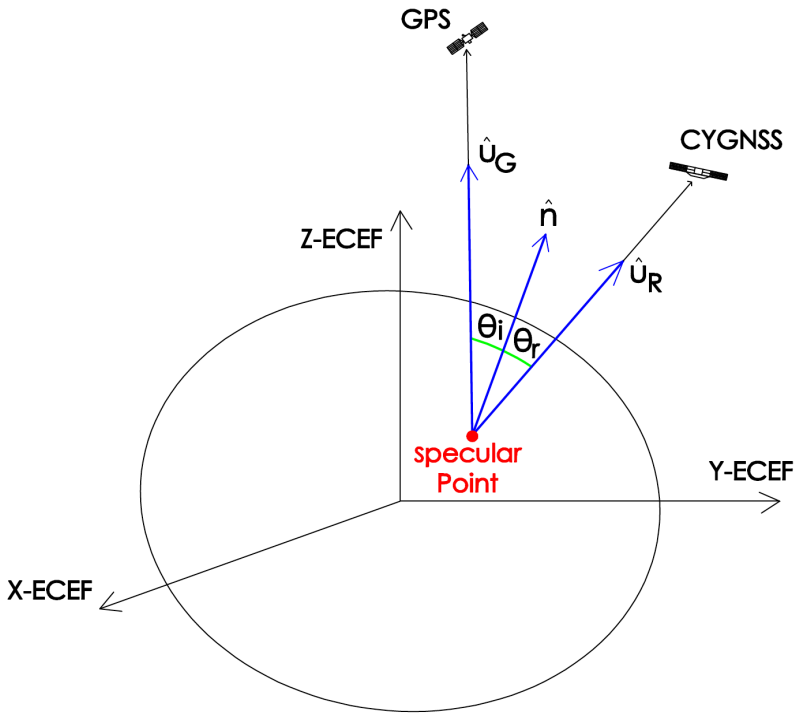

Figure 4.6. Representation of Vectors that Define a Specular Reflection

From the representation, $\mathbf{u_G}$ and $\mathbf{u_R}$ are unit vectors that points to the GPS and the CYGNSS receiver satellites respectively and $\mathbf{n}$ is the normal vector to the ellipsoid surface.

The cross products corresponding to the angles of incidence and reflection are:

$$\left.\begin{aligned} \boldsymbol{u_G} \times \boldsymbol{n} &= |u_G|\,|n|\,sin\theta_i\,\hat{\boldsymbol{b}} \\ \boldsymbol{n} \times \boldsymbol{u_R} &= |u_R|\,|n|\,sin\theta_r\,\hat{\boldsymbol{b}} \end{aligned}\right\} \tag{4.11}$$

The vector norms have unit value and the right-hand sides from the two equations in (4.11) are equivalent in magnitude and direction due to the *law of*

reflection. Therefore, this relationship enforces the coplanar requirement among the three vectors in the cross product equations. Consequently, the left-hand sides are also equivalent and the system of equations end up to be an equality of two cross products:

$$\boldsymbol{n} \times \boldsymbol{u_R} - \boldsymbol{u_G} \times \boldsymbol{n} = \begin{bmatrix} (u_{G_z} + u_{R_z})\, n_y + (u_{G_y} + u_{R_y})\, n_z \\ -(u_{G_z} + u_{R_z})\, n_x + (u_{G_x} + u_{R_x})\, n_z \\ (u_{G_y} + u_{R_y})\, n_x - (u_{G_x} + u_{R_x})\, n_y \end{bmatrix} = \begin{bmatrix} 0 \\ 0 \\ 0 \end{bmatrix} \tag{4.12}$$

The system in (4.12) consists of three non-linear equations in which each of the terms depends implicitly on the three unknowns $(x, y, z)^T$ that correspond to each of the position components of the specular point. The relationship between the terms from (4.12) and $(x, y, z)^T$ are shown in (4.13) and (4.15). Solving the system of three equations can retrieve the three unknown variables.

The unit vectors $\mathbf{u_G}$ and $\mathbf{u_R}$ that point to the satellites are described as:

$$\boldsymbol{u_G} = \frac{(\, x_G - x\,,\ y_G - y,\ z_G - z\,)}{\sqrt{(x_G - x)^2 + (y_G - y)^2 + (z_G - z)^2}} \qquad \boldsymbol{u_R} = \frac{(\, x_R - x\,,\ y_R - y,\ z_R - z\,)}{\sqrt{(x_R - x)^2 + (y_R - y)^2 + (z_R - z)^2}} \tag{4.13}$$

The normal vector $\mathbf{n}$ to the ellipsoid surface can be defined by computing partial derivatives on the ellipsoid expression:

$$f(x, y, z) = \frac{x^2}{a^2} + \frac{y^2}{a^2} + \frac{z^2}{b^2} - 1 \tag{4.14}$$

The gradient vector of (4.14), which is the normal vector to the ellipsoid surface, results in:

$$\boldsymbol{n}(x,y,z) = \frac{\boldsymbol{\nabla} f(x,y,z)}{\|\boldsymbol{\nabla} f(x,y,z))\|} \tag{4.15}$$

where,

$$\boldsymbol{\nabla} f(x,y,z) = \langle \frac{2x}{a^2}, \frac{2y}{a^2}, \frac{2z}{b^2} \rangle \tag{4.16}$$

In practice, there are other tools in the literature that solve for the positions of the specular points. The one used for this study is presented next.

Numerical Method – Garrison [11] has developed an algorithm that works with the numerical *Nelder-Mead method* to minimize the total path of the reflected signal through the specular point, so that it retrieves the longitude and latitude of the specular point position on the WGS 84 ellipsoid surface. Therefore, it is assumed again that the nominal sea level reminds constant.

The algorithm takes the positions of the transmitter and receiver satellites as inputs, followed by a definition of satellite pointing vectors centered at the ellipsoid origin. Then, the code verifies if the transmitter satellite is visible with respect to the receiver satellite. The minimum required angle of the GPS satellite above the horizon of the LEO satellite is conventionally set at five degrees. After that, the algorithm enters an iterative loop seeking the actual latitude and longitude of the specular point position. The initial guess for the latitude and longitude of the specular point position is set to the geographic coordinates of the receiver satellite. This is a reasonable assumption since the

actual latitude and longitude of the specular point will be close to the geographic coordinates of the LEO receiver satellite.

The initial latitude and longitude values define a dummy specular point position on the WGS 84 ellipsoid by transforming from geodetic coordinates to the ECEF frame $(x, y, z)^{T}$. Thus, a hypothetical path length can be computed by summing the distances from the initial guess specular point to the transmitter and the receiver as in equation (4.6). Then, the resulting path length is introduced to a minimization function based on the nonlinear optimization technique called *Nelder-Mead method*, which minimizes an objective function in a multi-dimensional space [25]. Figure 4.7 is a visual illustration of the iteration method with the objective to find the specular point location:

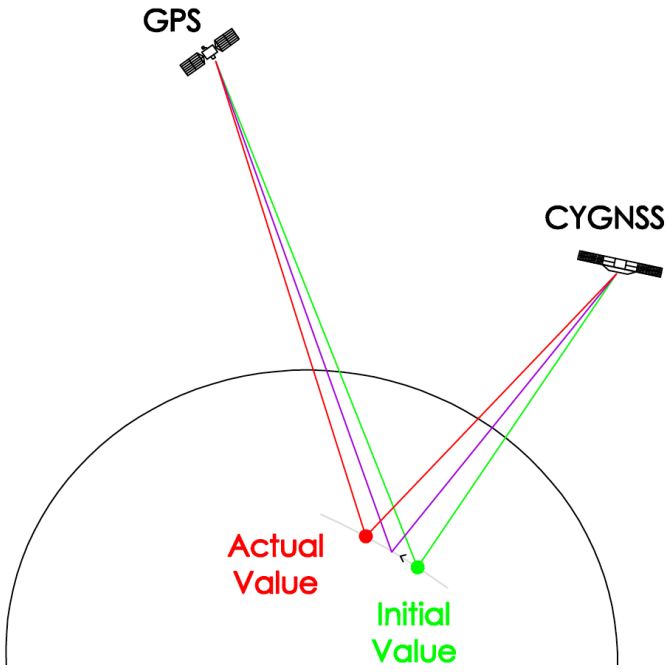

Figure 4.7. Illustration of the Iteration Method for Finding the Specular Point

The iteration converges to one geographic solution. Before the algorithm provides the final outputs, a small correction to the results may be necessary, since there are occasions in which the obtained latitude and longitude angles converge in the wrong quadrant.

4.2.3 Results and Validations. This project uses the numerical method explained in the section above to compute the location of the specular point. The inputs to be used in the numerical algorithm are the GPS and CYGNSS satellite positions represented in Table 4.5, which correspond to the reference epoch May 1st 2013 at 18:12:00.00 UTC. The specular point position is given in the geodetic latitude ϕ and longitude λ:

Table 4.5. Calculated Specular Point Location in the ECEF Frame and Geographic Coordinates with Given Satellite Positions

Inputs / Outputs	X_{ECEF} [km]	Y_{ECEF} [km]	Z_{ECEF} [km]	Φ [deg]	λ [deg]
GPS PRN 1	-22,488.658	-13,987.206	-2,560.537	-	-
CYGNSS – 1	-3,908.103	-5,339.442	1,877.727	-	-
SPECULAR POINT	-3,847.534	-4,851.718	1,523.908	13.92	231.58

This set of satellites is the case study examined for all the analyses in the Chapters 5 and 6.

The specular point is located on the northern hemisphere at the third quadrant in the ECEF frame. Figure 4.8 shows a 3-D representation of the reflected signal path through the specular point. It illustrates the GPS and

CYGNSS satellite positions and the reflected wave path striking the specular point on the WGS 84 ellipsoid surface.

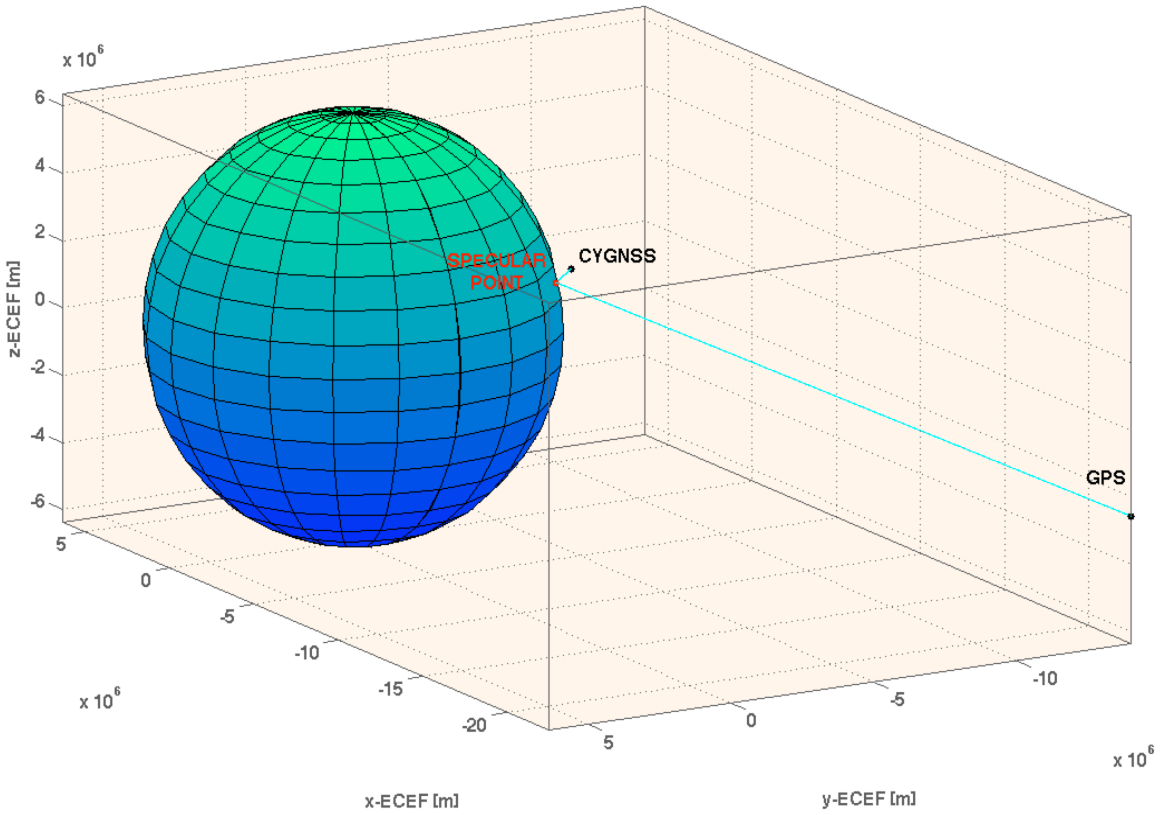

Figure 4.8. 3-D Representation of the Reflected Signal Path between the Satellites and the Calculated Specular Point Location on the WGS Ellipsoid

Note that the geographic latitude and longitude coordinates of the specular point are close to the CYGNSS satellite ones as expected in the numerical algorithm when the initial guess values were set.

Validations – To ensure the reliability of the obtained results, four validation studies are conducted to check if the geometrical configuration of the case study meets the requirements of basic optics given in section 4.2.1.

Validation 1. As seen in this Chapter, the *Law of Reflection* states that the angle at which the ray path is reflected θ_r at the specular point is the same angle at which the ray path arrives θ_i. Therefore, similarly to the vector approach described in Section 4.2.2, the dot product between the normal vector to the ellipsoid **n** and the vector pointing to the GPS satellite $\boldsymbol{u_G}$ should retrieve the same scalar as the dot product between the normal vector to the ellipsoid $\boldsymbol{n}$ and the vector pointing to the CYGNSS satellite $\boldsymbol{u_R}$:

$$\left.\begin{aligned} \boldsymbol{n} \cdot \boldsymbol{u_G} &= |n|\,|u_G|\,cos\theta_i \\ \boldsymbol{n} \cdot \boldsymbol{u_R} &= |n|\,|u_R|\,cos\theta_r \end{aligned}\right\} \tag{4.17}$$

From which the required condition is:

$$cos\theta_i = \frac{\boldsymbol{n} \cdot \boldsymbol{u_G}}{|n|\,|u_G|} = \frac{\boldsymbol{n} \cdot \boldsymbol{u_R}}{|n|\,|u_R|} = cos\theta_r \tag{4.18}$$

The agreement with the *Law of Reflection* condition is shown in Table 4.6, which ensures the equality of angles of incidence and reflection:

Table 4.6. Validation of Law of Reflection

Angle	Dot Product (*cosθ)*	Value [deg]
Angle of incidence θ_i	0.813356	35.575
Angle of reflection θ_r	0.813349	35.576

Validation 2. The other important requirement to meet is the *Fermat's principle of least time*. The location of the specular point leads to the shortest path length and time to get from the transmitter to the receiver satellites. The path length r_R of the reflected signal can be calculated by using equation (4.6). Therefore, small increments of latitude $\Delta\phi$ and longitude $\Delta\lambda$ are added or subtracted to the geographic coordinates of the obtained specular point position in Table 4.7 to show that the original specular point corresponds to the shortest path length r_R, which is 21,762,883.534 m.

Table 4.7. Comparative of Total Path Length Values for Differential Positions with respect to the Specular Point Location

ΔΦ [deg]	Δλ [deg]	r_R [m]
0	0	21,762,883.534
+0.001	0	21,762,883.544
+0.002	0	21,762,883.626
-0.001	0	21,762,883.544
-0.002	0	21,762,883.627
0	+0.001	21,762,883.542
0	+0.002	21,762,883.617
0	-0.001	21,762,883.545
0	-0.002	21,762,883.624

Validation 3. This validation comprises the first two presented requirements and tests if the retrieved location of the specular point matches with the expected one by setting a simple geometrical satellite configuration. The proposed scenario consists of two satellites, one transmitter and one

receiver, at same heights but at opposed longitudes, that is 180 degrees apart from each other. This way, the specular point is expected to be located at one of the poles of the ellipsoid surface. The results of this configuration are represented analytically in Table 4.8 and illustratively in Figure 4.9:

Table 4.8. Validation for the Expected Specular Point Location in the ECEF Frameand Geographic Coordinates when Given Two Opposed Satellites

Inputs / Outputs	X_{ECEF} [km]	Y_{ECEF} [km]	Z_{ECEF} [km]	Φ [deg]	λ [deg]
TRANSMITTER	-7,378.000	0	11,378.000	-	-
RECEIVER	7,378.000	0	11,378.000	-	-
SPECULAR POINT	-8.7E-5	3.4686E-8	6,356.752	90.00	180.00

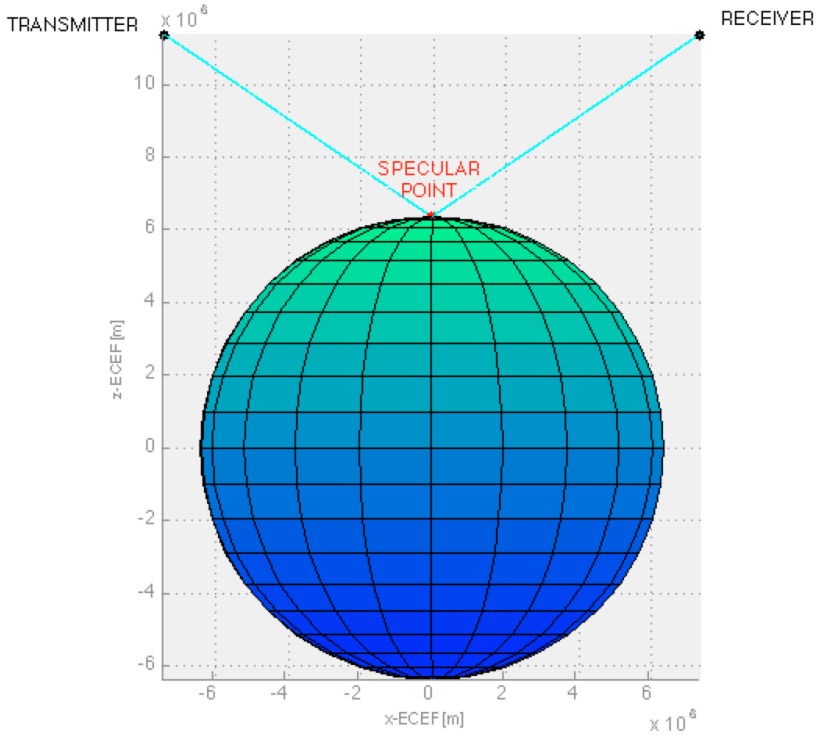

Figure 4.9. Representation of the Expected Specular Point Location at the Northern Pole of the WGS Ellipsoid with Two Opposed Satellites

Validation 4. Finally, the last validation has the purpose of filtering specular point results. Bear in mind that GPS L-band signals undergo specular reflections only on surfaces that are mirror-like for that wavelength, such as water, but not land. Hence, the obtainment of a specular point location only makes sense when it is on the ocean surface of the Earth. Therefore, a filter of results is performed with the aid of an algorithm that contains the continent profiles of the Earth. This algorithm tests whether a given specular point position is enclosed by any continent contour or not. The positions that are bounded should be discarded. Figure 4.10 illustrates on the world map the specular point location obtained from the results:

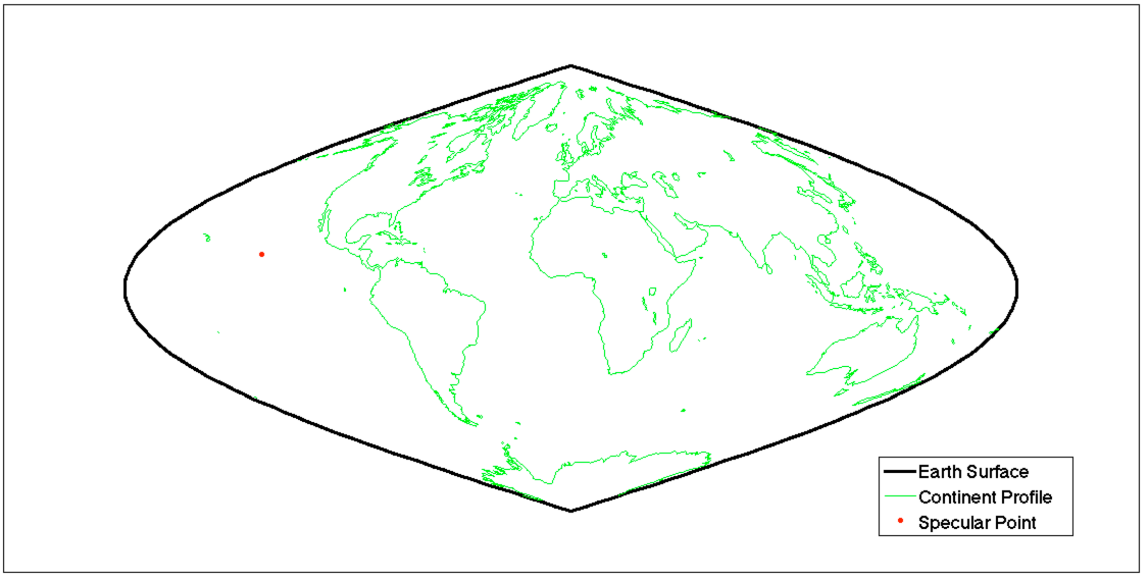

Figure 4.10. Illustration of the Specular Point Location on the World Map

In this case, the specular point is located on water, particularly on the Pacific Ocean. Consequently, specular reflections are effective at this point and the CYGNSS satellite receives scattered signals. For this reason, the results for

this case study can be used for the ionospheric measurement model obtained in Chapter 3.

4.3 Extra Geometric Range

Now it is possible to compute the extra geometric range term Δr in the ionospheric measurement model (3.11) obtained in Chapter 3:

$$\rho_R - \rho_D = c\,(\Delta\tau_{rel}) = \Delta r + \Delta I + I_{below} + T_R + \Delta\varepsilon \tag{4.19}$$

Recall that Δr is defined as the difference between the total path lengths corresponding to the reflected signal r_R and the direct signal r_D respectively:

$$\Delta r = r_R - r_D \tag{4.20}$$

Where the direct path r_D goes from the GPS satellite to the CYGNSS satellite and can be derived as:

$$r_D = \sqrt{(x_G - x_R)^2 + (y_G - y_R)^2 + (z_G - z_R)^2} \tag{4.21}$$

The reflected signal r_R goes from the GPS satellite and bounces on the ocean surface through the specular point to the CYGNSS satellite. The derivation of r_R is found in (4.6).

The results for the two ray-paths r_D and r_R and the extra geometric range Δr are listed in Table 4.9 and illustrated in Figure 4.11:

Table 4.9. Extra Geometric Range Value with the Corresponding Direct and Reflected Path Lengths

Ray Path	Length [km]
r_R	21,762.884
r_D	20,969.479
Δr	793.405

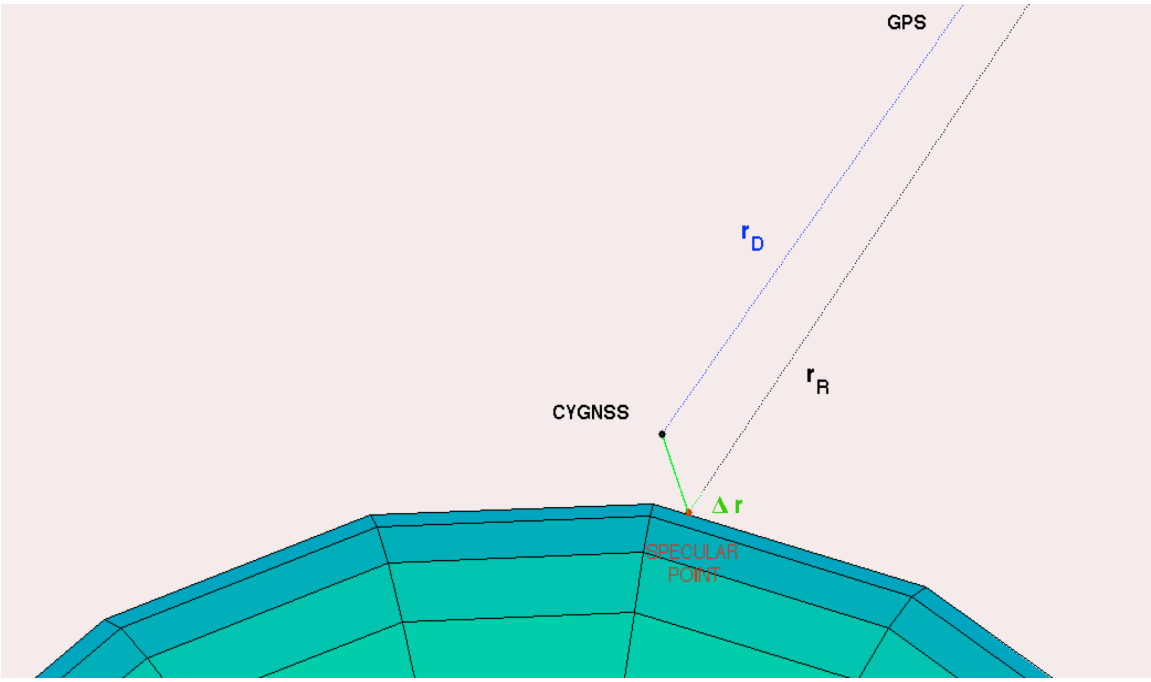

Figure 4.11. 3-D Representation of the Extra Geometric Range and the Direct and Reflected Signal Paths on the WGS-84 Ellipsoid

Note that the extra geometric range Δr represented in Figure 4.11 starts at some point on the reflected signal before arriving at the specular point. Also, notice that the direct and reflected signal paths are almost parallel to each other

due to the fact that the emission source is at a long distance. Recall that this is one of the assumptions made in the development of the measurement model in Chapter 3.

4.3.1 Configuration Cases. Actually, there exist three different cases when representing Δr. Each of the cases depends on the satellite position configuration. Consider that the reflected signal can be split into two different segments: the segment that goes from the transmitter satellite to the specular point r_{R1}, and the segment that goes from the specular point to the receiver satellite r_{R2}.

Case I – Δr starts at some point before arriving at the specular point. This configuration, represented in Figure 4.12, takes place when the direct signal path is shorter than the first segment of the reflected path:

$$r_D < r_{R1} \tag{4.22}$$

As results, the angles of incidence and reflection are constrained to a lower value than 45 degrees:

$$\theta_i = \theta_r < 45\, deg \tag{4.23}$$

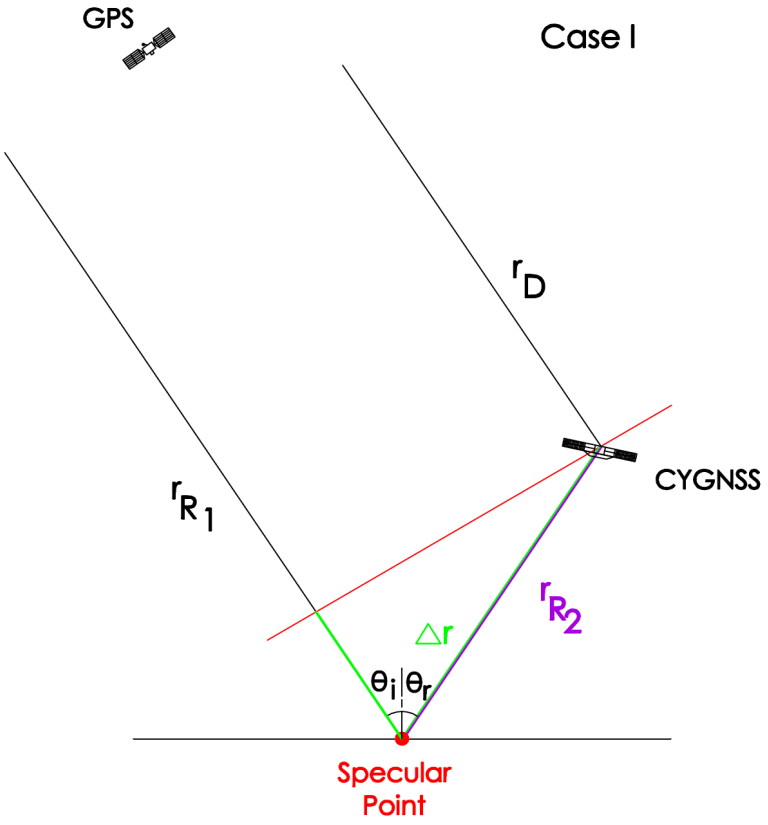

Figure 4.12. Extra Geometric Range Representation for Case I

Case II – *Δr* starts at the specular point. This configuration, represented in Figure 4.13, takes place when the direct signal path is equivalent to the first segment of the reflected path:

$$r_D = r_{R1} \tag{4.24}$$

As results, the angles of incidence and reflection are constrained to 45 degrees.

$$\theta_i = \theta_r = 45\, deg \tag{4.25}$$

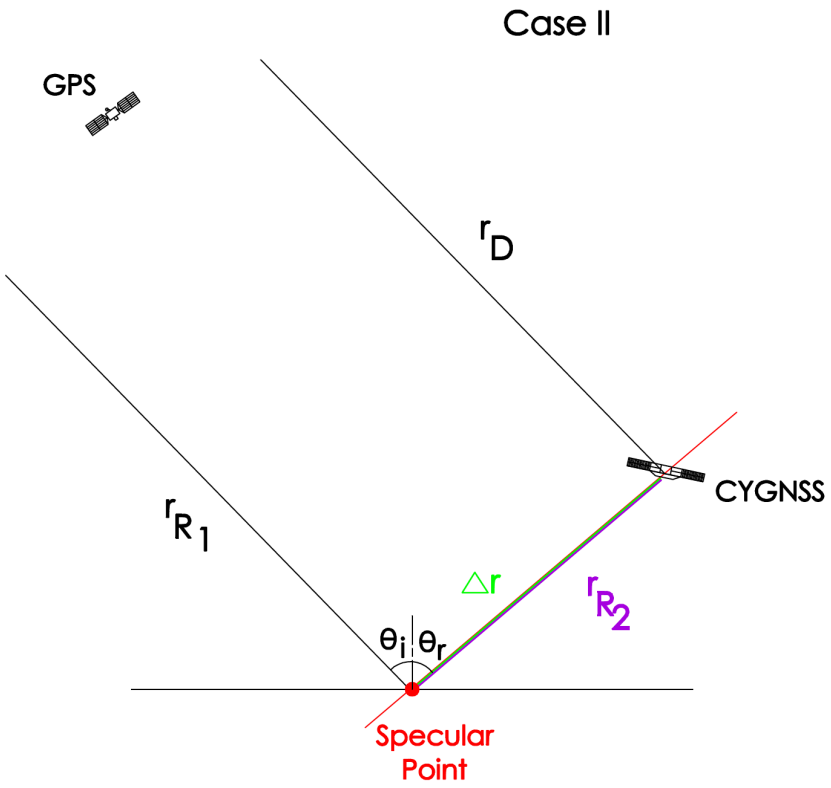

Figure 4.13. Extra Geometric Range Representation for Case II

Case III – Δr starts at some point after leaving the specular point. This configuration, represented in Figure 4.14, takes place when the direct signal path is longer than the first segment of the reflected path.

$$r_D > r_{R1} \tag{4.26}$$

As a result, the angles of incidence and reflection are constrained to a higher value than 45 degrees.

$$\theta_i = \theta_r > 45\, deg \tag{4.27}$$

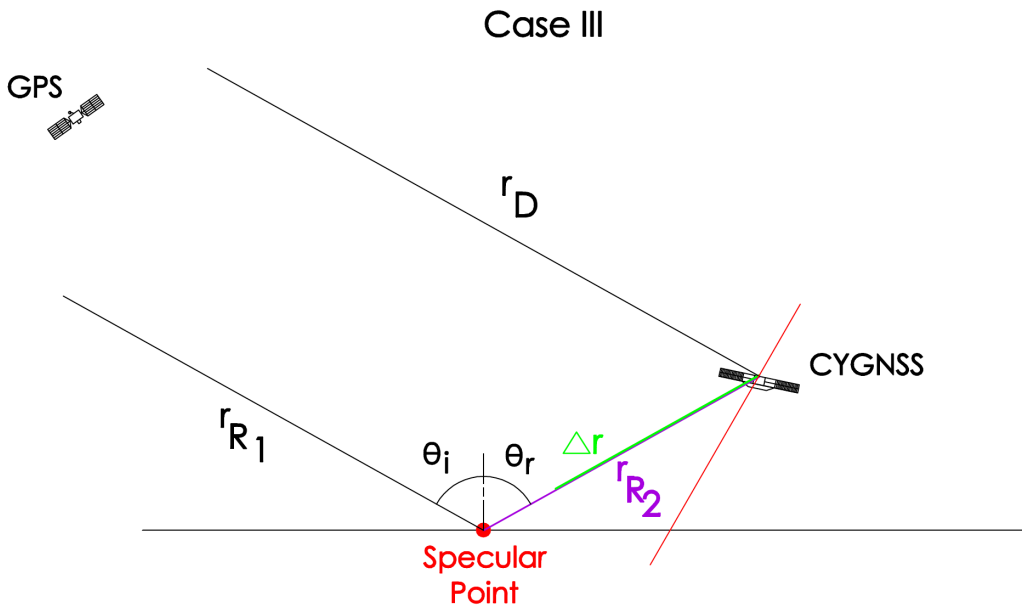

Figure 4.14. Extra Geometric Range Representation for Case III

CHAPTER 5

TROPOSPHERIC DELAY ESTIMATION

Chapter 5 presents the calculations for obtaining an estimate of the tropospheric delay term present in the ionospheric measurement model shown in Chapter 3.

Tropospheric refraction of electromagnetic signals is induced by the neutral part of the atmosphere, where there are negligible numbers of ionized particles. It is primarily composed of nitrogen and oxygen and considered to have a range from the lowest part of the atmosphere to 40 km altitude. The neutral atmosphere is a non-dispersive medium with respect to radio waves up to 15 GHz of frequency, thus the propagation is GPS-frequency independent [16]. Even though the troposphere is the dominant contribution of the tropospheric delay, the stratosphere is also a constituent to this delay term. The current existent models of the troposphere such as Hopfield, Saastamoinen and UNB3, are fundamentally empirical and are used by commercial GNSS processing software.

This chapter neglects satellite configurations where the receiver is below the horizon, a scenario that is possible when using radio occultation techniques as described in Chapter 1. The consideration of bending GPS signals after reflecting at the ocean surface is beyond the simple geometric optics principles introduced in Chapter 4, and beyond the scope of this work.

The first part of this chapter describes the empirical Hopfield model for the troposphere. The mathematical expressions that retrieve the tropospheric delay are defined, and also the underlying assumptions.

The second section indicates the analytical method to follow when applying the tropospheric model and the necessary tools to find the tropospheric delay corresponding to the satellite mission of this project.

Finally, the inputs from the case study of this dissertation are introduced in order to obtain tangible results and evaluate the strengths and weaknesses of the derivation.

5.1 Hopfield Model

The tropospheric path delay Δ^{Trop} can be defined by integrating the refractive index n or the refractivity N^{Trop} along the geometric range s_0 [16]:

$$\Delta^{Trop} = \int (n-1)\, ds_0 = 10^{-6} \int N^{Trop}\, ds_0 \qquad (5.1)$$

Hopfield is an empirical model of the troposphere that separates the refractivity into a dry component N_d^{Trop} and a wet component N_w^{Trop}:

$$N^{Trop} = N_d^{Trop} + N_w^{Trop} \qquad (5.2)$$

The dry part results from the hydrostatic or dry atmosphere and it can be precisely determined by surface pressure measurements. On the other hand,

the wet part results from the water vapor on the atmosphere and it cannot be modeled precisely from surface measurements. This lack of precision is due to the fact that the water vapor has an irregular distribution in the troposphere. However, only about ten percent of the tropospheric refraction arises from the wet component while ninety percent is from the dry component. In practice, models for the dry and wet refractivity at the surface of the Earth, $N_{d,0}^{Trop}$ and $N_{w,0}^{Trop}$, are used:

$$N_{d,0}^{Trop} = c_1 \frac{p}{T} \qquad c_1 = 77.64\ K\ mb^{-1} \tag{5.3}$$

$$N_{w,0}^{Trop} = c_2 \frac{e}{T} + c_3 \frac{e}{T^2} \qquad c_2 = -12.96\ K\ mb^{-1} \qquad c_3 = 3.718 \cdot 10^5\ K^2\ mb^{-1} \tag{5.4}$$

Where,

p is the atmospheric pressure in millibar [mb]

T is the atmospheric temperature in kelvin [K]

e is the partial pressure of water vapor in millibar [mb]

c_n are empirical coefficients that describe the local situation

Due to the difficulty in modeling the wet portion, the Hopfield model assumes the same functional model for the dry and wet components of the tropospheric delay. The functional model considers the dry and wet refractivity as function of the height above the surface as shown in Figure 5.1. The wet

layer is accounted as the lowest part of the neutral atmosphere with an effective height h_w of 11 km approximately. The dry layer has an effective height h_d of around 40 km, which can be computed more precisely as function of temperature:

$$h_d = 40\,136 + 148.72\,(T - 273.16) \qquad [m] \tag{5.5}$$

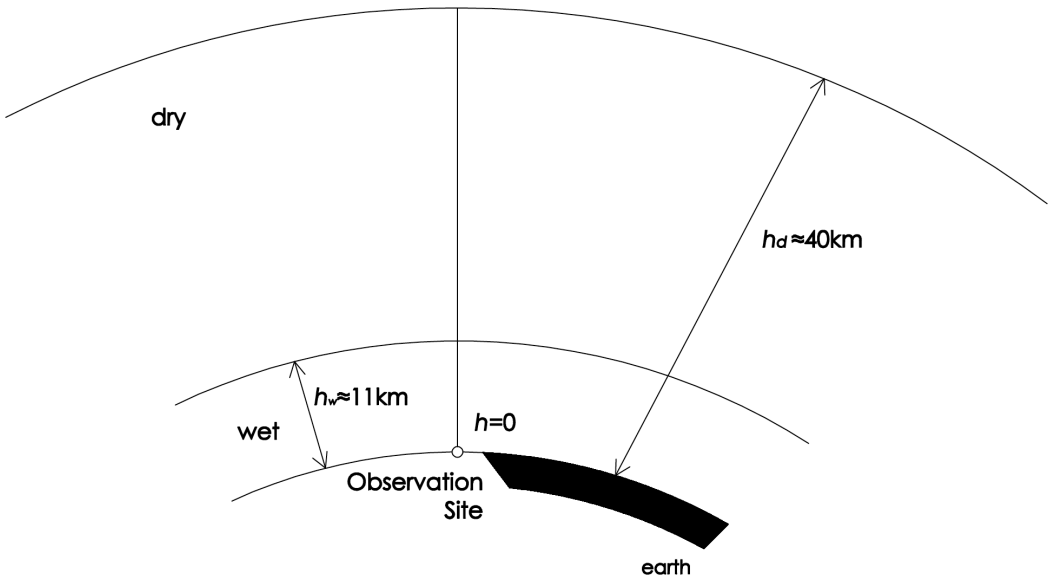

Figure 5.1. Thickness of Wet and Dry Layers as Defined in the Hopfield Model

The integral of the functional model for the dry and wet components has the respective limits of integration h_d and h_w shown in Figure 5.1. They can be solved if the delay is calculated along the vertical direction (at zenith of the observation site) and if the curvature of the signal path is neglected [16]. After the calculations, therefore, the total tropospheric zenith delay at the observation site yields

$$\Delta^{Trop,\ z} = \Delta_d^{Trop,\ z} + \Delta_w^{Trop,\ z} = \frac{10^{-6}}{5}\left[N_{d,0}^{Trop}\ h_d + N_{w,0}^{Trop}\ h_w\right] \tag{5.6}$$

This model, though, does not account for an arbitrary angle of the signal. When the satellite is not at zenith, a larger path length of the signal through the troposphere contributes a greater delay. Therefore, an obliquity factor is frequently applied which is the projection from the zenith onto the line of sight. The transition is implemented as the application of a mapping function, which is function of the elevation angle *E* at the observing site, in degrees [16]. Explicitly, the mapping functions for the Hopfield model are:

$$\begin{aligned} m_d(E) &= \frac{1}{sin\sqrt{E^2+6.25}} \\ m_w(E) &= \frac{1}{sin\sqrt{E^2+2.25}} \end{aligned} \tag{5.7}$$

By introducing the mapping function to equation (5.6), the total tropospheric delay at the observation site in units of meter is:

$$\Delta^{Trop} = \frac{10^{-6}}{5}\left[N_{d,0}^{Trop}\ h_d\ m_d(E) + N_{w,0}^{Trop}\ h_w\ m_w(E)\right] \tag{5.8}$$

where,

$N_{d,0}^{Trop}$ is the dry refractivity at the surface of the Earth

$N_{w,0}^{Trop}$ is the wet refractivity at the surface of the Earth

h_w is the effective height of the wet layer in meter [m]

h_d is the effective height of the dry layer in meter [m]

$m_d(E)$ is the mapping function for the dry component

$m_w(E)$ is the mapping function for the wet component

E is the elevation angle at the observing site in degrees [deg]

5.2 Tropospheric Delay Derivation

The tropospheric delay corresponding to the case study of this project can be found by applying equation (5.8) and solving for each of the terms.

Refractivity Terms – The dry and wet refractivity terms depend on atmospheric parameters at the observation site. Note that measured values of *p*, *T* and *e* are assumed to be available at the specular point. Alternatively, there are profile functions to express pressure, temperature and water vapor pressure as a function of height *H* above the mean sea level:

$$p = p_0\,(1 - 0.0226\,H)^{5.226}$$
$$T = T_0 - 6.5\,H \qquad (5.9)$$
$$e = e_0\,10^{(1+H/8)\,H/8}$$

where,

p_0 is the atmospheric pressure at sea level (1013.25 mb)

T_0 is the atmospheric temperature at sea level (291.2 K)

e_0 is the water vapor pressure at sea level (15 mb)

Recalling the case study introduced in Chapter 4, the atmospheric parameters at the specular point location can be computed by using the set of equations in (5.9). Since it is assumed that the specular point is always located on the WGS 84 ellipsoidal surface, the height H is set to zero. Consequently, the atmospheric parameters at the specular point correspond to the nominal values at sea level, p_0, T_0 and e_0.

Hence, the computation of the dry and wet refractivity terms at the surface of the Earth are performed as described in (5.3) and (5.4), which results in the following values shown in Table 5.1

Table 5.1. Dry and Wet Refractivity Values on the Surface for the Case Study

Refractivity	Value
$N_{d,0}^{Trop}$	270.1536
$N_{w,0}^{Trop}$	65.1009

The effective height of the wet component is fixed to a mean value [16] and the effective height of the dry layer is function of the temperature as expressed in (5.5). Table 5.2 shows the effective height values to be used in this case study:

Table 5.2. Wet and Dry Effective Heights for the Case Study

Effective Height	Value [m]
h_w	11,000
h_d	42,818.91

Now, it is possible to compute the total tropospheric zenith delay by plugging the results obtained in Tables 5.1 and Table 5.2 to equation (5.6).

Table 5.3. Total Tropospheric Zenith Delay at the Specular Point

Total Tropospheric Zenith Delay	Value [m]
$\Delta^{Trop,\,z}$	2.4568

The result shown in Table 5.3 corresponds to the accumulated tropospheric delay that a signal carries when it arrives at the specular point and it is emitted by a GPS satellite located at zenith of the observation site.

Mapping Function Terms – The mapping function in (5.7) represents an obliquity factor to be applied to the model when the signal arrives at an arbitrary angle different than at zenith. Not surprisingly, this obliquity factor is a function of the elevation angle *E* at which the signal arrives at the specular point. The Hopfield model assumes that the curvature of the signal path can be neglected, which means that the elevation of the GPS satellite corresponds to the elevation at which the signal arrives at the specular point.

Satellite Elevation. The elevation of a satellite with respect to an observation site can be defined by a transformation of coordinate frames from the ECEF to the East, North, Up (ENU) Local system at the specular point [26]. This local system allows the separation of the horizontal component from the vertical, which is helpful to determine whether a satellite is visible (above the horizon) or not to the observation site (Figure 5.2).

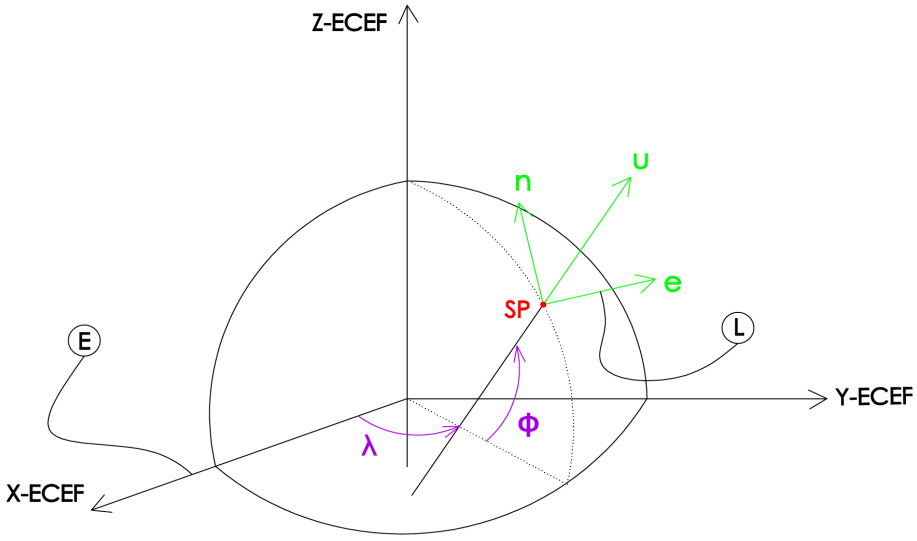

Figure 5.2. ECEF Coordinate Frame and ENU Local System

In the literature, there are already algorithms that contain the rotation matrix to rotate from the ECEF frame to the Local ENU, which is defined as follows:

$$ {}^{L}\boldsymbol{R}^{E} = \boldsymbol{R_1}(90-\phi)\,\boldsymbol{R_3}(\lambda-90) = \begin{bmatrix} -sin\lambda & cos\lambda & 0 \\ -sin\phi cos\lambda & -sin\phi sin\lambda & cos\phi \\ cos\phi cos\lambda & cos\phi sin\lambda & sin\phi \end{bmatrix} \qquad (5.10) $$

The geodetic longitude λ and latitude Φ to introduce are the ones corresponding to the location of the specular point found in Chapter 4.

The last step to complete the coordinate transformation is to perform the translation of the origin of the ECEF frame to the specular point location. For instance, consider the desire to find the elevation of the GPS satellite. The position of the GPS satellite needs to be expressed with respect to the specular point site $\Delta\mathbf{r}_G^{(L)}$ as represented in Figure 5.3:

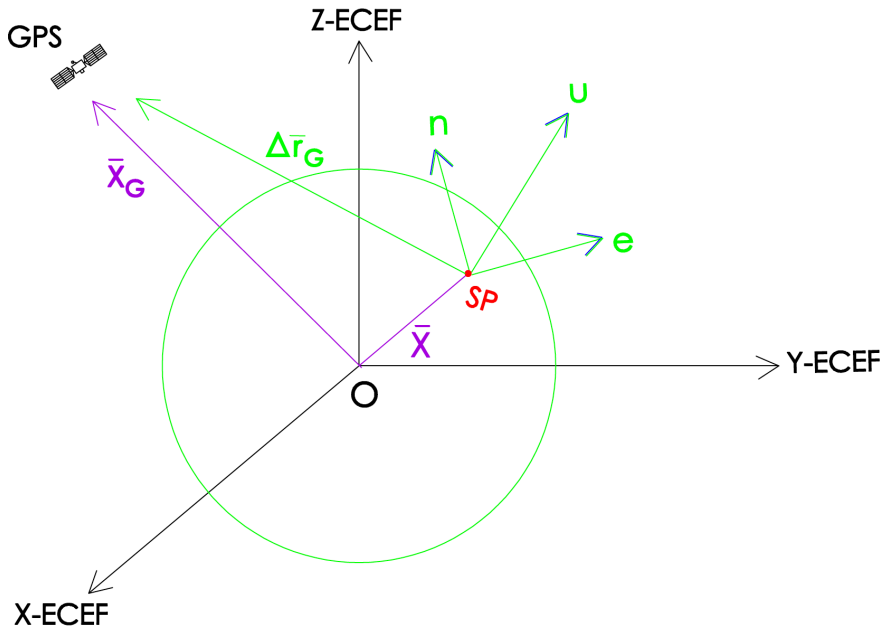

Figure 5.3. Transformation of the GPS Position Vector to the Local ENU System

The GPS position expressed in the local frame $\Delta \mathbf{r}_G^{(L)}$ can be computed as:

$$\Delta \mathbf{r}_G^{(L)} = {}^{L}\boldsymbol{R}^{E} \left(\boldsymbol{X}_G^{(E)} - \boldsymbol{X}^{(E)}\right) \tag{5.11}$$

By introducing the positions of the GPS satellite and the specular point from the case study in ECEF (Table 5.4),

Table 5.4. Position of the GPS Satellite and the Specular Point Location in the ECEF Frame and Geographic Coordinates

Position	X_{ECEF} [km]	Y_{ECEF} [km]	Z_{ECEF} [km]	Φ [deg]	λ [deg]
GPS PRN 1	-22,488.658	-13,987.206	-2,560.537	-	-
SPECULAR POINT	-3,847.534	-4,851.718	1,523.908	13.92	231.58

$\Delta \mathbf{r}_G^{(L)}$ results in (Table 5.5):

Table 5.5. Position of the GPS Satellite Expressed in the Local ENU System

Position	e [km]	n [km]	u [km]
GPS PRN 1	-8,929.437	-8,471.534	17,208.417

Thus, the elevation can be computed from the new position vector by trigonometry in Figure 5.4:

$$E = \sin^{-1}\left(\frac{u}{\sqrt{e^2+n^2+u^2}}\right) \tag{5.12}$$

Table 5.6. GPS Satellite Elevation Angle with respect to the Specular Point Site

Elevation	Value [deg]
E	54.425

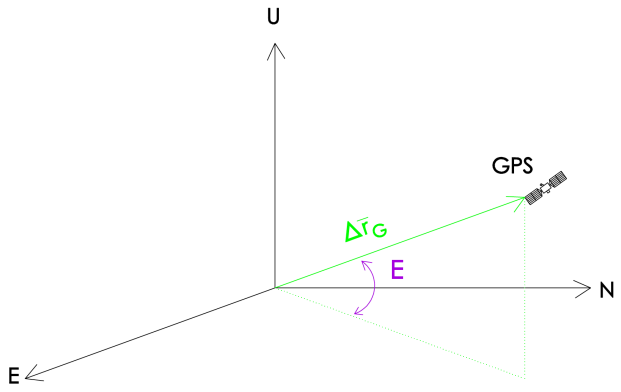

Figure 5.4. Elevation Angle in the ENU Frame

Notice that the elevation angle E is actually the complementary angle of the angle of incidence θ_i, which is 35.575 degrees computed in Chapter 4.

So now, by using (5.7) it is possible to get the obliquity factors (Table 5.7):

Table 5.7. Mapping Function Values Given the Elevation Angle

Mapping function	Value
m_d (E)	1.2286
m_w (E)	1.2292

Total Tropospheric Delay – Finally, all the necessary tools are ready to be applied to equation (5.8) in order to compute the total tropospheric delay (Table 5.8).

Table 5.8. Total Tropospheric Delay at the Specular Point

Total Tropospheric Delay	Value [m]
Δ^{Trop}	3.0184

As expected, this total tropospheric delay is larger than the zenith one by 22.86 %. Figure 5.5 shows how the total tropospheric delay varies with the elevation angle. The delay is maximum for satellites at the horizon and minimum for satellites at zenith.

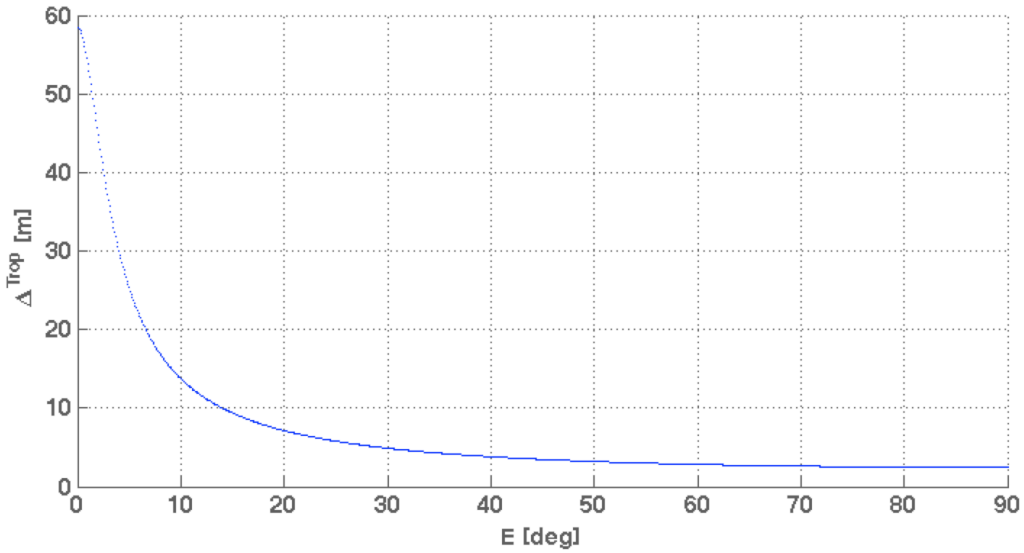

Figure 5.5. Tropospheric Delay versus Elevation Angle

The application of a mapping function is an error source to take into account. The uncertainties in modeling the wet and dry tropospheric delay are amplified at low elevation angles. The delay values start to increase considerably at elevation angles below 15 degrees. And below five degrees, even the best models produce errors of several decimeters. Therefore, the CYGNSS receivers should avoid tracking satellites at very low elevation angles, for which the reflected path may travel through a significant amount of troposphere.

5.3 Tropospheric Delay in the Measurement Model

Recall that the ionospheric measurement model obtained in Chapter 3 contains a tropospheric delay term related only to the reflected signal. This is due to the fact that the direct signal does not sweep any layer of the neutral

atmosphere, so it does not suffer any tropospheric refraction before reaching the CYGNSS satellite:

$$\rho_R - \rho_D = c\,(\Delta\tau_{rel}) = \Delta r + \Delta I + I_{below} + T_R + \Delta\varepsilon \tag{5.13}$$

On the other hand, the reflected signal does suffer a tropospheric delay on the two segment paths at which it can be split: on the incoming ray towards the specular point and on the outgoing ray leaving the specular point. For the case study, it is interesting to note that both segments of the reflected signal will accumulate the same tropospheric delay, since both the GPS and CYGNSS satellites are at the same elevation at the Specular Point. This is due to the Law of Reflection, which is described in Chapter 4. Hence, the total tropospheric delay corresponding to the reflected signal path is twice of the tropospheric delay represented in Table 5.9.

Table 5.9. Total Tropospheric Delay of the Reflected Signal for the Case Study

Total Tropospheric Delay	Value [m]
T_R	6.0369

In conclusion, Hopfield model is a straightforward estimation of the tropospheric refraction when the atmosphere is very dry and when the GPS satellites are not at low elevation angles. The dry component can be estimated with a precision of one percent, while the wet component may commonly have errors of 10-20%.

CHAPTER 6

IONOSPHERIC DELAY ANALYSIS

The last terms to investigate from the measurement model are the ionospheric delay components, to which the Total Electron Content (TEC) is proportional. In practice, once the CYGNSS mission is launched, TEC will be the measurement extracted from the DDM. In this chapter a simulation of typical ionospheric delay terms is performed using the case study, with the aim of quantifying measurements that will ultimately be made from CYGNSS.

As described previously in the GPS error section, the ionosphere can be considered the single largest error source for GNSS users. Therefore, it is expected in the case study that the ionospheric delay terms will be the highest errors on the true range of the signal path.

The first part of this chapter recalls the description of the ionospheric refraction and its dependency on the electron density. An obliquity function is also presented in order to take into account the geometric angle that the signal raypath slices through each ionospheric layer.

The second section shows the methodology for computing TEC along a raypath range. The ionospheric model used to get the electron densities is described, and the computational procedure is explained in detail.

Lastly, the ionospheric simulation is implemented for the case study by considering the corresponding assumptions on the two ionospheric delay terms ΔI and I_{below} in the measurement model.

6.1 Ionospheric Refraction

Ionospheric refraction of electromagnetic signals is induced by the ionized particles of the atmosphere. This ionized region, called the ionosphere, extends in various layers from about 50 to 2,000 km above the Earth as described in more detail in Chapter 1.

The ionosphere is a dispersive medium with respect to the GNSS radio signals, so the propagation is frequency dependent [16]. In addition, the refractive index depends on the electron density N_e, which is the number of electrons per cubic meter. There exist two different refractive indexes: the one corresponding to the carrier phase waves is the *phase refractive index* n_{ph} and the one corresponding to the code phase measurements is the *group refractive index* n_{gr}. Since CYGNSS satellites output DDMs using code phase measurements, the ionospheric refraction experienced by the signals can be written as:

$$\Delta_{gr}^{Iono} = \frac{40.3}{f^2} \int N_e \, ds_0 \tag{6.1}$$

Where,

Δ_{gr}^{Iono} is the ionospheric delay for the group refractive index [m]

f is the radio-frequency of the propagating signal in Hertz [Hz]

N_e is the number of electron per cubic meter [electrons/m^3]

s_0 is the geometric range along the straight signal path in meter [m]

Defining the Total Electron Content (TEC) as the total number of electrons along the straight signal path between the satellite and the receiver,

$$TEC = \int N_e \, ds_0 \tag{6.2}$$

and substituting to (6.1), results in:

$$\Delta_{gr}^{Iono} = \frac{40.3}{f^2} \, \mathrm{TEC} \tag{6.3}$$

The TEC is commonly expressed in TEC units (TECU), defined as

$$1 \, TECU = 10^{16} \, \mathrm{electrons} \, per \, m^2 \tag{6.4}$$

The simplest way to model the TEC is by computing the Vertical Total Electron Content (VTEC). This quantity denotes the total overhead electron content. However, it is only valid for satellites at zenith. For arbitrary geometric angles (Figure 6.1), computations need to take into account an obliquity factor that considers the variation of the signal path length with the zenith angle.

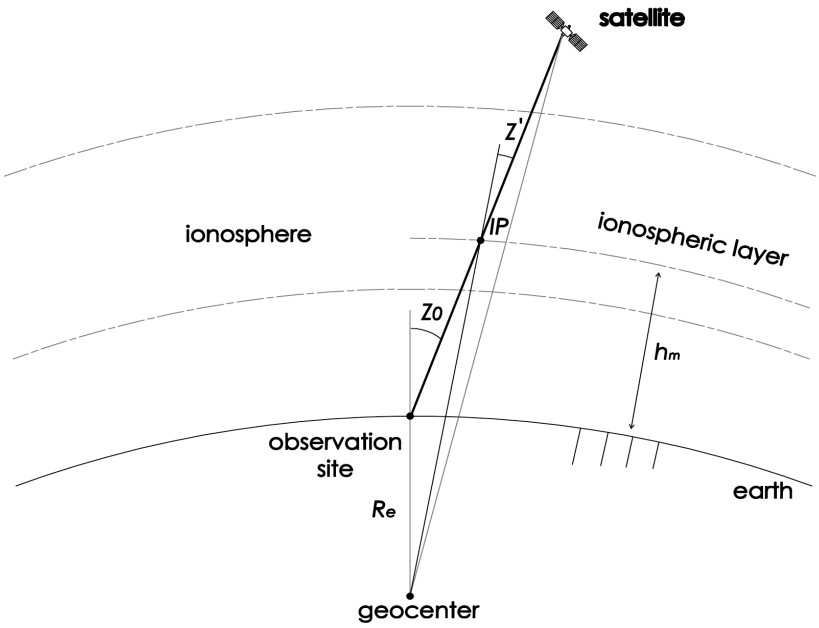

Figure 6.1. Geometry for the Ionospheric Path Delay

Figure 6.1 represents a single-layer model where all free electrons are concentrated in an infinitesimally thin spherical shell that contains the ionospheric point *IP* at the height h_m. By studying the geometry, a trigonometry relation can be derived:

$$\sin \mathrm{z}' = \frac{\mathrm{R}_e}{\mathrm{R}_e + h_m} \sin z_0 \tag{6.5}$$

Where,

z' is the zenith angle at the ionospheric point

z_0 is the zenith angle at the observing site

R_e is the mean radius of the Earth

h_m is the mean value for the height of the ionosphere

Hence, by applying the obliquity factor *OF* the ionospheric refraction for an arbitrary angle of the signal is:

$$\Delta_{gr}^{Iono} = OF \ \frac{40.3}{f^2}\mathrm{VTEC} = \frac{1}{\cos z'}\frac{40.3}{f^2}\ \mathrm{VTEC} \tag{6.6}$$

6.2 Simulation of Ionospheric Electron Content

The theoretical approach presented previously makes use of a single-layer model to compute the ionospheric refraction. The simplification of a single thin shell of ionosphere reduces the accuracy of the resultant ionospheric delay. In practice, therefore, a multi-layer model is used here.

Consider a GPS satellite at an arbitrary zenith angle transmitting electromagnetic signals to an observation site. The observation site is the end of a straight-line raypath, and may be either the specular point of the case study or the location of the CYGNSS receiver. The objective is to find the TEC along the straight signal path between the satellite and the observation site (Figure 6.2).

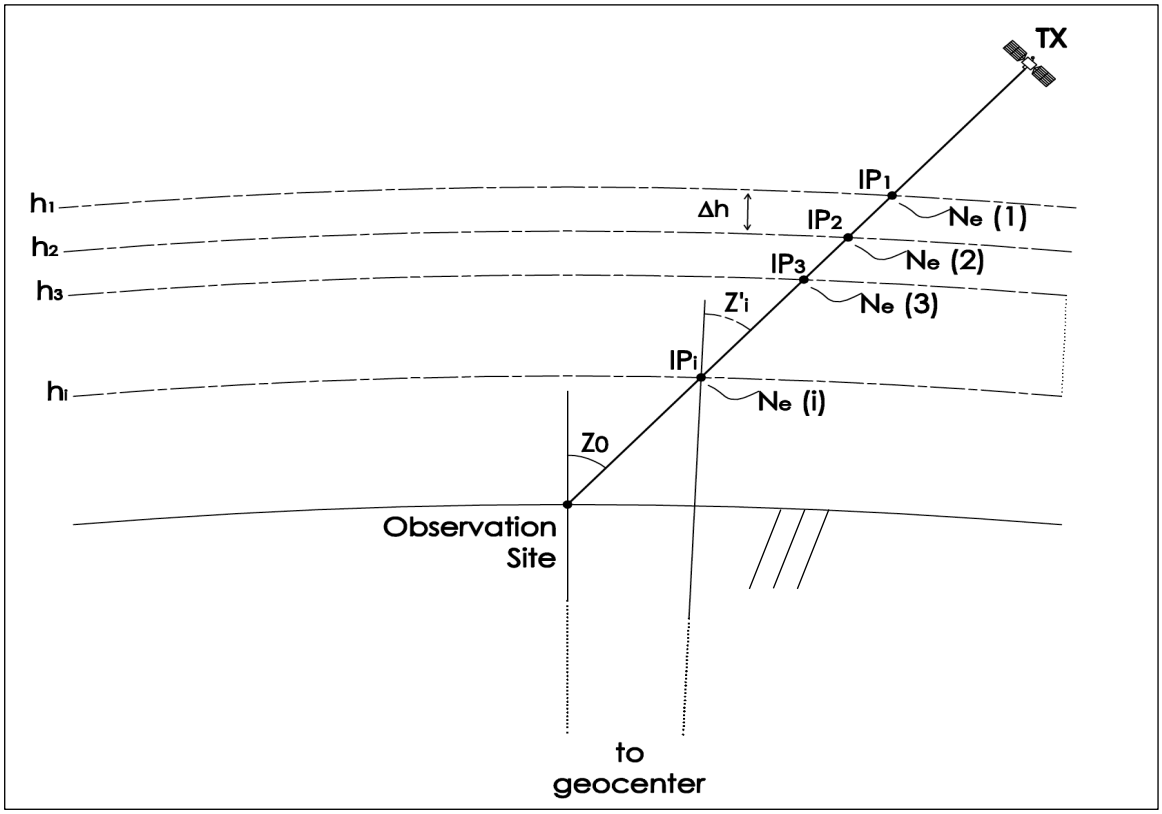

Figure 6.2. Discretization of the Straight Signal Path for Total Electron Content Computation

The method is to discretize the raypath into several ionospheric points IP_i at different heights h_i evenly spaced by Δh intervals. Each of these discrete points will have associated a particular electron density $N_e(i)$, from which the TEC_i corresponding to that interval is obtained. This TEC_i includes the electrons in a column with a cross section of one-meter square that extends from that discrete point to the next lower one. Therefore, the TEC along the signal raypath can be computed by doing the summation of each of the electron content of each interval.

So, the expression that estimates the total electron content along the raypath with an arbitrary angle is the following discrete form of the integral from (6.2) in TECU:

$$TEC = \sum_i \frac{N_e(\phi_i,\lambda_i,h_i)\,\Delta h\,OF(\phi_i,\lambda_i,h_i)}{10^{16}} \tag{6.7}$$

$N_e(\phi_i,\lambda_i,h_i)$ is the electron density at the i^{th} ionospheric point at geographic latitude ϕ_i, longitude λ_i, and height h_i. Δh is the difference in height between consecutive points, assumed to be evenly spaced. $OF(\phi_i,\lambda_i,h_i)$ is the obliquity factor for arbitrary raypath angle.

For a given height h_i the ionospheric point on the raypath at that height can be specified by its geographic latitude ϕ_i and longitude λ_i [6]. This specific location is input to an ionospheric model that gives as outputs the electron density $N_e(i)$ corresponding to that location.

The *International Reference Ionosphere* 2007 (IRI-2007) provides the electron density data and consists in an international project with the goal to produce an empirical standard model of the ionosphere based on all available data sources [2]. For a given location, time and date, IRI specifies monthly averages of the electron density, electron temperature, ion temperature, and ion composition in the altitude range from 50 to 2,000 km.

Then the electron density is multiplied by the interval value Δh so the user obtains the vertical total electron content inside a tube of length Δh. The

obliquity factor explained previously in Figure 6.1 is applied to each of the different discrete heights considering the respective apparent zenith angle at each point to compute the TEC along a slant, rather than vertical path, for the interval between points *i* and *i+1*. The slant total electron content along the raypath in a multi-layer model will consist of the sum of the total electron content at each discrete interval.

6.3 Ionospheric Delay in the Measurement Model

From the measurement model presented in Chapter 3, there are two remaining terms, the outputs ΔI and I_{below}:

$$\rho_R - \rho_D = c\,(\Delta\tau_{rel}) = \Delta r + \Delta I + I_{below} + T_R + \Delta\varepsilon \tag{6.8}$$

As described in the measurement model section, ΔI is the horizontal delay variation between the direct and reflected signal from the CYGNSS height above, while I_{below} corresponds to the total electron content that the reflected signal passes through below the CYGNSS altitude. Therefore, the simulation method explained in the previous section needs to be applied for four different signal paths as shown in Figure 6.3.

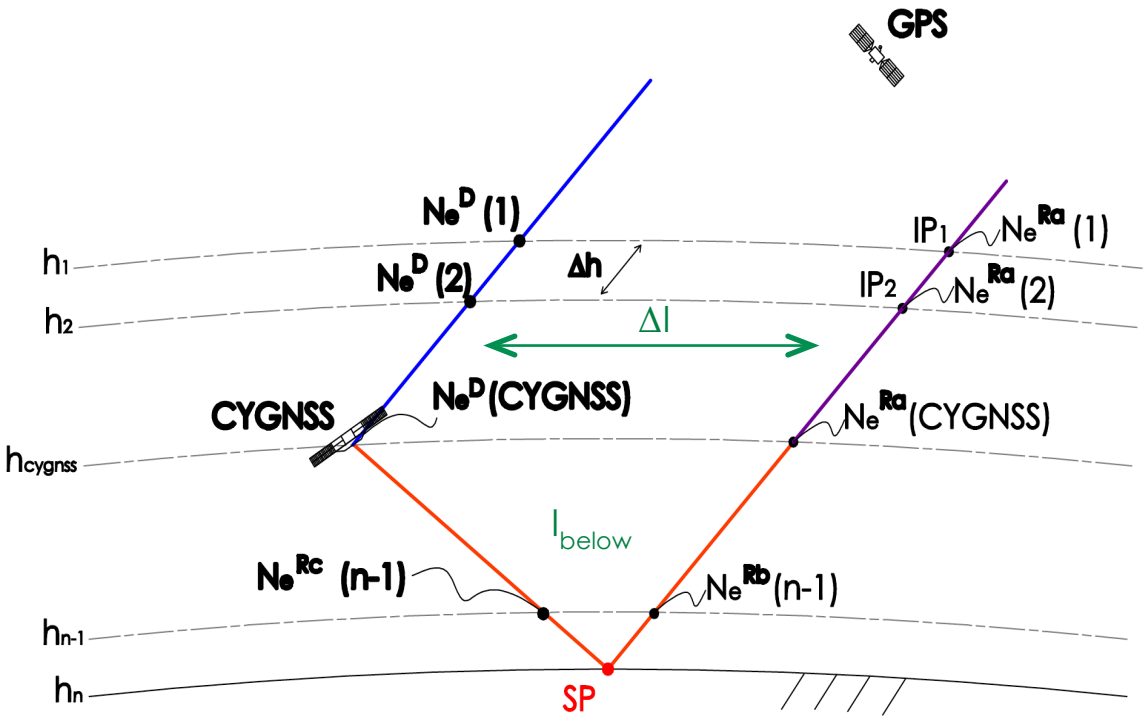

Figure 6.3. Discretization of the Direct and Reflected Signal Paths from the Case Study for TEC Computation

The direct signal path is in blue and the reflected signal can be split into three different parts: part *a* from the CYGNSS height and above in purple, and parts *b* and *c* as the incident and reflected raypaths below CYGNSS altitude in orange. Parts *b* and *c* generally encounter the densest layers of the ionosphere.

The first ionospheric point IP_1 is set to an upper limit of 2,000 km altitude. From that first point, 1900 more discrete heights complete the discretization of the signals at even intervals Δh of 1 km.

The discrete summation from (6.7) can be applied by running the algorithm explained in the method section together with the IRI model at the reference epoch of the case study (May 1st 2013 at 18:12:00.00 UTC). However, the IRI-2012 source code was not available at the time of writing this dissertation. For this reason, the reference epoch input to the IRI model has been set back by one solar cycle (eleven years) to simulate similar solar cycle conditions. Thus, Figure 6.4 illustrates the geographic coordinates of the specular point together with the CYGNSS satellite and the ionospheric point at CYGNSS height in order to identify the total electron content corresponding to each of the signal paths:

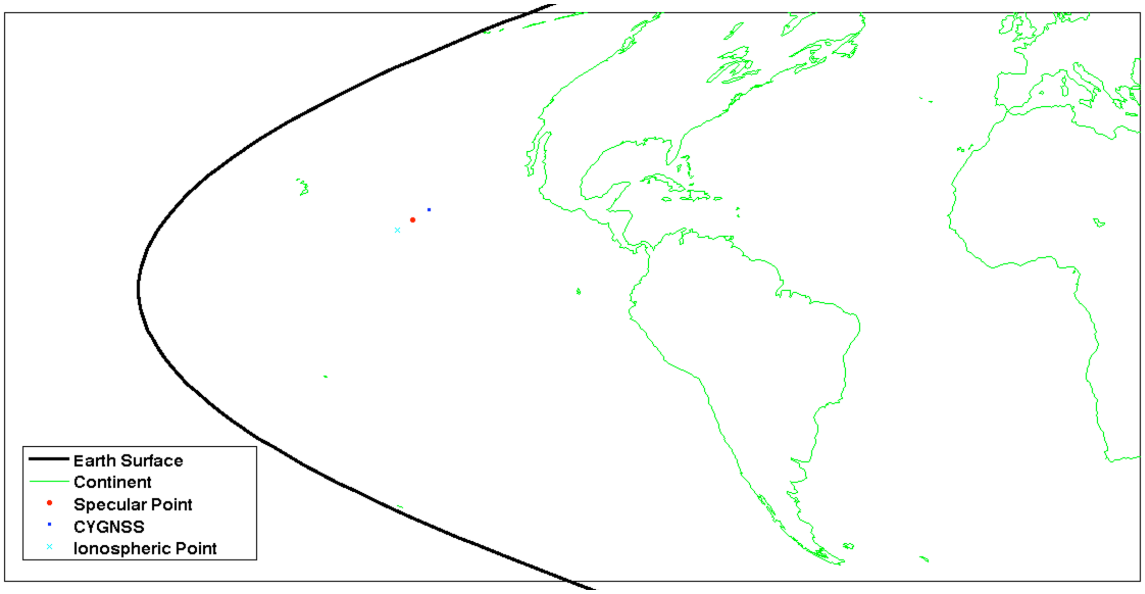

Figure 6.4. Distribution of the Specular Point, the CYGNSS Satellite and the Ionospheric Point in Geographic Coordinates for the Case Study

Table 6.1. Total Electron Content for Each Signal Path of the Case Study

TEC	Value [TECU]
TEC (r_D)	18.4502
TEC (r_{Ra})	18.0427
TEC (r_{Rb})	52.5940
TEC (r_{Rc})	51.5797

Referring back to the ionospheric delay terms on the measurement model, the TEC corresponding to the horizontal delay variation ΔI_{TEC} is computed as,

$$\Delta I_{TEC} = r_{Ra\,TEC} - r_{D\,TEC} \tag{6.9}$$

And the total electron content that the reflected signal sweeps below the CYGNSS height I_{below_TEC} is defined by,

$$I_{below\_TEC} = r_{Rb\,TEC} + r_{Rc\,TEC} \tag{6.10}$$

Table 6.2. Total Electron Content of the Ionospheric Delay Terms

TEC	Value [TECU]
ΔI_{TEC}	-0.4075
I_{below_TEC}	104.1736

ΔI_{TEC} does not seem to be a significant component. Its value is negative because the direct signal path encounters slightly more electron content than the reflected above the CYGNSS height. Hence, the ionospheric delay terms, ΔI and I_{below}, are simulated by applying equation (6.3).

Table 6.3. Ionospheric Delay Terms Results for the Case Study

Ionospheric Delay	Value [m]
ΔI	-0.0662
I_{below}	16.9149
I_{TOTAL}	16.8488

Note that for this case study where the satellites are at E=54.42 degrees of elevation, the ionospheric refraction contributes a larger error source than the tropospheric delay to the measurement model. Also, the ionospheric delay due to ΔI is a much smaller than I_{below} and, for this case, can be considered a negligible error source.

6.3.1 Assumptions on ΔI. In practice, ΔI may be considered insignificant for many cases if the ionosphere is smoothly varying (and not stormy). When the GPS and CYGNSS satellites are positioned at very high elevations with respect to the specular point site, the raypath of the direct and reflected signals above the CYGNSS height travel through almost the same spatial regions, so both signals see approximately the same total electron content.

An example of the ΔI magnitude for a geometric configuration in which satellites are positioned at very high elevation, corresponding to Case I from Section 4.3.1 illustrated in Figure 4.12, is shown. For an angle of E' = 86.65 degrees:

Table 6.4. Satellite and Specular Point Positions in the ECEF Frame for a High Elevation Configuration (E' = 86.65 degrees)

Element	X_{ECEF} [km]	Y_{ECEF} [km]	Z_{ECEF} [km]	Φ [deg]	λ [deg]
GPS PRN 1	-22,662.740	-12,912.852	-855.471	-	-
CYGNSS – 1	-6,098.937	-3,153.911	-405.687	-	-
SPECULAR POINT	-5,645.790	-2,945.221	-361.226	-3.27	207.55

Table 6.5. Ionospheric Delay Values for a High Elevation Configuration

Ionospheric Delay	Value [m]
ΔI'	0.0108
I'_{below}	17.8323

The horizontal delay variation $\Delta I'$ has become less significant compared to the case study. I'_{below} is the main constituent of the computed TEC since the signal traverses the densest regions of the ionosphere. These regions are easily localizable in space, particularly overhead of the specular point site. Figure 6.5 shows this region by plotting the location of the specular point, the CYGNSS satellite and the ionospheric point at the CYGNSS height:

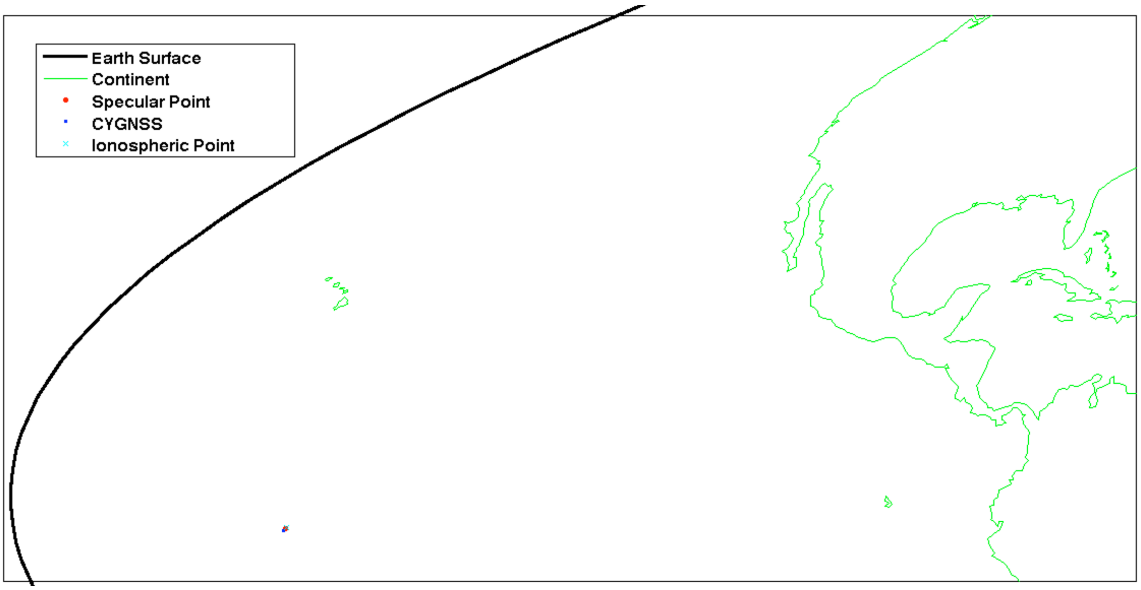

Figure 6.5. Distribution of the Specular Point, the CYGNSS Satellite and the Ionospheric Point in Geographic Coordinates for a High Elevation Configuration

On the other hand, a geometric configuration such as Case III from Section 4.3.1 illustrated in Figure 4.14 indicates the satellites are at low elevation with respect to the specular point. For an angle of E'' = 6.72 degrees,

Table 6.6. Satellite and Specular Point Positions in the ECEF Frame for a Low Elevation Configuration (E'' = 6.72 degrees)

Element	X_{ECEF} [km]	Y_{ECEF} [km]	Z_{ECEF} [km]	Φ [deg]	λ [deg]
GPS PRN 1	-12,789.849	-13,510.654	-19,002.839	-	-
CYGNSS – 1	-929.072	-5,596.629	3,888.873	-	-
SPECULAR POINT	-1,673.434	-5,783.586	2,097.792	19.33	253.86

Table 6.7. Ionospheric Delay Values for a Low Elevation Configuration

Ionospheric Delay	Value [m]
$\Delta I''$	0.4153
I''_{below}	43.1127

The horizontal delay variation $\Delta I''$ is larger, and in this case the same order of magnitude as other error sources such as multipath and receiver noise. This is due to the fact that the raypaths of the direct and reflected signals above the CYGNSS height travel through quite different regions of space. Therefore, $\Delta I''$ needs to be taken into account in the measurement model for satellites at low elevation, while $\Delta I''$ is negligible for high and mid elevation scenarios, assuming that the ionosphere is smoothly varying (as the IRI model is).

In addition, the delay component value I''_{below} has increased by more than 50%. When the CYGNSS satellite is at low elevation, the path length of the signal increases and it travels at a slant through more of the ionosphere. Furthermore, satellites at low elevation may have significantly different TEC contributions to I''_{below} from the incident and the reflected raypaths. At low elevation, i.e., high angles of incidence and reflection at the specular point, points on these raypaths are distant from each other. Figure 6.6 shows this division by plotting the location of the specular point, the CYGNSS satellite and the ionospheric point at the CYGNSS height:

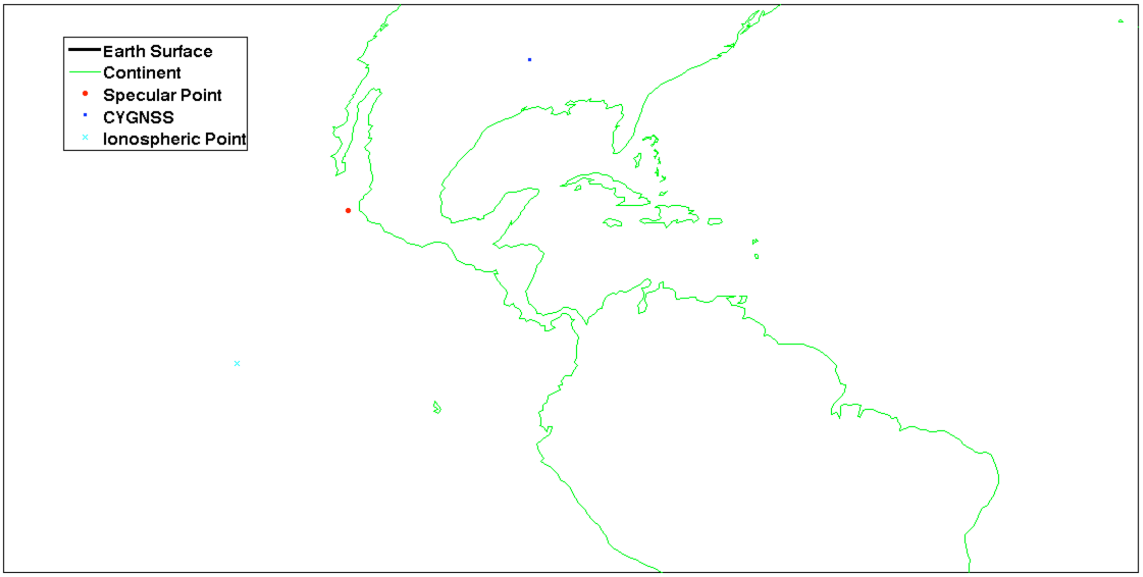

Figure 6.6. Distribution of the Specular Point, the CYGNSS Satellite and the Ionospheric Point in Geographic Coordinates for a Low Elevation Configuration

CHAPTER 7

MEASUREMENT MODEL SIMULATION

The last chapter estimates each of the measurement model terms for multiple simulated locations, to quantify the relative contributions of each to CYGNSS measurements. This estimation allows a study of the expected results when applying the formulated mathematical model.

Each of the model terms is computed as performed for the case study from Chapters 4 through 6, but for different samples of signals over a period of time. In order to do that, a design of the simulation for the deterministic terms is carried out consisting in several computational steps: location of specular points over time, discarding of specular points on land, calculation of the extra geometric ranges Δr, estimation of the tropospheric delays T_R, and finally, estimate of the ionospheric delay terms ΔI and I_{below}.

Finally, an analysis of the simulation evidences that the obtained results depend on two main factors: the satellite elevation angle and the local time due to solar radiation.

7.1 Case Study Terms

All the deterministic terms of the measurement model for the case study have been predicted from Chapters 4 through 6. Table 7.1 shows each of the parameter values for a configuration of satellites that has an elevation angle of 54.42 degrees at 9:12:00 local-time at the specular point:

Table 7.1. Each of the Measurement Model Parameters from the Case Study

Measurement Model Parameter	Value [m]
Δr	793,405
T_R	6.0396
ΔI	-0.0592
I_{below}	16.9156

Effectively, the simulation obtains analogous results shown in Table 7.1 extended for a sample of signals over a period of time.

7.2 Simulation Conditions and Results

The CYGNSS measurements are simulated for one set of GPS-CYGNSS satellites starting at 18:12:00 and ending at 23:08:00 UTC with time steps of one minute. The total time interval corresponds to around three orbital periods of the CYGNSS satellite (P = 1h 34min 37sec). In this time interval, one pair of GPS-CYGNSS satellites make measurements across the globe, spanning both the

dayside and the nighttime sides of the Earth. This is important for the study since the free electrons of the ionosphere are created by solar radiation.

From introducing the GPS and CYGNSS satellite positions at each instant of time, the specular point sites over the oceans are generated as represented in Figure 7.1:

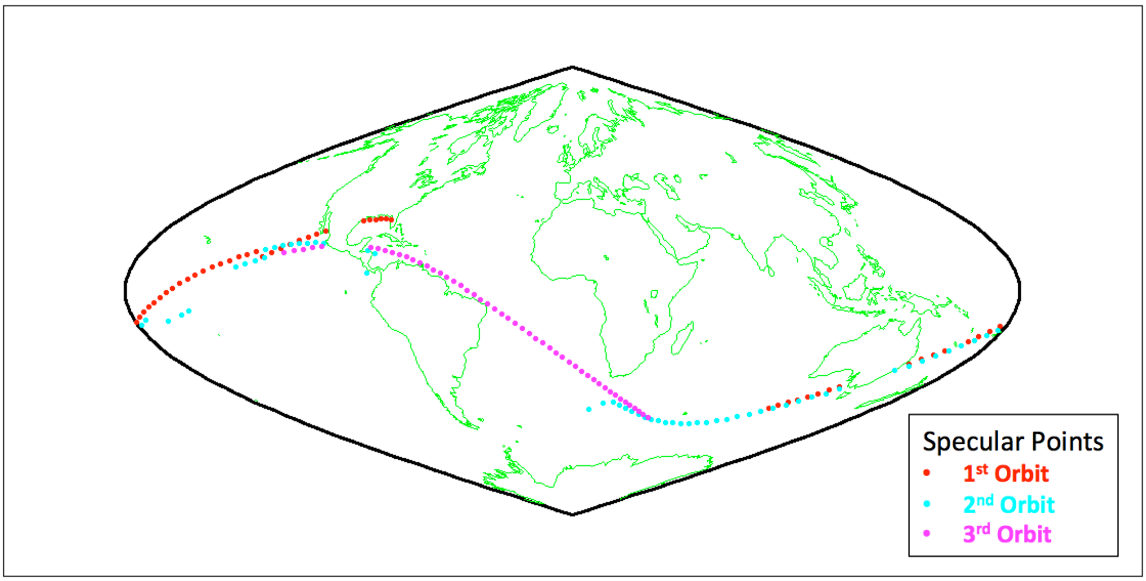

Figure 7.1. Location of Specular Points Generated in the Simulation for about Three Orbital Periods of CYGNSS with Time Steps of One Minute

Two different conditions are necessary for specular reflection to occur. On one hand, specular reflection occurs on water, so the points over land are discarded since CYGNSS would not receive any reflected signals. In addition, the specular reflection on the ocean is only possible when both the GPS and CYGNSS satellites are above the horizon with respect to each other, so they can “see” each other by direct line-of-sight.

Note that even though the CYGNSS orbital plane is inclined at 35 degrees, which makes its ground tracks to cover only mid-latitudes of the Earth, the specular points can reach high latitudes because GPS orbits have higher inclination, which are at 55 degrees.

Figure 7.2 shows the 3-D representation of one part of the simulation. The specular points over time are plotted in red, and the GPS and CYGNSS satellite locations in white and yellow respectively. The blue rays striking the specular points are the reflected signals while the white lines correspond to the direct raypaths.

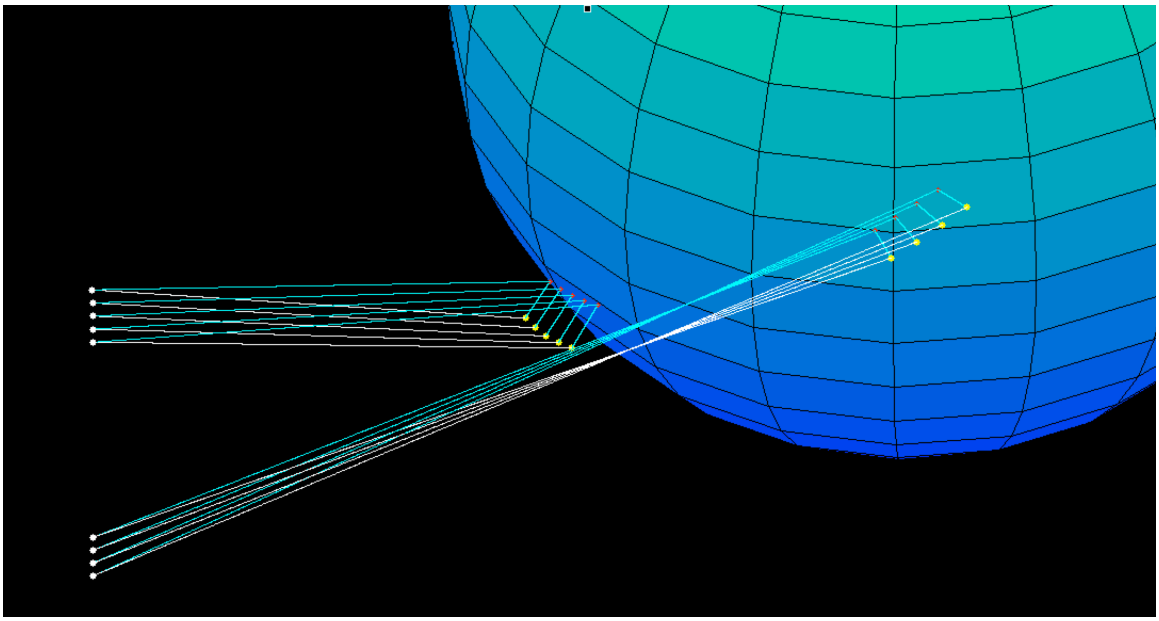

Figure 7.2. 3-D Simulation of Specular Points on the WGS 84 Ellipsoid and the Respective Direct and Reflected GPS Signals

Finally, the CYGNSS measurements from the simulation are obtained. The ionospheric discretization is set with height intervals of Δh = 50km. Each of the measurement model terms is displayed in Table 7.2 within time steps of three

minutes between the first and the second measurements and fifteen minutes after the second measurement.

Table 7.2. Measurement Model Parameters from the Simulation over Time

Time (UTC)	Δr [m]	T_R [m]	ΔI [m]	I_{below} [m]	E [deg]	Local Time at the SP
18:12:00	793,405	6.04	-0.06	18.87	54.43	9:12:00
18:15:00	636,969	7.30	-0.22	21.80	42.25	9:15:00
18:30:00	-	-	-	-	-	-
18:45:00	-	-	-	-	-	-
19:00:00	-	-	-	-	-	-
19:15:00	23,579	55.75	0.02	4.08	4.42	3:15:00
19:30:00	-	-	-	-	-	-
19:45:00	417,224	10.25	-0.85	30.28	28.53	8:45:00
20:00:00	49,621	39.44	0.05	47.98	6.72	12:00:00
20:15:00	-	-	-	-	-	-
20:30:00	-	-	-	-	-	-
20:45:00	13,338	69.25	0.05	2.72	3.25	23:45:00
21:00:00	23,020	56.22	0.06	6.01	4.38	5:00:00
21:15:00	105	116.23	-0.02	59.50	0.27	9:15:00
21:30:00	909	110.55	-0.06	46.38	0.81	12:30:00
21:45:00	117,520	24.46	-0.26	36.72	11.32	15:45:00
22:00:00	363,903	11.37	-0.64	26.86	25.49	19:00:00
22:15:00	223,162	16.25	0.02	1.71	17.43	22:15:00
22:30:00	-	-	-	-	-	-

The gaps represent a lack of coverage for reflected signals, caused by either the satellites being below the horizon with respect to each other or the reflected signals striking continental parts of the Earth rather than water.

An analysis of the results shows that two main factors influence the relative magnitude of each component of the measurement model.

Elevation Angle – The first factor is the elevation angle at which the satellites are located with respect to the specular point. The values from 18:12:00 UTC correspond to high elevation and result in higher extra geometric ranges, lower tropospheric delays, negligible ionospheric horizontal variations and medium values for I_{below}. On the other hand, the values from 19:45:00 UTC correspond to low elevation and result in lower extra geometric ranges, higher tropospheric delays, significant ionospheric horizontal variations and very high contributions on I_{below}.

Local Time – The amount of solar radiation is an important factor that explains the reason why in some cases I_{below} presents small contributions even for low elevation angles such as the values from 19:15:00 UTC. This is caused by the low amount of solar radiation represented in the respective local time, which means that the region is at nighttime or at dawn/dusk times.

CHAPTER 8

CONCLUSIONS AND FURTHER STUDIES

8.1 Overview

The main goal of this dissertation was to investigate the opportunity to measure electron content of the ionosphere over the oceans with CYGNSS satellites.

A pre-launch simulation of typical signal errors from the formulated measurement model has been performed to address this study. The simulation of CYGNSS measurements suggested that the obtained electron content parameters from the measurement model depend on two main factors: the satellite elevation angle and the local time or solar radiation. High elevation satellites are the most desirable configuration since it makes it easy to localize the retrieved TEC. In addition, the signal is not as much disturbed and does not carry as many errors as low satellite configurations do due to the application of mapping functions and/or obliquity factors.

The outcome of the research serves two purposes. First, the method for simulating ionospheric delays can be used in the near term in mission planning to provide typical ionospheric errors for simulated measurements. Second, and more importantly, this research proved the ability to estimate the delay induced by ionospheric refraction, by subtracting the true range and tropospheric errors from the measurements provided by CYGNSS. These estimates of ionospheric

delay obtained from measurements can be fed into data assimilation. The ingestion of more data will improve the accuracy of empirical models and ionospheric tomography. Ultimately, being able to obtain ionospheric measurements without having to build and launch new infrastructure implies great advantages in terms of economical opportunities for high quality science.

8.2 Summary of Contributions

Stating the most relevant concepts to keep in mind from the chapters, each of the contributions made in this dissertation is as follows:

8.2.1 Development of a Measurement Model. An analytical expression was formulated to estimate TEC from the ionosphere over the oceans by using CYGNSS satellite measurements. It has been necessary to use ranging measurements from direct and ocean-reflected GPS signals. The measurement model takes the *Delay Doppler Maps* (DDMs) as the inputs and retrieves the relative ionospheric delay terms as the outputs.

8.2.2 Analysis of Satellite and Raypath Geometries. The extra geometric range in the measurement model was computed by identifying the specular point location, the point on the ocean surface at which the reflected signal strikes. Analytical approaches to compute the specular point were presented. The

obtained location was evaluated to ensure the agreement with fundamental physical principles.

8.2.3 Quantification of the Signal Delay due to the Atmosphere. The tropospheric delay was described based on the Hopfield model, while the ionospheric delay terms were estimated by applying a multi-layer discretization model and taking typical electron densities from the *International Reference Ionosphere* (IRI).

8.2.4 Design of a Simulation. A pre-launch simulation of typical signal errors was studied by simulating the deterministic terms of the measurement model. A simulation of satellite locations was run over a period of time that included different elevation configurations of satellites encompassing both the daylight and nighttime sides of the Earth.

8.3 Further studies

The capability presented of extracting ionospheric electron content over the oceans with CYGNSS can be used to implement the measurements into data assimilation and empirical models. Applying the recommendations for future work listed below will contribute to the improvement of ionospheric models in retrieving more continuous and accurate results globally.

8.3.1 Study of the Impacts and the Implementation of CYGNSS Measurements into Data Assimilation and Empirical Models.

The obtained ionospheric parameters from the measurement model are relative to the ionospheric delay on the direct path, so they can make the most effective contribution when implemented into data-assimilative models and ionospheric tomography. In addition, the implementation should be followed by an investigation of whether or not the ionospheric models are improved over the oceans.

8.3.2Investigation of the Impact of Using Steady Sea Surface Models.

The assumption of always locating the specular point on the WGS 84 ellipsoid omits the ocean motion and geophysical phenomena such as tides, tsunamis and ocean swells. This contributes to errors on the geometric raypath range on the measurement model. An investigation to determine whether or not the impact is relevant should be performed. If so, a model of the sea surface motion should be considered.

8.3.3 Solving for the Specular Point Location Applying the Analytical Approaches presented in Chapter 4.

The optimization problem and the vector approach presented in section 4.2.2 should be analytically solvable given the assumptions. Therefore, finding the exact solutions and checking that the

satellites are above the horizon with respect to the specular point site are interesting tasks to take into account.

8.3.4 Further Atmospheric Model Refinement for Computing Tropospheric Refraction.

When estimating the tropospheric delay, atmospheric parameters such as temperature, pressure and water vapor pressure have been considered steady with geographic coordinates and season of the year, making height the only dependent variable. For this reason, it is important to regard taking atmospheric parameters from dynamical atmospheric models. In addition, the implementation of a mapping function is an important source of error especially for satellites at low elevation. The application of a multi-layer model is recommended for improved accuracy.

8.3.5 Study of the Minimum Satellite Elevation Angle for Neglecting the Horizontal Ionospheric Delay Variation and the Impact of Ignoring Ionospheric Storms.

The horizontal variation component ΔI of the ionospheric delay can be ignored when the direct and reflected signal sweep the same space regions above the CYGNSS satellite height. This occurs when the satellites are at high elevation with respect to the specular point site. A study of the minimum elevation angle for neglecting ΔI is an important contribution to consider. It is also relevant to note that the model used for the ionosphere, IRI, is a

climatological (i.e., average) model, which does not consider ionospheric storms or daily variability.

8.3.6 Extension to account for Bending GPS signals. All geometries in this study assumed straight line raypath propagation and neglected bending. Relaxing this assumption may improve the accuracy of ionospheric estimates made from CYGNSS measurements. Further beyond the scope of this study, there may exist the possibility to work with reflected signals with occulting satellite receivers. The study of this possible scenario involving radio occultation techniques is just a challenging suggestion for adventurer scientists.

APPENDIX A

ERROR VARIATION ANALYSIS FOR POSITIONING

The analysis consists in a simulation of GPS PRN 1 satellite positions computed in Matlab and STK. The following graphs represent simulations starting at the almanac reference epoch (May 1st 2013 16:44:48 UTC) running over 24 hours with time steps of one minute.

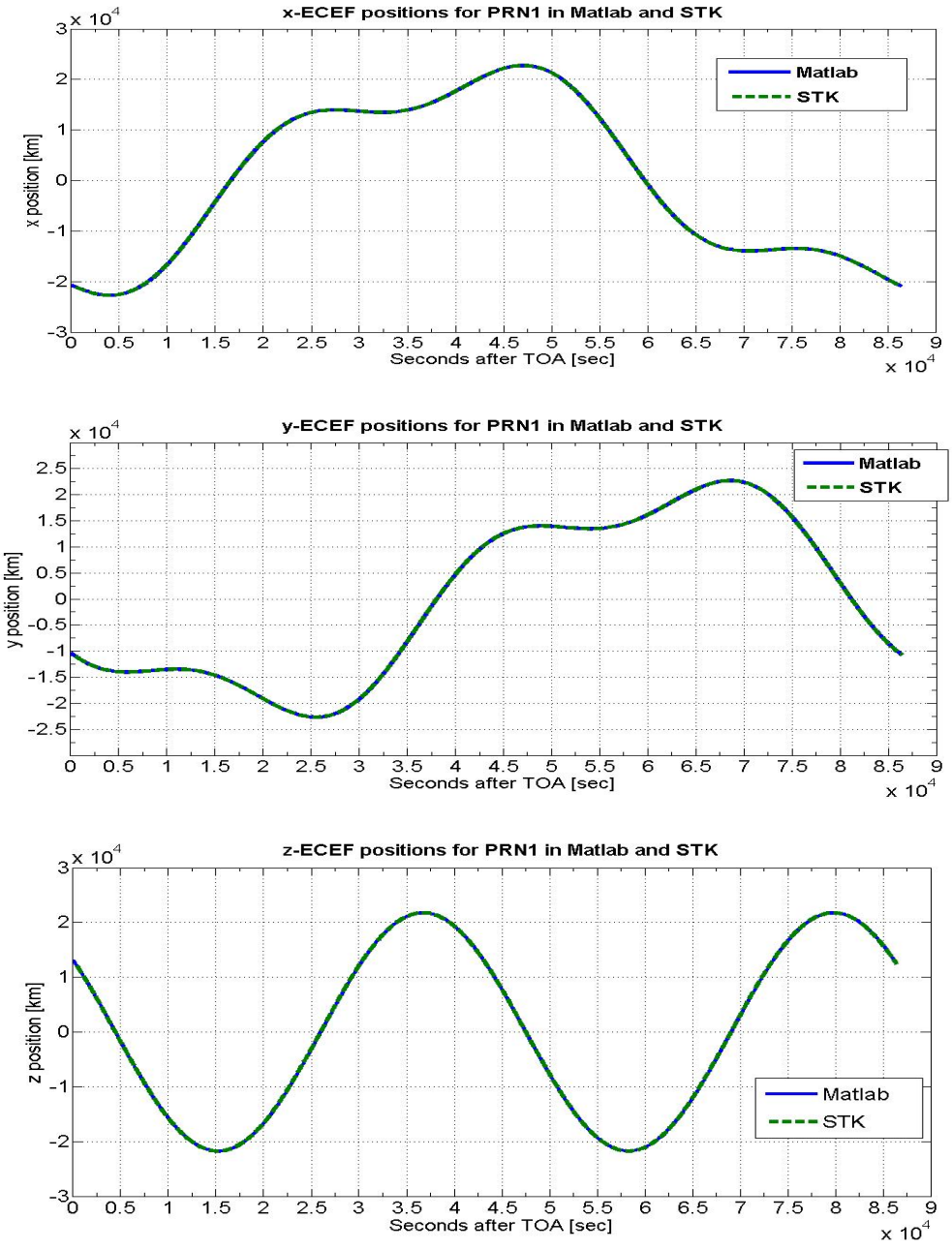

Figure A.1. Components of PRN 1 Positions over Time from Matlab and STK

Both curves overlap each other, so position discrepancies are visible by plotting the difference between the STK and Matlab results.

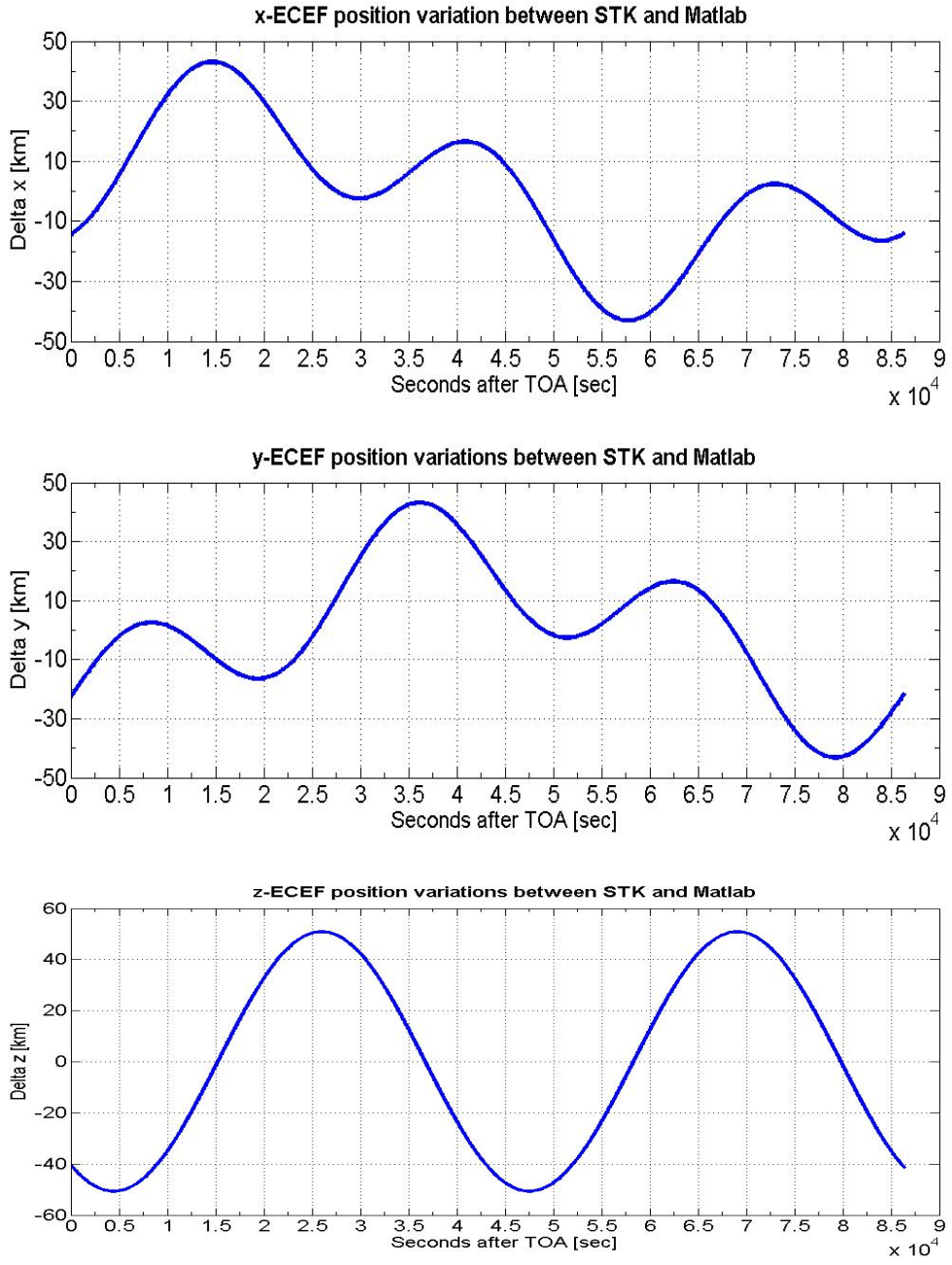

Figure A.2. Variation Components between STK and Matlab PRN 1 Positions

The graphs above show the presence of error variations between satellite positions computed in STK and positions computed in Matlab. Notice that the variations in each component do not go beyond 55 km. Also, see that when one of the three components has a relatively high error variation, the other two components have a very low value. The periodic behavior on the Z-component may be due to a possible error source on the inclination as shown in Figure A.3:

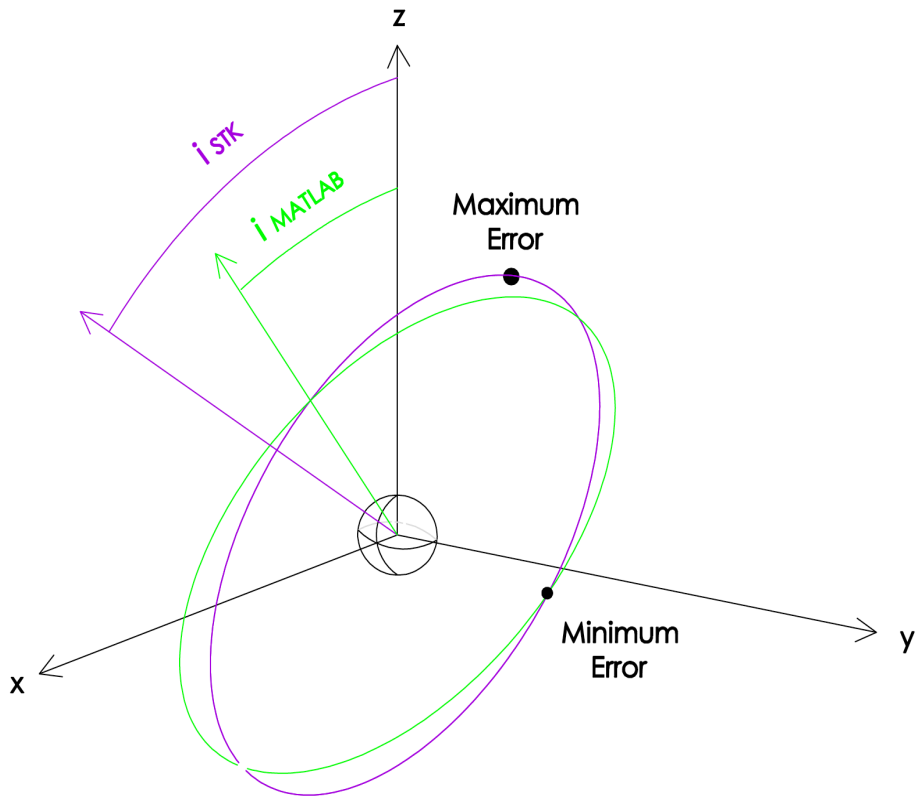

Figure A.3. Inclination Error Source on the Z-Component of the Position

Finally, the total error variation is computed as the norm of each error component. Hence, the maximum total error variation can be estimated:

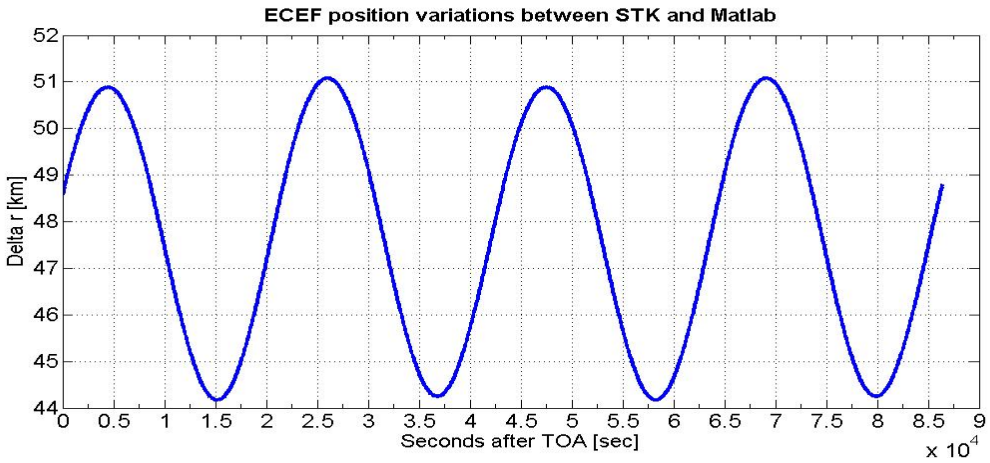

Figure A.4. Total Error Variation between STK and Matlab PRN 1 Positions

And a comparison of the total relative error variation to the STK yields to the graph represented in Figure A.5:

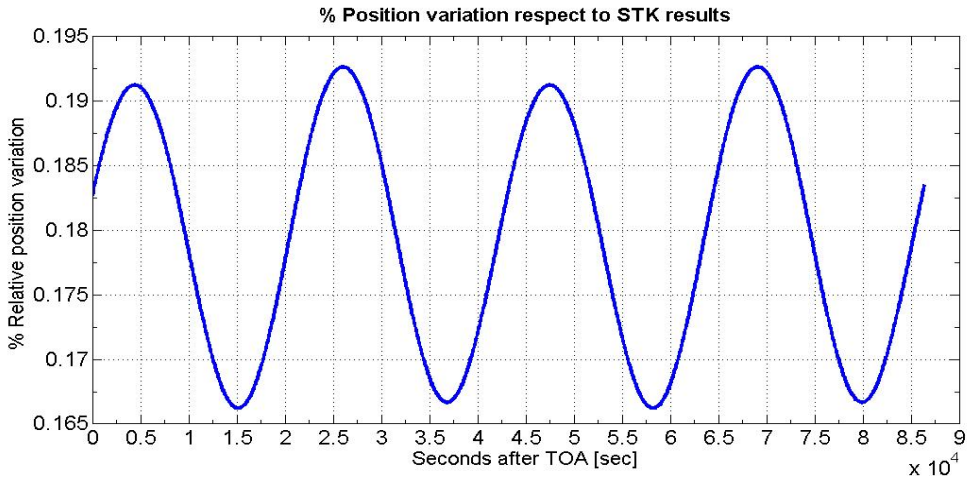

Figure A.5. Relative Error Variation with respect to STK Results

The Matlab and STK position values differ according to a total error variation that goes from 44 to 51 km, which can be translated to 0.167% to 0.193% of relative error variation with respect to STK solutions. In conclusion, it

is believed that the variation in magnitude is small enough to consider the position errors insignificant in terms of ray tracing analysis. Consequently, for subsequent simulations, the variations due to the STK propagation of almanac orbital parameters over time are considered negligible effects in terms of ray-path calculations.

BIBLIOGRAPHY

[1] Anderson, D., and T. Fuller-Rowell. *The Ionosphere*. Boulder, CO (325 Broadway, Boulder 80303-3326): Space Environment Center, 1999. Print.

[2] Bilitza, D., and B. W. Reinisch. "International Reference Ionosphere 2007: Improvements and New Parameters." *Advances in Space Research* 42.4 (2008): 599-609. Print.

[3] Bust, G. S., and C. N. Mitchell. "History, Current State, and Future Directions of Ionospheric Imaging." *Reviews of Geophysics* 46.1 (2008): 1-23. Print.

[4] Clarizia, M. P., C. P. Gommenginger, S. T. Gleason, M. A. Srokosz, C. Galdi, and M. Di Bisceglie. "Analysis of GNSS-R Delay-Doppler Maps from the UK-DMC Satellite over the Ocean."*Geophysical Research Letters* 36.2 (2009): 1-4. Web.

[5] *Cyclone Global Navigation Satellite System (CYGNSS)*. University of Michigan, n.d. Web. 15 May 2013. <http://aossresearch.engin.umich.edu/>.

[6] Datta-Barua, S. “Ionospheric Threats to the Integrity of Airborne GPS Users.” Diss. Stanford University, 2008. (2004): 28-32. Print.

[7] Datta-Barua, S. “Spacecraft Dynamics.” Illinois Institute of Technology. Engineering 1 Building, Chicago, IL. 13 Sep. 2012. Lecture.

[8] Elfouhaily, T., D. R. Thompson, and L. Linstrom. "Delay-Doppler Analysis of Bistatically Reflected Signals from the Ocean Surface: Theory and Application. "*IEEE Transactions on Geoscience and Remote Sensing* 40.3 (2002): 560-73. Print.

[9] Feynman, R. P., R. B. Leighton, M. Sands, and S. B. Treiman. "The Feynman Lectures on Physics." *Physics Today* 17.8 (1964). Print.

[10] Foelsche, U., M. Borsche, A. K. Steiner, A. Gobiet, B. Pirscher, G. Kirchengast, J. Wickert, and T. Schmidt. "Observing Upper Troposphere–Lower Stratosphere Climate with Radio Occultation Data from the CHAMP Satellite." *Climate Dynamics* 31.1 (2007): 49-65. Print.

[11] Garrison, J. L. "Re: How to Calculate Specular Points in STK." Message to Seebany Datta-Barua. 27 Sep. 2013. E-mail.

[12] Giancoli, D. C. "Light: Reflection and Refraction." *Physics for Scientists & Engineer*. Upper Saddle River, NJ: Pearson/Prentice Hall, 2008. Print.

[13] "Definition of a Yuma Almanac." *U.S. Coast Guard Navigation Center*. U.S. Department of Homeland Security, n.d. Web. 30 Nov. 2013. <http://www.navcen.uscg.gov/?pageName=gpsAlmanacs>.

[14] Guo, J., D. Yang, K. V. Ling, D. Shao, and Y. Zhang. "Geometry and Accuracy of Specular Points in GPS-Reflection Altimetry." *Chinese Journal of Electronics* 21.1 (2012): 91-96. Print.

[15] Hajj, G. A., and L. J. Romans. "Ionospheric Electron Density Profiles Obtained with the Global Positioning System: Results from the GPS/MET Experiment." *The Radio Science Bulletin* 33.1 (1998): 175-90. Web.

[16] Hofmann-Wellenhof, B., H. Lichtenegger, and E. Wasle. *GNSS--global Navigation Satellite Systems: GPS, GLONASS, Galileo, and More*. Wien: Springer, 2008. Print.

[17] Hoque, M. M., and N. Jakowski. "Ionospheric Propagation Effects on GNSS Signals and New Correction Approaches." *InTech*. (2012): 381-384. Print.

[18] "IS-GPS-200D." *U.S. Coast Guard Navigation Center*. Navstar GPS Space Segment/Navigation User Interfaces, 7 Dec. 2004. Web. 30 Nov. 2013. <http://www.navcen.uscg.gov/pdf/IS-GPS-200D.pdf>.

[19] Jakowski, N. "Radio Occultation Techniques for Probing the Ionosphere." *The Radio Science Bulletin* (2005): 4-15. Print.

[20] Katzberg, S. J., and J. L. Garrison. *Utilizing GPS to Determine Ionospheric Delay over the Ocean*. Hampton, VA: National Aeronautics and Space Administration, Langley Research Center, 1996. 1-12. Print.

[21] Komjathy, A., B. Wilson, X. Pi, V. Akopian, M. Dumett, B. Iijima, O. Verkhoglyadova, and A. J. Mannucci. "JPL/USC GAIM: On the Impact of Using COSMIC and Ground-based GPS Measurements to Estimate Ionospheric Parameters." *Journal of Geophysical Research* 115.A2 (2010). Print.

[22] Kostelecký, J., J. Klokočník, and C. A. Wagner. "Geometry and Accuracy of Reflecting Points in Bistatic Satellite Altimetry." *Journal of Geodesy* 79.8 (2005): 421-30. Print.

[23] Marchan-Hernandez, J. F., N. Rodriguez-Alvarez, A. Camps, X. Bosch-Lluis, I. Ramos-Perez, and E. Valencia. "Correction of the Sea State Impact in the L-Band Brightness Temperature by Means of Delay-Doppler Maps of Global Navigation Satellite Signals Reflected Over the Sea Surface." *IEEE Transactions on Geoscience and Remote Sensing* 46.10 (2008): 2914-923. Print.

[24] Misra, P., and P. Enge. *Global Positioning System: Signals, Measurements, and Performance*. Lincoln, MA: Ganga-Jamuna, 2012. Print.

[25] Nelder, J. A., and R. Mead. "A Simplex Method for Function Minimization." *The Computer Journal* 7.4 (1965): 308-13. Print.

[26] Pervan, B. “Introduction to Navigation Systems.” Illinois Institute of Technology. Engineering 1 Building, Chicago, IL. 15 Oct. 2012. Lecture.

[27] Platnick. S. "The Earth Observer." *National Aeronautics and Space Administration*25.3 (2013): 11-18. Web.

[28] Potula, B. S., Y. H. Chu, G. Uma, H. P. Hsia, and K. H. Wu. "A Global Comparative Study on the Ionospheric Measurements between COSMIC Radio Occultation Technique and IRI Model." *Journal of Geophysical Research* 116.A2 (2011): 1-24. Print.

[29] Ruf, C., S. Gleason, Z. Jelenak, S. Katzberg, A. Ridley, R. Rose, J. Scherrer, V. Zavorotny. "The NASA EV-2 Cyclone Global Navigation Satellite System (CYGNSS) Mission." *Aerospace Conference, 2013 IEEE* (2013): 1 7. *Google Scholar*. Web.

[30] Tascione, T. F. "Ionosphere." *Introduction to the Space Environment*. Malabar, FL: Krieger Pub., 1994. 65-74. Print.

[31] Wilson, B. D., A. J. Mannucci, D. N. Yuan, B. A. Iijima, X. Pi, C. M. Ho, and U. J. Lindqwister. "Monitoring the Ionosphere Using a Global GPS Network: Validation and Applications." *Jet Propulsion Laboratory* (1997): 1-9. Print.

[32] Wu, S. C., T. Meehan, and L. Young. "The Potential Use of GPS Signals as Ocean Altimetry Observables." *Proceedings of the National Technical Meeting-Institute of Navigation* (1997): 543-50. Print.